UNIVERSITÀ DEGLI STUDI DI MODENA E REGGIO EMILIA

Dipartimento di Scienze Fisiche, Informatiche e Matematiche

CORSO DI DOTTORATO DI RICERCA IN "PHYSICS AND NANOSCIENCES"

Tesi presentata per il conseguimento del titolo di Dottore di Ricerca in Fisica

---

Excitonic Insulator in Narrow-Gap Carbon Nanotubes

Candidato:
Giacomo SESTI

Relatori:
Prof. Elisa MOLINARI
Dr. Massimo RONTANI

Coordinatore della Scuola di Dottorato:
Prof. Stefano FRABBONI

XXXIV ciclo

Abstract

Single-wall carbon nanotubes, graphene sheets wrapped up on a cylindrical shape, have tightly bound excitons. This behaviour is a result of the weakly screened long wavelength potential binding electron and holes. If external interactions are minimized for example by suspending the tubes, narrow-gap carbon nanotubes become correlated insulators. The correlated phase so generated was proposed to have an excitonic origin. There are, however, other possible explanations such as a Peierls instability, a topological phase or a Mott Insulator.

Excitons are electron-hole couples bound by the Coulomb potential and behave at low temperatures as a weakly interacting bosonic gas. Above a critical density, excitons may condense but electron-hole recombination limits their lifetime, precluding an excitonic condensation in most materials in the absence of external stimuli. A spontaneous excitonic condensation requires excitons with a negative excitation energy and this exotic phase of matter is known as excitonic Insulator. The excitonic insulator is characterised by a reconstructed ground state composed by excitons resulting in the opening of a gap and breaking the symmetry of the underlying lattice.

In this work, I explore the idea of narrow gap carbon nanotubes as excitonic insulators. I compute in a quantitative manner the excitonic binding energies and the physical quantities associated to the excitonic insulator phase. Instrumental for determining the electron-hole binding energies is a careful evaluation of the screening properties of carbon nanotubes. I show that the standard effective-mass model systematically underestimates the interaction strength at long wavelength when compared with first principles calculations since it lacks a comprehensive description of the three-dimensional topology of the tube. I developed a new two-band model dielectric function exploiting a plane-wave expansion of Bloch states and the exact Coulomb cut-off technique. The electron-electron force computed with the new dielectric function compares quantum transport experiments and turns out to be super Coulombic at long-range.

Furthermore, I compute the phase diagram of the excitonic insulator ground state, as a function of tube chirality and radius. The self-consistent calculation shows that a large part of narrow-gap tubes are excitonic insulators at low temperature, the gap being weakly sensitive to the tube radius. Eventually, I find that the excitonic insulator phase of carbon nanotubes can be distinguished from the other many-body phases by looking at the dependence of the transport gap on the magnetic field. Specifically, I expect the transport gap in the excitonic phase to have a singular behaviour, with the appearance of a cusp at the Dirac field. I link

this unique behaviour of the excitonic phase to the strong sensibility to changes of screening induced by the magnetic field, not present in other correlated insulators.

Sommario

I nanotubi di carbonio a parete singola, strisce di grafene arrotolate in forma cilindrica, hanno stati eccitonici strettamente legati. Questo comportamento è il frutto di un potenziale a lungo-range debolmente schermato che lega elettroni e lacune. Se le interazioni esterne sono ridotte al minimo, per esempio sospendendo i tubi, i nanotubi di carbonio a piccolo gap diventano isolanti correlati. Si è proposto che la fase correlata così generata abbia un'origine eccitonica. Tuttavia, ci sono altre possibili spiegazioni come un'instabilità di Peierls, una fase topologica o un isolante di Mott.

Gli eccitoni sono coppie elettrone-lacuna legate dal potenziale di Coulomb e si comportano a basse temperature come un gas bosonico debolmente interagente. Sopra una densità critica, gli eccitoni possono condensare ma la ricombinazione elettrone-lacuna limita la loro vita media, impedendo una condensazione eccitonica nella maggior parte dei materiali in assenza di stimoli esterni. Una condensazione eccitonica spontanea richiede eccitoni aventi un'energia di eccitazione negativa e questa fase esotica della materia è nota come isolante eccitonico. L'isolante eccitonico è caratterizzato da uno stato fondamentale ricostruito composto da eccitoni che provoca l'apertura di un gap e la rottura della simmetria del reticolo sottostante.

In questo lavoro, esploro l'idea dei nanotubi di carbonio a piccolo gap come isolanti eccitonici. Calcolo in modo quantitativo le energie di legame eccitoniche e le quantità fisiche associate alla fase di isolante eccitonico. Di fondamentale importanza per determinare le energie di legame elettrone-lacuna è un'attenta valutazione delle proprietà di screening dei nanotubi di carbonio. Dimostro che il modello standard a massa efficace sottostima sistematicamente la forza di interazione a lungo-range rispetto ai calcoli a principio primo, poiché manca di una descrizione completa della topologia tridimensionale del tubo. Ho quindi sviluppato con un modello a due bande una nuova funzione dielettrica che sfrutta un'espansione a onde piane degli stati di Bloch e la tecnica esatta del troncamento del potenziale di Coulomb. La forza elettrone-elettrone calcolata con la nuova funzione dielettrica è confrontabile con esperimenti di trasporto quantistico e risulta essere super coulombiana a grandi distanze.

Inoltre, calcolo il diagramma di fase dello stato fondamentale dell'isolante eccitonico in funzione della chiralità del tubo e del raggio. Il calcolo autoconsistente mostra che gran parte dei tubi a piccolo gap sono isolanti eccitonici a bassa temperatura, con un gap che dipende poco dal raggio del tubo. Infine, trovo che la fase di isolante eccitonico dei nanotubi di carbonio può essere distinta dalle altre fasi correlate guardando la dipendenza del gap di trasporto dal campo mag-

netico. In particolare, mi aspetto che il gap di trasporto nella fase eccitonica abbia un comportamento singolare, con la comparsa di una cuspide al campo di Dirac. Collego questo comportamento unico della fase eccitonica alla forte sensibilità ai cambiamenti di screening indotti dal campo magnetico, non presenti in altre fasi correlate.

Contents

Chapter 1

Introduction

Carbon nanotubes (NTs), graphene strips rolled up to a cylindrical form, are ideal materials where to study strongly interacting electrons in one dimension [1, 2, 3, 4]. Due to the reduced dimensionality, Coulomb interaction remains unscreened at long wavelength whereas its strength reaches extreme values in suspended, undoped tubes, as the electric field lines spill over into the vacuum. Excitons, electron-hole pairs bound by Coulomb attraction, exhibit huge binding energies [5, 6, 7, 8, 9] that remain finite even in metallic NTs [10, 11]. Ultraclean, narrow-gap NTs may be charged in a controlled and reversible way by means of Coulomb blockade, hosting fascinating many-body states of matter. These include the Luttinger liquid [12, 13, 14, 15, 16, 17, 18, 19, 20], the Wigner crystal [21, 22, 20, 23, 24, 25, 26], and a correlated insulator understood as either a Mott [27] or an excitonic phase [28] (but Peierls insulators [29, 30, 31], topological phases [32], and hybrid scenarioes [33, 34, 35] were proposed as well).

Undoped NTs are always insulating [27, 20, 3, 4, 36, 37], including the armchair kind, which band theory predicts to be metallic and protected against gap-opening perturbations [2]. The contribution to the gap that is not accounted for by independent-electron models is thought to have a many-body origin, whose features critically depend on the range of electron-electron interaction. One possible, conventional scenario is the Mott insulator [27, 36], whose gap originates from the short-range part of Coulomb interaction. Its theory, a strong-coupling version of the Luttinger liquid, assumes the long-wavelength Coulomb force to be cutoff by nearby electrostatic gates in the experimental setup [12, 13, 14, 16, 17, 38]. A second possibility, recently proposed [28], is that the residual gap is due to the long-range part of Coulomb interaction, which binds electrons and holes into excitons.

Excitons, electrically neutral bosons, may condense at low temperatures if the their density overcomes a critical value [39, 40, 41, 42, 43, 44, 45]. This event is however very unlikely in most systems, as commonly, even at low temperatures,

excitons are short living excitations with a population well below the critical value. There have been various attempts to generate excitonic condensation through optical induction [46, 47, 48, 49, 50, 51, 52, 53, 54, 55, 56, 57]. In this case, excitonic condensation may appear only at quasi-equilibrium as stimulation by light is constantly required to maintain the excitonic population, which, otherwise, would be depleted by electron-hole recombination. The short lifetime of the optically generated excitons has however been a major limitation preventing for long time any observation of excitonic condensation [54, 58]. Nowadays, the excitonic lifetime can be hugely extended, typically up to some ns, working in optically induced semiconductors where electrons and holes are forcibly separated, either in real or reciprocal space. Systems of this kind are based for example on indirect gap semiconductors [59, 60], and bilayers [61, 62, 63, 64, 65, 66, 67, 68, 69]. In the last years, quasi-equilibrium condensations of excitons have finally been observed in double quantum well within a layered semiconductor structure [70, 71, 72, 73, 74].

Presence of external stimuli is however not a necessary requirement for excitonic condensation that is possible even at thermodynamic equilibrium [75, 76, 77, 78, 79]. In this latter case, the sea of spontaneously generated excitons gives rise to a new equilibrium phase known as excitonic insulator (EI). Necessary requirement for the EI is a strong long-range potential capable to overcome the energy cost of forming the electron-hole pairs. The EI is reminiscent of the superconductive state proposed by Bardeen, Cooper, and Schrieffer [80, 81]. There are indeed strong similarity between excitons and Cooper pairs starting from the fact that they are both two-bodies excitations: excitons are made up of an electron and a hole while Cooper pairs of two electrons. Both the excitations appear as fluctuations in the high-temperature phase and form only in the ordered, low-temperature phase; respectively the EI and the superconductor. However, as excitons are neutral excitations, the signature of the macroscopic order in a EI may be a charge density wave (CDW), a spin density density wave (SDW), or more generally a change of crystal symmetry that is spontaneously broken by the excitonic condensate, rather than a superconductive state.

The prototypical systems where the EI phase is thought possible are small gap semiconductors and semimetals [46, 49, 51, 82, 83, 84]. Certain physical factors favour the occurrence of an EI phase, such as the presence of an indirect gap, that reduces the dielectric screening, as well as the low-dimensionality which enhances the strength of the effective electron-hole attraction. In recent times, there has been a revival in the search of the EI thanks to several new candidate materials, among which chalcogenides with rare-earth [85, 86, 87] or with transition metals [88, 89, 90, 91, 92, 93, 94, 95, 96, 97, 98, 99, 100, 101, 102, 103, 104, 105, 106]. Many graphene based systems represent an intriguing possibility for the intense electronic interaction of such low dimensional systems coupled with small gaps

[107, 108, 109]. Signs of excitonic condensation have been observed for example in graphite [110, 111, 112] as the stacking of the graphene layers is suggested stabilising the EI phase [107]. Other very interesting graphene-based systems are naturally carbon nanotubes [28].

Instrumental for finding signs of an excitonic condensation in carbon nanotubes is a careful evaluation of their screening properties. Screening in nanotubes shows a complex behaviour due to its non local character, the interband electronic polarization being effective at intermediate ranges only [113]. As a result, in undoped nanotubes the electron-hole interaction, once projected onto the lowest conduction and highest valence band, is enhanced with respect to the bare force, for carrier separation larger than the NT radius [114]. Whereas the precise assessment of the dressed interaction requires the accurate calculation of the dielectric matrix, the computation from first principles is limited to nanotubes having a small unit cell, due to the heavy computational load. Therefore, a model dielectric function based on the effective-mass (EM) approximation is widely used, either in its original form by Ando [5] or in simpler versions [114, 115]. These models are able to reproduce the main non-local features of screening but rule out the excitonic instability [5]. Recent first-principle computations have however challenged the current EM models [28] as the ab-initio screened Coulomb interaction of armchair tubes exhibits at long-range a seemingly singular-like profile, in contrast to the Thomas-Fermi like behaviour of the EM models that predicts metals to have a heavilty screened short-range Coulomb interaction. This seeming singular profile turns out to cause an excitonic instability.

In view of the above results, it is first aim of my work to make a further quantitative assessment of the screened Coulomb interaction in narrow-gap NTs, starting from selected first-principle case studies to derive a model working for NTs of any size. Being the excitonic instability crucially linked to screening properties of NTs, my theis proceeds with a careful evaluation of excitonic instabilities in NTs. The work is organised as follows:

In chapter 2-3 I illustrate from a formal point the envelope function formalism for narrow-gap carbon nanotubes used during the work. The review follows the common approach used in literature [116, 2, 117]. This consists at first in calculating the tight-binding theory of graphene. I then specialise to the region of the Dirac cones, at the corners of the Brillouin zone, to introduce the envelope functions. The envelope functions of graphene are then extended to carbon nanotubes by treating nanotubes as folded graphene sheet. Finally, I discuss the main properties of carbon nanotubes according to established literature.

In chapter 4 I proceed to the study of screening properties of narrow-gap carbon nanotubes starting from selected first principles calculations. Crucially, I show that the EM model underestimates the strength of Coulomb interaction from first principles at long wavelength in both narrow- and zero-gap NTs, hence

missing the binding of low-energy excitons. The EM theory is shown to neglect the actual topology of the orbitals involved in the calculation of the polarization, as it takes Bloch states from graphene. To overcome this problem, I introduce a two-band, computationally cheap model of the polarization that copes with the tube-like topology of Bloch states by expanding them over a three-dimensional plane-wave basis set. Furthermore, I apply an exact cutoff technique to Coulomb potential [118], in order to avoid spurious interactions among replicas in supercell calculations. I eventually validate the model through comparison with first-principles results for zigzag and armchair NTs of different radii. As a generic outcome, I find that the effect of curvature on the overlap integrals between conduction and valence Bloch states leads to a significant enhancement of the dressed Coulomb interaction at long wavelength, $W(q \sim 0)$. My findings support the previous claim of excitonic instability [28] in armchair tubes, suggesting that the long-range part of Coulomb interaction rules many-body physics of NTs. As an application of the proposed model dielectric function, and motivated by a recent experiment by the Weizmann group [119], I compute the real-space effective Coulomb force between two electrons populating the lowest conduction band. This observable has been measured, for various electron-electron separations, in ultraclean suspended NTs in a non invasive manner [119].

In chapter 5 I evaluate the presence of excitonic instabilities in non-armchair narrow-gap carbon nanotubes as the armchair kind was already covered by [28]. To describe screening, I use the model developed in the previous chapter. As a two-bodies excitation, excitons energies are computed recurring to the Bethe-Salpeter equation. In case of excitonic instability, I describe formally the EI wavefunction analogously to Cooper instability of a superconducting state, with the excitons playing the role of the Cooper pairs. I then compute the new band gap of NTs in the EI phase. Eventually, I build up the phase diagram of the EI phase in absence of external stimuli for a wide range of NTs varying for radii and chiral angles.

The presence of excitonic instabilities in NTs, despite definitely proving that the EI phase can cause the semiconducting behaviour of NTs, do not suffice to rule out the alternative proposed explanations for the semiconducting behaviour of NTs, such as a Mott-Hubbard transition [13, 27]. Indeed, even other many-body mechanisms could trigger an instability in NTs. When multiple many-body instabilities can occur at the same time, the identification of the correct many-body mechanism typically relies on studying the characteristic physical quantities associated to the many-body mechanism. For the EI phase, this would be the presence of a SDW or the breaking of the sublattice symmetry. Unfortunately, the low dimensionality of carbon nanotubes and the strong susceptibility to external stimuli make challenging to detect the broken symmetry of the NTs, preventing to easily assess the nature of the many-body mechanism. In chapter 6, I argue that a

possible solution to the current uncertainty on the origin of NTs many-body gap may come from the studies of the NTs transport gap with respect to varying axial magnetic fields. Not fully disclosed in previous works, the sharp dependence of the EI phase on screening creates a peculiar tunability of the EI many-body gap on the magnetic field. I show that the NTs transport gap dispersion with respect to the field in the EI phase exhibits the appearance of a cusp at the Dirac field. On the contrary, in the conventional Mott insulator proposal, the NTs transport gap does not show any peculiar tunability with the field, due to the short-range electron-electron interaction being weakly sensible to the system screening. I then show for nanotubes of fixed radii the map plot of the EI phase at the changing of the magnetic field.

As final remark, I would like to point out that the first principle computations shown in chapter 4 have been performed by Daniele Varsano, while all the other results presented during chapters 4, 5 and 6 come from my work.

List of Publications

- Anomalous screening in narrow-gap carbon nanotubes submitted to PRB, available on arXiv at https://arxiv.org/abs/2201.10199
- Phase diagram of the Excitonic Insulator in narrow-gap CNT in preparation to be submitted to PRB. Chapter 5 of my thesis work
- Excitonic vs Mott Insulator in carbon nanotubes: a proposed experimental test in preparation to be submitted to PRL. Chapter 6 of my thesis work

Chapter 2

The tight-band theory of graphene

Graphene has maybe been the most prominent material in condensed matter physics in the last decades, inspiring the present-day research of exotic materials capable to host peculiar states of matter. In spite of its recent success, graphene cannot be fully classified as a novel material since graphene is a single layer of graphite. Graphite has been known and studied for a long time in solid state physics. Nevertheless, the experimental isolation of graphene turned out to be a major challenge for various years and it was finally achieved in 2004 by Novoselov et al [120]. Since then, graphene has been a mainstream topic in condensed matter physics, with a whole section of literature focused in discussing methods of exploitation and manipulation. The great appeal of graphene is surely due to its remarkable conducting properties that are reminiscent of the behaviour of massless relativistic particles. In order to understand how this occurs, it is necessary to study its electronic structure.

2.1 The crystal structure of graphene

In a graphene layer, the carbon atoms arrange on a plane (Fig. 2.1) forming a honeycomb lattice with interatomic distance $a_{cc} = 1.42$ Å [1, 121]. The carbon atoms are bounded to their three nearest neighbours by means of covalent σ bonds spread on the plane. The p_z orbitals of the carbon atoms, perpendicular to the plane, develop π bonds. To describe the graphene layer, the simplest choice could seem using as unit cells the hexagons that make up the honeycomb lattice. However, the hexagonal cells are not unit cell as the carbon atoms are located at the hexagonal cells corners and hence shared with the neighbouring cells. A different choice for the unit cell has to be made that ensures that each carbon atom belongs to a unique cell. The solution is adopting as unit cell of the direct lattice a

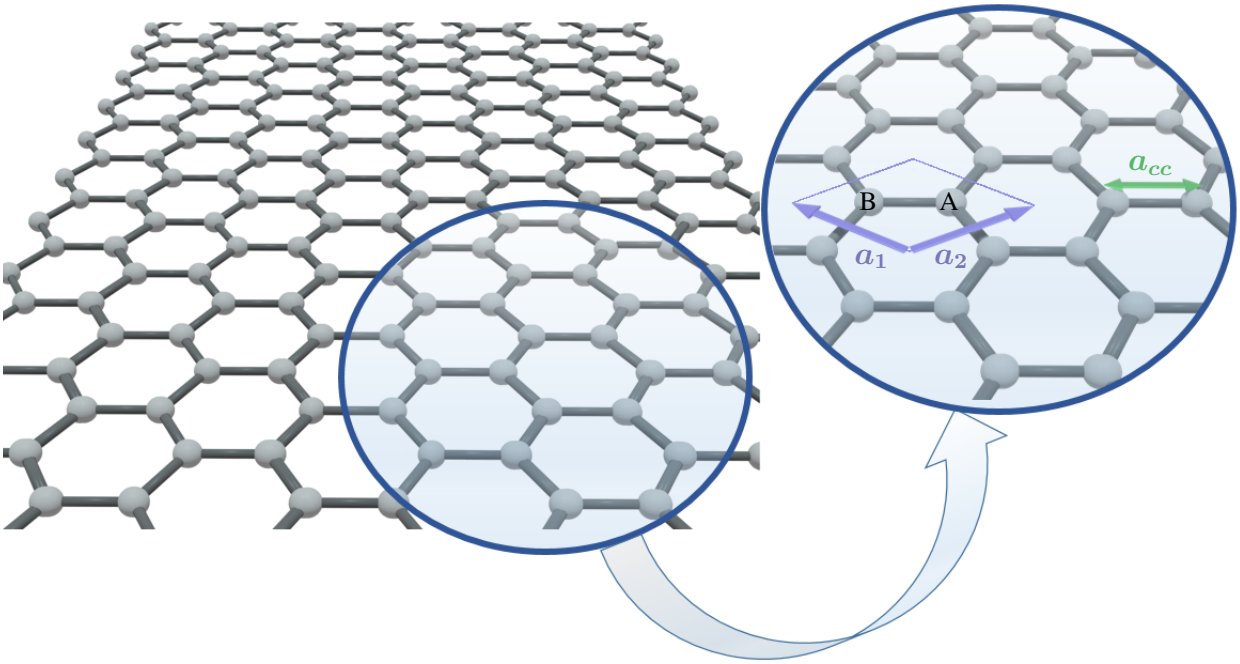

Figure 2.1: Illustration of the graphene lattice and of its lattice vectors. The rhomboidal unit cell contains the two inequivalent A and B atoms.

rhomboidal unit cell enclosing two carbon atoms [122]. The rhomboidal unit cell is built by connecting the centers of neighbouring hexagonal cells as illustrated in Fig. 2.1. The two vectors $\mathbf{a_1}$ and $\mathbf{a_2}$ are the basis of the direct lattice:

$$\begin{aligned} \mathbf{a_1} &= \frac{a}{2}\begin{pmatrix} \sqrt{3} \\ 1 \end{pmatrix}, \\ \mathbf{a_2} &= \frac{a}{2}\begin{pmatrix} -\sqrt{3} \\ 1 \end{pmatrix}, \end{aligned} \tag{2.1}$$

where $a = \sqrt{3}a_{cc} = 2.46$ Å is the graphene lattice constant.

The two atoms belonging to the unit cell, from now on dubbed A atom and B atom, are separated by the interatomic distance a_{cc}. By addition of direct lattice vectors to the positions of any couple of A and B atoms, it is possible to find the positions of all the carbon atoms in the honeycomb lattice. However, starting from an A or a B atom, the addition of direct lattice vectors allows to reach only atoms that occupy the same position in the unit cell. That is to say, it is not possible to reach any B atom starting from an A atom by means of combinations of direct lattice vectors and viceversa. Therefore, the graphene honeycomb lattice can be conceived as the superposition of two sublattices A and B, both exclusively made

up of A or B atoms respectively. The two sublattices are shifted with respect to each other by the interatomic distance a_{cc}. The lattice points of the two sublattices are:

$$\begin{aligned} \mathbf{R_A} &= \mathbf{R_{0A}} + n_1\mathbf{a_1} + n_2\mathbf{a_1}, \\ \mathbf{R_B} &= \mathbf{R_{0B}} + n_1\mathbf{a_1} + n_2\mathbf{a_2}, \end{aligned} \tag{2.2}$$

for any $n_1, n_2 \in \mathbb{Z}$. We choose the origin such that:

$$\begin{aligned} \mathbf{R_{0A}} &= a \begin{pmatrix} \frac{1}{2\sqrt{3}} \\ 0 \end{pmatrix}, \\ \mathbf{R_{0B}} &= a \begin{pmatrix} -\frac{1}{2\sqrt{3}} \\ 0 \end{pmatrix} = -\mathbf{R_{0A}}. \end{aligned} \tag{2.3}$$

We can now consider the reciprocal lattice of graphene. The reciprocal lattice vectors follow the relation $\mathbf{a_i} \cdot \mathbf{b_j} = 2\pi\delta_{ij}$. In the case of the rhomboidal unit cell, the reciprocal lattice vectors are:

$$\begin{aligned} \mathbf{b_1} &= \frac{2\pi}{a} \begin{pmatrix} \frac{1}{\sqrt{3}} \\ 1 \end{pmatrix}, \\ \mathbf{b_2} &= \frac{2\pi}{a} \begin{pmatrix} -\frac{1}{\sqrt{3}} \\ 1 \end{pmatrix}, \end{aligned} \tag{2.4}$$

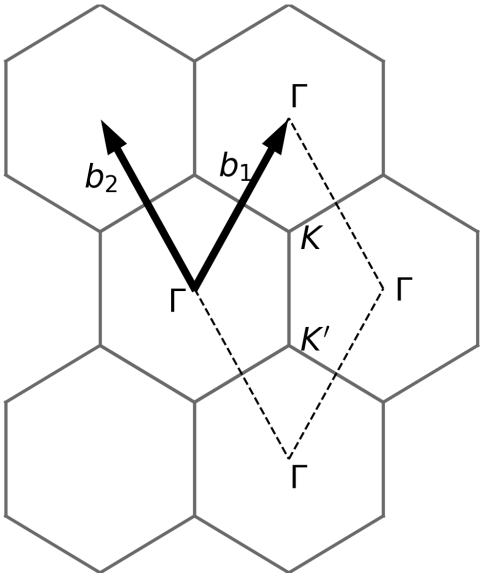

Figure 2.2: Illustration of the reciprocal lattice of graphene where we have indicated the high symmetry points $\mathbf{\Gamma}$ and $\mathbf{K}$. The rhomboidal first Brillouin zone contains a $\mathbf{K}$ and a $\mathbf{K'}$ corner.

The first Brillouin zone (1BZ) of graphene has an hexagonal shape. In the same spirit of what done for the unit cell in real space, it is possible to choose a rhomboidal first Brillouin zone as alternative to the hexagonal Brillouin zone. The rhomboidal Brillouin zone is built connecting the centers of neighbouring hexagonal zones; the procedure is illustrated in Fig 2.2. The centers of the hexagonal Brillouin zone are also known as Γ points. The rhomboidal Brillouin zone contains only two of the hexagon corners. We will call the two corners $\mathbf{K}$ and $\mathbf{K}'$ points:

$$\begin{aligned} \mathbf{K} &= \frac{2\pi}{a}\begin{pmatrix} \frac{1}{\sqrt{3}} \\ \frac{1}{3} \end{pmatrix}, \\ \mathbf{K}' &= \frac{2\pi}{a}\begin{pmatrix} \frac{1}{\sqrt{3}} \\ -\frac{1}{3} \end{pmatrix}. \end{aligned} \tag{2.5}$$

Similarly to the positions of A and B atoms in real space, it is not possible to move from the $\mathbf{K}$ point to the $\mathbf{K}'$ point by combination of reciprocal lattice vectors. The two points $\mathbf{K}$ and $\mathbf{K}'$ are defined inequivalent and form two separate sublattices in reciprocal space. At the vertices of the hexagonal Brillouin zone, there are three $\mathbf{K}$ points and three $\mathbf{K}'$ points. The whole system is symmetric under rotations of $\frac{2\pi}{3}$.

2.2 The tight-binding model

The carbon atoms have in total four valence electrons. Three of these electrons hybridise into sp^2 orbital while the remaining one occupies the p_z orbital. As previously said, the sp^2 are involved in planar σ bonding while the p_z electrons in π bondings. The two type of bondings turn out to cover different energy range. We plot in Fig. (2.3) the electronic bands of graphene along the high-symmetry M-Γ-K directions. The σ bands are very distant from the Fermi energy and are well separated in energy by about 10 eV [1, 121, 123]. Thus, the σ bands are little involved for what concerns the electronic properties of graphene. On the contrary, the π and π^* bands cross the Fermi level in correspondence of the Brillouin zone corners $\mathbf{K}$ and $\mathbf{K}'$ [124]. This determines a semi-metallic behaviour. The electronic dispersion of the two π bands can be depicted through a tight-binding Hamiltonian [1, 125]. As the overlap between the p_z orbitals and the planar sp^2 is strictly zero by symmetry, the π electrons are treated independently of the other valence electrons. Thus, in order to describe the generic eigenfunction of the graphene state, it is sufficient to consider a linear combinations of two π orbitals; each one centred on a different atomic site:

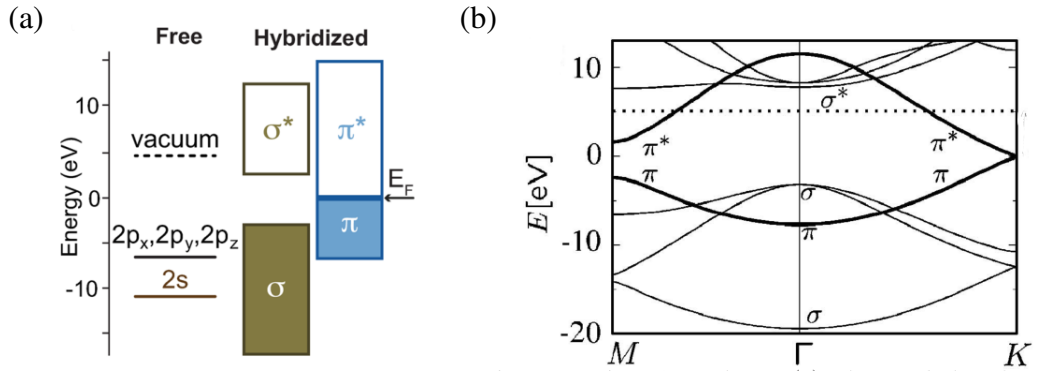

Figure 2.3: (a) Schematic energy range of the atomic and hybridized orbitals of the carbon atoms. (b) Electronic band structure of graphene along the high-symmetry M-Γ-K direction. The bonding π and antibonding π^* are respectively the last valence band and the first conduction band and cross at the K points of the Brillouin zone. The bonding σ and antibonding σ^* bands are well separated in energy. Above the vacuum level, marked with a dashed line, the states of the continuum are difficult to describe and merge with the σ^* bands. (figure (a) is taken from [4] and figure (b) from [2])

$$\Psi(\mathbf{k},\mathbf{r}) = C_A(\mathbf{k})\Phi_A(\mathbf{k},\mathbf{r}) + C_B(\mathbf{k})\Phi_B(\mathbf{k},\mathbf{r}) \tag{2.6}$$

with

$$\begin{aligned}\Phi_A(\mathbf{k},\mathbf{r}) &= \frac{1}{\sqrt{N}} e^{i\theta_A} \sum_{\{\mathbf{R_A}\}} e^{i\boldsymbol{k}\cdot\mathbf{R_A}} \phi_\pi(\mathbf{r}-\mathbf{R_A}),\\ \Phi_B(\mathbf{k},\mathbf{r}) &= \frac{1}{\sqrt{N}} e^{i\theta_B} \sum_{\{\mathbf{R_B}\}} e^{i\boldsymbol{k}\cdot\mathbf{R_B}} \phi_\pi(\mathbf{r}-\mathbf{R_B}).\end{aligned} \tag{2.7}$$

The wavefunction ϕ_π indicates the p_z atomic orbitals and we allow for different phase factors in front of the two Bloch functions $\Phi_\alpha(\mathbf{k},\mathbf{r})$. The $\Phi_\alpha(\mathbf{k},\mathbf{r})$ functions are normalized to N that is the number of atoms in each sublattice, or alternatively the number of unit cells.

Within the tight binding approximation, we describe the electrons with a single-body Hamiltonian consisting of the kinetic term and the crystal field. The crystal field is the periodic potential created by the other charges of the system. The electron-electron interaction is as usual omitted at this level:

$$\mathcal{H} = -\frac{\hbar^2}{2m}\nabla^2 + \sum_{\alpha=A,B}\sum_{\{\mathbf{R}_\alpha\}} V(\mathbf{r}-\mathbf{R}_\alpha). \tag{2.8}$$

The energies of the graphene states are:

$$E(\mathbf{k}) = \frac{\langle \Psi(\mathbf{k},\mathbf{r})|\mathcal{H}|\Psi(\mathbf{k},\mathbf{r})\rangle}{\langle \Psi(\mathbf{k},\mathbf{r})|\Psi(\mathbf{k},\mathbf{r})\rangle}, \tag{2.9}$$

Introducing the expression of the tight-binding wavefunction $\Psi(\mathbf{k},\mathbf{r})$ from Eq.(2.6), we have:

$$E(\mathbf{k}) = \frac{\sum_{\alpha=A}^{B}\sum_{\beta=A}^{B} C_\alpha^*(\mathbf{k})C_\beta(\mathbf{k})\langle \Phi_\alpha(\mathbf{k},\mathbf{r})|\mathcal{H}|\Phi_\beta(\mathbf{k},\mathbf{r})\rangle}{\sum_{\alpha=A}^{B}\sum_{\beta=A}^{B} C_\alpha^*(\mathbf{k})C_\beta(\mathbf{k})\langle \Phi_\alpha(\mathbf{k},\mathbf{r})|\Phi_\beta(\mathbf{k},\mathbf{r})\rangle}. \tag{2.10}$$

The evaluation integral at the numerator is known as the transfer integral $H_{\alpha\beta}$, at the denominator instead appears the overlap integral $S_{\alpha\beta}$:

$$E(\mathbf{k}) = \frac{\sum_{\alpha=A}^{B}\sum_{\beta=A}^{B} C_\alpha^*(\mathbf{k})C_\beta(\mathbf{k})H_{\alpha\beta}}{\sum_{\alpha=A}^{B}\sum_{\beta=A}^{B} C_\alpha^*(\mathbf{k})C_\beta(\mathbf{k})S_{\alpha\beta}}. \tag{2.11}$$

The multiplicative coefficients $C_\alpha(\mathbf{k})$ are chosen in order to minimize the energy $E(\mathbf{k})$:

$$\frac{\partial E(\mathbf{k})}{\partial C_\alpha^*} = 0, \tag{2.12}$$

$$\frac{\sum_{\beta=A}^{B} C_\beta(\mathbf{k})H_{\alpha\beta}}{\sum_{\alpha=A}^{B}\sum_{\beta=A}^{B} C_\alpha^*(\mathbf{k})C_\beta(\mathbf{k})S_{\alpha\beta}} - \frac{\sum_{\alpha=A}^{B}\sum_{\beta=A}^{B} C_\alpha^*(\mathbf{k})C_\beta(\mathbf{k})H_{\alpha\beta}}{\left(\sum_{\alpha=A}^{B}\sum_{\beta=A}^{B} C_\alpha^*(\mathbf{k})C_\beta(\mathbf{k})S_{\alpha\beta}\right)^2}\sum_{\beta=A}^{B} C_\beta(\mathbf{k})S_{\alpha\beta} = 0. \tag{2.13}$$

In the right term of the previous equation, we can introduce the energy as from Eq.(2.11):

$$\frac{\sum_{\beta=A}^{B} C_\beta(\mathbf{k})H_{\alpha\beta}}{\sum_{\alpha=A}^{B}\sum_{\beta=A}^{B} C_\alpha^*(\mathbf{k})C_\beta(\mathbf{k})S_{\alpha\beta}} - \frac{E(k)\sum_{\beta=A}^{B} C_\beta(\mathbf{k})S_{\alpha\beta}}{\left(\sum_{\alpha=A}^{B}\sum_{\beta=A}^{B} C_\alpha^*(\mathbf{k})C_\beta(\mathbf{k})S_{\alpha\beta}\right)} = 0, \tag{2.14}$$

leading to:

$$\sum_{\beta=A}^{B} \left[H_{\alpha\beta} - E(\mathbf{k}) S_{\alpha\beta}\right] C_{\beta}(\mathbf{k}) = 0. \tag{2.15}$$

This equation has to hold for all values of α. We can reformulate the equation from a matrix point of view, introducing a coefficient vector C:

$$\left[H - E(\mathbf{k}) S\right] C = 0. \tag{2.16}$$

This equation has non-trivial solutions only if

$$\det\left[H - E(\mathbf{k}) S\right] = 0. \tag{2.17}$$

Hence, we have to solve the secular equation. For each k there are two solutions, representing the bonding and anti-bonding π bands. In order to solve the equation, we now find the elements of the transfer matrix H and of the overlap matrix S.

2.2.1 The transfer matrix

We evaluate the transfer matrix H on the basis of the atomic sublattice. Thus, we compute all the elements of the kind $H_{\alpha\beta}$. The atomic orbitals of the π electrons are strongly localized around the atomic sites, so in the derivation we will adopt the nearest neighbour approximation. This approximation consists in assuming that the only non-vashining integrals are those obtained combining atomic orbitals of atoms on the same site or that are nearest neighbours. We start by computing the diagonal elements:

$$\begin{aligned} H_{\alpha\alpha}(\mathbf{k}) &= \frac{1}{V} \int d^3\mathbf{r}\ \Phi^*_{\alpha}(\mathbf{k}, \mathbf{r}) \mathcal{H} \Phi_{\alpha}(\mathbf{k}, \mathbf{r}), \\ &= \frac{1}{VN} \sum_{\{\mathbf{R}_\alpha\}} \sum_{\{\mathbf{R}'_\alpha\}} e^{i\mathbf{k}\cdot(\mathbf{R}'_\alpha - \mathbf{R}_\alpha)} \int d^3\mathbf{r}\ \phi^*_{\pi}(\mathbf{r} - \mathbf{R}_\alpha)\ \mathcal{H}\ \phi_{\pi}(\mathbf{r} - \mathbf{R}'_\alpha). \end{aligned} \tag{2.18}$$

At this point, we apply the nearest neighbour approximation. As two atoms of the same type are never nearest neighbour, only the case $\mathbf{R}'_\alpha = \mathbf{R}_\alpha$ has to be considered.

$$H_{\alpha\alpha}(\mathbf{k}) = \frac{1}{VN} \sum_{\{\mathbf{R}_\alpha\}} \int d^3\mathbf{r}\ \phi^*_{\pi}(\mathbf{r} - \mathbf{R}_\alpha)\ \mathcal{H}\ \phi_{\pi}(\mathbf{r} - \mathbf{R}_\alpha). \tag{2.19}$$

Here, we are averaging $\mathcal{H}$ with respect to the $\phi_\pi(\mathbf{r} - \mathbf{R}_\alpha)$ orbitals, that are eigenfunctions of the atomic Hamiltonian at the sites $\mathbf{R}_\alpha$ with eigenvalue the energy of

the $2p$ band. The atomic Hamiltonian at the sites $\mathbf{R}_\alpha$ is however contained within $\mathcal{H}$. When averaging, we can imagine that the atomic Hamiltonian is the leading term inside $\mathcal{H}$ while the contribution of the others charges approximately cancels out by symmetry. Thus:

$$\mathcal{H}\ \phi_\pi(\mathbf{r}-\mathbf{R}_\alpha) \simeq \epsilon_{2p}\phi_\pi(\mathbf{r}-\mathbf{R}_\alpha), \tag{2.20}$$

$$H_{\alpha\alpha}(\mathbf{k}) \simeq \frac{1}{N}\sum_{\{\mathbf{R}_\alpha\}} \epsilon_{2p} = \epsilon_{2p}. \tag{2.21}$$

The result is independent on the sublattice index and then it is the same for A and B sites.

We now consider the out of diagonal elements:

$$H_{\alpha\beta}(\mathbf{k}) = \frac{1}{V}\int d^3\mathbf{r}\ \Phi^*_\alpha(\mathbf{k},\mathbf{r})\mathcal{H}\Phi_\beta(\mathbf{k},\mathbf{r}) \quad \text{with} \quad \alpha \neq \beta. \tag{2.22}$$

The two terms of this kind $H_{AB}(\mathbf{k})$ and $H_{BA}(\mathbf{k})$ are related to each other since $H_{AB}(\mathbf{k})$= $H^*_{BA}(\mathbf{k})$. We make the computation only for $H_{AB}(\mathbf{k})$.

$$H_{AB}(\mathbf{k}) = \frac{e^{i(\theta_B-\theta_A)}}{VN}\sum_{\{\mathbf{R_A}\}}\sum_{\{\mathbf{R'_B}\}} e^{i\mathbf{k}\cdot(\mathbf{R'_A}-\mathbf{R_B})}\int d^3\mathbf{r}\ \phi^*_\pi(\mathbf{r}-\mathbf{R_A})\ \mathcal{H}\ \phi_\pi(\mathbf{r}-\mathbf{R'_B}). \tag{2.23}$$

Thanks to the nearest neighbour approximation, for each site of the A sublattice we keep only the contributions of the three nearest neighbouring B sites. The three nearest neighbours with respect to any A atom are at a distance $\frac{a}{\sqrt{3}}$ and they are equispaced by angles $\frac{2\pi}{3}$ on the plane.

$$\mathbf{R_j} = \mathbf{R_A} + \frac{a}{\sqrt{3}}\left(\cos\left(\frac{2\pi(j-1)}{3}\right), \sin\left(\frac{2\pi(j-1)}{3}\right)\right), \quad \text{with}\ \ j=1,2,3. \tag{2.24}$$

$$\begin{aligned}
\mathbf{R_1} =& a\left(\frac{1}{\sqrt{3}}, 0\right),\\
\mathbf{R_2} =& a\left(-\frac{1}{2\sqrt{3}}, \frac{1}{2}\right),\\
\mathbf{R_3} =& a\left(-\frac{1}{2\sqrt{3}}, -\frac{1}{2}\right).
\end{aligned} \tag{2.25}$$

The transfer integral $H_{AB}(\mathbf{k})$ becomes:

$$H_{AB}(\mathbf{k}) = \frac{e^{i(\theta_B-\theta_A)}}{VN}\sum_{j=1}^{3} e^{i\mathbf{k}\cdot\mathbf{R_j}} \sum_{\{\mathbf{R_A}\}} \int d^3\mathbf{r}\ \phi_\pi^*(\mathbf{r}-\mathbf{R_A})\ \mathcal{H}\ \phi_\pi(\mathbf{r}-\mathbf{R_A}-\mathbf{R_j}). \quad (2.26)$$

We define t_j as:

$$t_j = \frac{1}{VN}\sum_{\{\mathbf{R_A}\}} \int d^3\mathbf{r}\ \phi_\pi^*(\mathbf{r}-\mathbf{R_A})\ \mathcal{H}\ \phi_\pi(\mathbf{r}-\mathbf{R_A}-\mathbf{R_j}). \quad (2.27)$$

$$H_{AB}(\mathbf{k}) = e^{i(\theta_B-\theta_A)}\sum_{j=1}^{3} t_j e^{i\mathbf{k}\cdot\mathbf{R_j}}. \quad (2.28)$$

The quantity t_j, that in principle may depend on the index j, is actually the same for all values of the index j. We prove this by applying to t_j a rotation $\hat{\mathcal{R}}$ of the plane amounting to $\pm\frac{2\pi}{3}$.

$$\hat{\mathcal{R}}(t_j) = \frac{1}{VN}\sum_{\{\mathbf{R_A}\}} \int d^3\mathbf{r}\ \hat{\mathcal{R}}(\phi_\pi^*(\hat{\mathcal{R}}\mathbf{r}-\hat{\mathcal{R}}\mathbf{R_A}))\ \mathcal{H}\ \hat{\mathcal{R}}(\phi_\pi(\hat{\mathcal{R}}\mathbf{r}-\hat{\mathcal{R}}\mathbf{R_A}-\hat{\mathcal{R}}\mathbf{R_j})). \quad (2.29)$$

First of all, we need to remember that the π orbitals are invariant under rotations on the xy plane, so only the arguments of the functions are affected by the rotation. In addiction, t_j being a scalar remains the same.

$$t_j = \frac{1}{VN}\sum_{\{\mathbf{R_A}\}} \int d^3\mathbf{r}\ \phi_\pi^*(\hat{\mathcal{R}}\mathbf{r}-\hat{\mathcal{R}}\mathbf{R_A})\ \mathcal{H}\ \phi_\pi(\hat{\mathcal{R}}\mathbf{r}-\hat{\mathcal{R}}\mathbf{R_A}-\hat{\mathcal{R}}\mathbf{R_j}). \quad (2.30)$$

The $\mathbf{r}$ is invariant since we are integrating over this variable, the set of $\{\mathbf{R_A}\}$ is unaffected too because the whole graphene plane is symmetric under rotations of $\pm\frac{2\pi}{3}$. It reduces to:

$$t_j = \frac{1}{VN}\sum_{\{\mathbf{R_A}\}} \int d^3\mathbf{r}\ \phi_\pi^*(\mathbf{r}-\mathbf{R_A})\ \mathcal{H}\ \phi_\pi(\mathbf{r}-\mathbf{R_A}-\hat{\mathcal{R}}\mathbf{R_j}). \quad (2.31)$$

So, the only effect of the rotation $\hat{\mathcal{R}}(t_j)$ is to rotate the $\mathbf{R_j}$. However, the $\mathbf{R_j}$ are equispaced by angles of $\frac{2\pi}{3}$ as one can check looking at Eq.(2.25). Thus, the rotation basically changes the value of the index j in $\mathbf{R_j}$ to its other possible values. This sets an equivalence between all the t_j and we can drop the index dependence $\forall\ t_j = t$. The transfer integral t is real and has to be negative, since

the π orbitals are approximate bound states of the Hamiltonian $\mathcal{H}$. At this stage, we can go back to Eq.(2.28):

$$H_{AB}(\mathbf{k}) = t\, e^{i(\theta_B - \theta_A)} \sum_{j=1}^{3} e^{i\mathbf{k}\cdot\mathbf{R_j}} = t\, e^{i(\theta_B - \theta_A)} \alpha(\mathbf{k}), \tag{2.32}$$

with

$$\alpha(\mathbf{k}) = \sum_{j=1}^{3} e^{i\mathbf{k}\cdot\mathbf{R_j}} = e^{\frac{ik_x a}{\sqrt{3}}} + 2e^{-\frac{ik_x a}{2\sqrt{3}}} \cos\left(\frac{k_y a}{2}\right). \tag{2.33}$$

2.2.2 The overlap matrix

We now consider the matrix of the overlap integrals S and we expand S on the basis of the sublattices A and B. Under this choice, the diagonal elements are straightforward:

$$S_{\alpha\alpha}(\mathbf{k}) = \frac{1}{V} \int d^3\mathbf{r}\; \Phi^*_\alpha(\mathbf{k},\mathbf{r}) \Phi_\alpha(\mathbf{k},\mathbf{r}) = 1, \tag{2.34}$$

due to normalization requirements.

The two out of diagonal elements of the overlap matrix S are one the complex conjugated of the other: $S_{AB}(\mathbf{k}) = S^*_{BA}(\mathbf{k})$. As in the previous section, we compute the term $S_{AB}(\mathbf{k})$:

$$\begin{aligned} S_{AB}(\mathbf{k}) &= \frac{1}{V} \int d^3\mathbf{r}\; \Phi^*_A(\mathbf{k},\mathbf{r}) \Phi_B(\mathbf{k},\mathbf{r}), \\ &= \frac{1}{VN} \sum_{\{\mathbf{R_A}\}} \sum_{\{\mathbf{R'_B}\}} e^{i\mathbf{k}\cdot(\mathbf{R'_A} - \mathbf{R_B})} \int d^3\mathbf{r}\; \phi^*_\pi(\mathbf{r} - \mathbf{R_A}) \phi_\pi(\mathbf{r} - \mathbf{R'_B}). \end{aligned} \tag{2.35}$$

Operating within the nearest neighbour approximation, it reduces to:

$$\begin{aligned} S_{AB}(\mathbf{k}) &= \frac{1}{V} \int d^3\mathbf{r}\; \Phi^*_A(\mathbf{k},\mathbf{r}) \Phi_B(\mathbf{k},\mathbf{r}), \\ &= \frac{1}{VN} e^{i(\theta_B - \theta_A)} \sum_{j=1}^{3} e^{i\mathbf{k}\cdot\mathbf{R_j}} \int d^3\mathbf{r}\; \phi^*_\pi(\mathbf{r} - \mathbf{R_A}) \phi_\pi(\mathbf{r} - \mathbf{R_A} - \mathbf{R_j}). \end{aligned} \tag{2.36}$$

The common practice here is to adopt the so called orthogonal tight-binding, that consists in neglecting overlaps of π orbitals on different sites not mediated by the Hamiltonian. As a consequence, we set $S_{AB}(\mathbf{k}) = 0$.

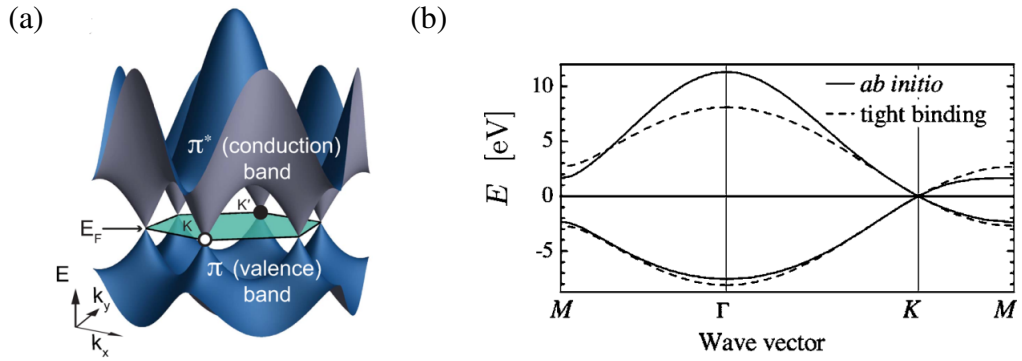

Figure 2.4: (a) Tight-binding π bands on the 2D Brillouin zone of graphene (b) Comparison of the ab-initio π bands in solid lines with the tight-binding results (figure (a) is taken from [4], figure (b) adapted from [126])

2.2.3 The band structure of the π states

Once determined the matrix elements of H and S, we retrieve the dispersion of the π states solving the secular equation Eq.(2.17) in the basis of the sublattices:

$$\begin{aligned} &\det\left[H - E(\mathbf{k})S\right] = 0, \\ &\det\begin{bmatrix} \epsilon_{2p} - E & te^{i(\theta_B-\theta_A)}\alpha(\mathbf{k}) \\ te^{-i(\theta_B-\theta_A)}\alpha^*(\mathbf{k}) & \epsilon_{2p} - E \end{bmatrix} = 0, \\ &(\epsilon_{2p} - E)^2 - t^2|\alpha(\mathbf{k})|^2 = 0, \\ &E - \epsilon_{2p} = \mp t|\alpha(\mathbf{k})|. \end{aligned} \tag{2.37}$$

It is clear that ϵ_{2p}, the energy of the $2p$ band, plays the role of the energy reference of the system. For sake of clarity, we shift this energy reference to 0, so as $E' = E - \epsilon_{2p}$. Hence, dropping the primed index, the energy dispersion becomes:

$$\begin{aligned} &E = \mp\, t|\alpha(\mathbf{k})|, \\ &E = \pm\, |t|\sqrt{1 + 4\cos\left(\frac{\sqrt{3}k_x a}{2}\right)\cos\left(\frac{k_y a}{2}\right) + 4\cos^2\left(\frac{k_y a}{2}\right)}, \end{aligned} \tag{2.38}$$

where the $\pm$ symbols refer respectively to the conduction band and the valence band.

We plot in Fig.(2.4-a) the two energy dispersions of the π bands from tight-binding. The two bands touch when the function $|\alpha(\mathbf{k})| = 0$. This condition is met at the **K** points, determining the semi-metallic behaviour. Thus, graphene is a special semimetal whose Fermi surface is reduced to the six **K** points of the hexagonal Brillouin zone. The dispersion of the π bands computed with nearest-neighbour orthogonal tight-binding agrees particularly well with first principle

computations, especially in the regions close to the Fermi energy (Fig.(2.4-b)). The agreement between tight-binding and first principle can become even better if relaxing the hypothesis of orthogonality between π orbitals and including next-nearest neighbour [127]. In this latter case, tight-binding displays the breaking of the particle-hole symmetry also appearing in ab-initio.

We can deepen the analysis of the electronic behaviour in the region in the neighbourhood of the $\mathbf{K}$ points through an expansion of Eq.(2.38).

$$E_{\pm}(\mathbf{K}+\delta\mathbf{k}) = \pm\hbar v_F|\delta k|. \tag{2.39}$$

The conduction and valence bands show a nearly linear dispersion with a Fermi velocity $v_F = |t|\frac{\sqrt{3}a}{2\hbar}$. This type of energy dispersion is very peculiar because it is characteristic of massless relativistic fermions while in semiconductors electrons typically follow a quadratic energy-momentum relation. The regions in which it is observed the nearly linear dispersion of the energy are called Dirac cones. In order to characterise the electronic properties of graphene and derived materials, it is often sufficient to consider only the region of the Brillouin zone with the Dirac cones because the electronic processes are mainly limited to this area of the reciprocal space.

2.3 Envelope functions of graphene

At the beginning of section 2.2, we have defined the general wavefunction of graphene as:

$$\Psi(\mathbf{k},\mathbf{r}) = C_A(\mathbf{k})\Phi_A(\mathbf{k},\mathbf{r}) + C_B(\mathbf{k})\Phi_B(\mathbf{k},\mathbf{r}), \tag{2.40}$$

where the $\Phi_\alpha(\mathbf{k},\mathbf{r})$ are the Bloch functions and the multiplicative coefficients $C_A(\mathbf{k})$ and $C_B(\mathbf{k})$ have turned out to be the eigenfunctions of the secular equation Eq.(2.15). Based on the band structure, we have seen that to characterise graphene is sufficient to limit to the region where appear the Dirac cones. In this region, we can manipulate the tight-binding wavefunction and write it in a more practical form as a function of the distance $\mathbf{k}$ from the $\mathbf{K}$ or $\mathbf{K}'$ points. Taking as case study the $\mathbf{K}$ point, the wavefunction can be written as:

$$\begin{aligned}\Psi(\mathbf{K}+\mathbf{k},\mathbf{r}) = &\frac{1}{\sqrt{N}}e^{i\theta_A}C_A(\mathbf{K}+\mathbf{k})\sum_{\{\mathbf{R_A}\}} e^{i(\boldsymbol{K}+\boldsymbol{k})\cdot\mathbf{R_A}}\phi_\pi(\mathbf{r}-\mathbf{R_A})+ \\ &\frac{1}{\sqrt{N}}e^{i\theta_B}C_B(\mathbf{K}+\mathbf{k})\sum_{\{\mathbf{R_B}\}} e^{i(\boldsymbol{K}+\boldsymbol{k})\cdot\mathbf{R_B}}\phi_\pi(\mathbf{r}-\mathbf{R_B}).\end{aligned} \tag{2.41}$$

We now introduce the envelope functions $F_{\mathbf{K}\alpha}(\mathbf{k},\mathbf{R}_\alpha)$ defined as:

$$F_{\mathbf{K}\alpha}(\mathbf{k},\mathbf{R}_\alpha) = C_\alpha(\mathbf{K}+\mathbf{k})e^{i\boldsymbol{k}\cdot\mathbf{R}_\alpha}. \tag{2.42}$$

Since the distance $\mathbf{k}$ from the Brillouin zone corners is very small within the region of the Dirac cones, the envelope functions are slowly-varying in direct space with respect to the lattice parameter. The wavefunction of graphene becomes:

$$\begin{aligned}\Psi(\mathbf{K}+\mathbf{k},\mathbf{r}) = \frac{1}{\sqrt{N}} e^{i\theta_A} \sum_{\{\mathbf{R_A}\}} e^{i\boldsymbol{K}\cdot\mathbf{R_A}} F_{\mathbf{K}A}(\mathbf{k},\mathbf{R_A})\phi_\pi(\mathbf{r}-\mathbf{R_A}) + \\ \frac{1}{\sqrt{N}} e^{i\theta_B} \sum_{\{\mathbf{R_B}\}} e^{i\boldsymbol{K}\cdot\mathbf{R_B}} F_{\mathbf{K}B}(\mathbf{k},\mathbf{R_B})\phi_\pi(\mathbf{r}-\mathbf{R_B}).\end{aligned} \tag{2.43}$$

We can now consider the behaviour of the $\phi_\pi(\mathbf{r}-\mathbf{R}_\alpha)$ orbitals on the lattice plane. These orbitals are localised around the atomic sites and decay smoothly in a range of few lattice constants from the center; for larger distances however decay rapidly. This type of functions are usually called smoothing functions. When a smoothing function is multiplied to a generic smooth function, such as the envelope function, the smooth function dependence on the positions can usually be transferred to the smoothing function:

$$F_{\mathbf{K}\alpha}(\mathbf{k},\mathbf{R}_\alpha)\phi_\pi(\mathbf{r}-\mathbf{R}_\alpha) \simeq F_{\mathbf{K}\alpha}(\mathbf{k},\mathbf{r})\phi_\pi(\mathbf{r}-\mathbf{R}_\alpha). \tag{2.44}$$

This approximation relies on the fact that for positions of $\mathbf{r}$ for which the orbital $\phi_\pi(\mathbf{r}-\mathbf{R}_\alpha)$ is not negligible, the envelope function $F_{\mathbf{K}\alpha}(\mathbf{k},\mathbf{r})$ is approximately equal to $F_{\mathbf{K}A}(\mathbf{k},\mathbf{R}_\alpha)$. Instead, for positions further away from $\mathbf{R}_\alpha$, for which $F_{\mathbf{K}\alpha}(\mathbf{k},\mathbf{r})$ would significantly differ to $F_{\mathbf{K}\alpha}(\mathbf{k},\mathbf{R}_\alpha)$, the orbital $\phi_\pi(\mathbf{r}-\mathbf{R}_\alpha)$ is null. As a consequence, the graphene wavefunction can be rewritten as:

$$\begin{aligned}\Psi(\mathbf{K}+\mathbf{k},\mathbf{r}) = \frac{1}{\sqrt{N}} e^{i\theta_A} \sum_{\{\mathbf{R_A}\}} e^{i\boldsymbol{K}\cdot\mathbf{R_A}} F_{\mathbf{K}A}(\mathbf{k},\mathbf{r})\phi_\pi(\mathbf{r}-\mathbf{R_A}) + \\ \frac{1}{\sqrt{N}} e^{i\theta_B} \sum_{\{\mathbf{R_B}\}} e^{i\boldsymbol{K}\cdot\mathbf{R_B}} F_{\mathbf{K}B}(\mathbf{k},\mathbf{r})\phi_\pi(\mathbf{r}-\mathbf{R_B}).\end{aligned} \tag{2.45}$$

Taking out the envelope functions and indicating once again the Bloch states as $\Phi_\alpha(\mathbf{K},\mathbf{r})$, we end up with:

$$\Psi(\mathbf{K}+\mathbf{k},\mathbf{r}) = F_{\mathbf{K}A}(\mathbf{k},\mathbf{r})\Phi_A(\mathbf{K},\mathbf{r}) + F_{\mathbf{K}B}(\mathbf{k},\mathbf{r})\Phi_B(\mathbf{K},\mathbf{r}). \tag{2.46}$$

Thus, the electrons have a spatial wavefunction that approximately is the same one of the $\mathbf{K}$ points. The total wavefunction of graphene includes the contribution of both the $\mathbf{K}$ points:

$$\Psi(\mathbf{k},\mathbf{r}) = \sum_{\alpha=A}^{B} \sum_{\boldsymbol{\tau}=\mathbf{K}}^{\mathbf{K}'} F_{\tau\alpha}(\mathbf{k},\mathbf{r})\Phi_\alpha(\boldsymbol{\tau},\mathbf{r}). \tag{2.47}$$

2.4 Phases of the Bloch states

The Bloch states $\Phi_\alpha(\boldsymbol{\tau}, \mathbf{r})$ appearing in the wavefunction have been defined without specifying the phases. Within the envelope functions formalism, we have reduced to require only the Bloch states of the $\mathbf{K}$ points that are:

$$\begin{aligned}
\Phi_A(\mathbf{K}, \mathbf{r}) &= \frac{1}{\sqrt{N}} \sum_{\{\mathbf{R_A}\}} e^{i\mathbf{K}\cdot\mathbf{R_A}} \phi_\pi(\mathbf{r} - \mathbf{R_A}), \\
\Phi_B(\mathbf{K}, \mathbf{r}) &= \frac{1}{\sqrt{N}} e^{i\theta_1} \sum_{\{\mathbf{R_B}\}} e^{i\mathbf{K}\cdot\mathbf{R_B}} \phi_\pi(\mathbf{r} - \mathbf{R_B}), \\
\Phi_A(\mathbf{K}', \mathbf{r}) &= \frac{1}{\sqrt{N}} e^{i\theta_2} \sum_{\{\mathbf{R_A}\}} e^{i\mathbf{K}'\cdot\mathbf{R_A}} \phi_\pi(\mathbf{r} - \mathbf{R_A}), \\
\Phi_B(\mathbf{K}', \mathbf{r}) &= \frac{1}{\sqrt{N}} e^{i\theta_3} \sum_{\{\mathbf{R_B}\}} e^{i\mathbf{K}'\cdot\mathbf{R_B}} \phi_\pi(\mathbf{r} - \mathbf{R_B}).
\end{aligned} \tag{2.48}$$

The phases of these four Bloch states can be determined working with the symmetries of the graphene lattice [128, 129]. Since only the relative phases matter, we let the $\Phi_A(\mathbf{K}, \mathbf{r})$ state phase-free. The main spacial symmetries of the graphene lattice are:

- translations by unit vectors
- symmetries of the point group of the triangle C_{3v} consisting of rotations and reflections around the origin. The rotations that leave the system unchanged are of multiples of $\frac{2\pi}{3}$. The reflections axes depend on the system of reference chosen, in our case the axes are along the directions $\frac{\pi}{6}$,$\frac{\pi}{2}$ and $\frac{5\pi}{6}$.
- C_2 inversion symmetry, that for a plane is equivalent to a π rotation around the z axis.

We can consider the effects of these symmetries on the Bloch states. For what concerns the translations, it is clear that in the tight-binding theory the translational symmetry is kept automatically into account. Thus, this symmetry is already conserved.
We can then move to the symmetries of the point group of the triangle. In principle, we should study these transformations with respect to any center of the hexagons. However, thanks to the translational symmetry of graphene, we can limit to perform all these operation only once. Thus, we write down the symmetries of the point group of the triangle C_{3v} in our system of reference. The

rotations are made up, less for the identity, of two cases: either a rotation by $\frac{2\pi}{3}$ or a rotation by $-\frac{2\pi}{3}$. The general law of transformation for rotations is:

$$Rot\left(\theta\right)=\begin{pmatrix}\cos\left(\theta\right) & -\sin\left(\theta\right)\\ \sin\left(\theta\right) & \cos\left(\theta\right)\end{pmatrix} \tag{2.49}$$

So the symmetric rotations are:

$$Rot\left(\frac{2\pi}{3}\right)=\begin{pmatrix}-\frac{1}{2} & -\frac{\sqrt{3}}{2}\\ \frac{\sqrt{3}}{2} & -\frac{1}{2}\end{pmatrix}, \tag{2.50}$$

and

$$Rot\left(-\frac{2\pi}{3}\right)=\begin{pmatrix}-\frac{1}{2} & \frac{\sqrt{3}}{2}\\ -\frac{\sqrt{3}}{2} & -\frac{1}{2}\end{pmatrix}. \tag{2.51}$$

A reflection with respect to a generic direction θ is:

$$Ref\left(\theta\right)=\begin{pmatrix}\cos\left(2\theta\right) & \sin\left(2\theta\right)\\ \sin\left(2\theta\right) & -\cos\left(2\theta\right)\end{pmatrix}. \tag{2.52}$$

The three symmetric reflections are:

$$Ref\left(\frac{\pi}{6}\right)=\begin{pmatrix}\frac{1}{2} & \frac{\sqrt{3}}{2}\\ \frac{\sqrt{3}}{2} & -\frac{1}{2}\end{pmatrix}, \tag{2.53}$$

$$Ref\left(\frac{\pi}{2}\right)=\begin{pmatrix}-1 & 0\\ 0 & 1\end{pmatrix}, \tag{2.54}$$

$$Ref\left(\frac{5\pi}{6}\right)=\begin{pmatrix}\frac{1}{2} & -\frac{\sqrt{3}}{2}\\ -\frac{\sqrt{3}}{2} & -\frac{1}{2}\end{pmatrix}. \tag{2.55}$$

The four Bloch states appearing in the wavefunction are referred to the $\mathbf{K}$ and $\mathbf{K}'$ point of the Brillouin zone. These two points generally transform under the action of the symmetry operations. We then compute the new value of the two $\mathbf{K}$ points after the transformations; the effect of the symmetry operations is shown even from a graphical point of view in Fig. 2.5 in the same order.

$$\begin{array}{ccc} Rot\left(0\right)\mathbf{K}=\mathbf{K} & Rot\left(\frac{2\pi}{3}\right)\mathbf{K}=\mathbf{K}-\mathbf{b_1}+\mathbf{b_2} & Rot\left(-\frac{2\pi}{3}\right)\mathbf{K}=\mathbf{K}-\mathbf{b_1}\\ Ref\left(\frac{\pi}{6}\right)\mathbf{K}=\mathbf{K} & Ref\left(\frac{\pi}{2}\right)\mathbf{K}=\mathbf{K}-\mathbf{b_1}+\mathbf{b_2} & Ref\left(\frac{5\pi}{6}\right)\mathbf{K}=\mathbf{K}-\mathbf{b_1}\end{array} \tag{2.56}$$

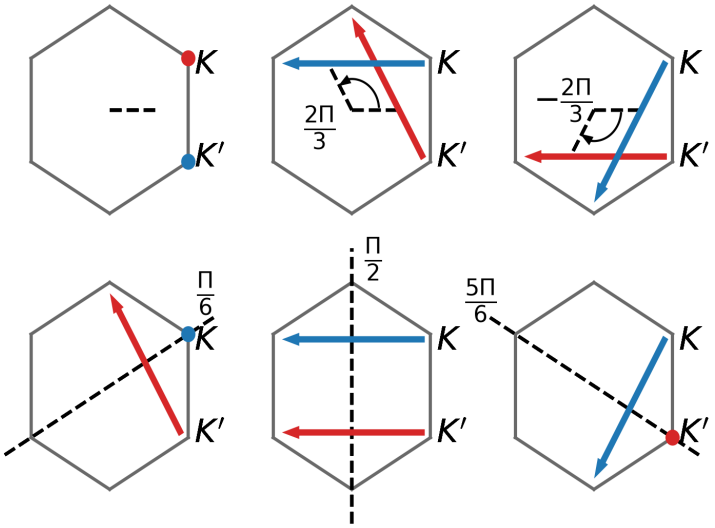

Figure 2.5: Pictorial representation of the action in reciprocal space of the symmetries of the point group of the triangle C_{3v} on the $\mathbf{K}$ and $\mathbf{K}'$ points of the Brillouin zone. In the upper row appear the rotations, in the lower row the reflections.

$$\begin{array}{ccc} Rot\,(0)\,\mathbf{K}' = \mathbf{K}' & Rot\left(\frac{2\pi}{3}\right)\mathbf{K}' = \mathbf{K}' + \mathbf{b_2} & Rot\left(-\frac{2\pi}{3}\right)\mathbf{K}' = \mathbf{K}' + \mathbf{b_2} - \mathbf{b_1} \\ Ref\left(\frac{\pi}{6}\right)\mathbf{K}' = \mathbf{K}' + \mathbf{b_2} & Ref\left(\frac{\pi}{2}\right)\mathbf{K}' = \mathbf{K}' + \mathbf{b_2} - \mathbf{b_1} & Ref\left(\frac{5\pi}{6}\right)\mathbf{K}' = \mathbf{K}' \end{array} \tag{2.57}$$

All the symmetry operations of the point group of the triangle applied to either one of the two $\mathbf{K}$ points transform the $\mathbf{K}$ point into themselves or one of other $\mathbf{K}$ points of the same type. The symmetry operations are diagonal in the space of the Dirac valleys. We can then define two pseudospinors, that have respectively as components the two Bloch states of the $\mathbf{K}$ and $\mathbf{K}'$ valley:

$$\begin{aligned} \Phi(\mathbf{K},\mathbf{r}) &= \begin{pmatrix} \Phi_A(\mathbf{K},\mathbf{r}) \\ \Phi_B(\mathbf{K},\mathbf{r}) \end{pmatrix}, \\ \Phi(\mathbf{K}',\mathbf{r}) &= \begin{pmatrix} \Phi_A(\mathbf{K}',\mathbf{r}) \\ \Phi_B(\mathbf{K}',\mathbf{r}) \end{pmatrix}. \end{aligned} \tag{2.58}$$

We demand that the two pseudospinors transform as valley-specific irreducible representations of the C_{3v} symmetry operations. This means that the action of any of the C_{3v} symmetry operations on the two pseudospinors can be represented

as the product of a 2×2 matrix with the pseudospinors. The six 2×2 matrices of the symmetry operations are valley dependent and constitute two different 2×2 irreducible representations of C_{3v}. We indicate with M(R) and M'(R) the matrices of the symmetry operations on the $\mathbf{K}$ and $\mathbf{K}'$ pseudospinors. Under any of the symmetry operations, the pseudospinors have to transform as:

$$\begin{aligned} R\Phi(\mathbf{K},\mathbf{r}) &= [M(R)]^T \begin{pmatrix} \Phi_A(\mathbf{K},\mathbf{r}) \\ \Phi_B(\mathbf{K},\mathbf{r}) \end{pmatrix}, \\ R\Phi(\mathbf{K}',\mathbf{r}) &= [M'(R)]^T \begin{pmatrix} \Phi_A(\mathbf{K}',\mathbf{r}) \\ \Phi_B(\mathbf{K}',\mathbf{r}) \end{pmatrix}. \end{aligned} \tag{2.59}$$

Before computing the elements of the six M(R) and M'(R) matrices, we can already draw some conclusions on their shape studying how the rotations and reflections act in real space. To help the reading, we depict from a graphical point of view the effect of a rotation a reflection in real space in Fig. 2.6. The three rotations move a carbon atom of the A or B sublattice on the old sites of a carbon atom belonging to the same sublattice. The sublattice index of the graphene atoms is then conserved during a rotation and the transformation matrix only features diagonal elements. During a reflection, instead, the positions of A and B sites are mirrored. Hence, the transformation matrix of a reflection only contains out-of diagonal components.

We are now ready to derive the symmetry matrices. The procedure of the derivation is as follows: we apply the symmetry operations to each $\Phi_\alpha(\boldsymbol{\tau},\mathbf{r})$ and then we write the resulting operations from a matrix point of view through the pseudospinors. Here, we limit to write down the effect of the symmetry operations only for the Bloch state $\Phi_A(\mathbf{K},\mathbf{r})$. For the other Bloch states, the results can be

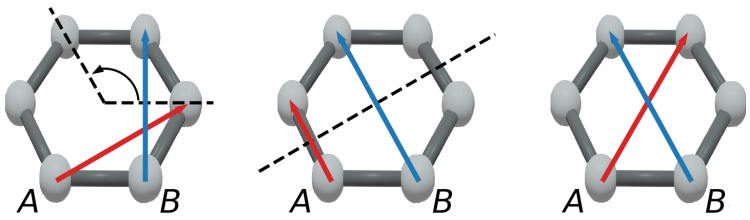

Figure 2.6: Pictorial representation, in order, of the action of a rotation, a reflection and the inversion symmetry on the graphene hexagon. The two sublattice do not exchange only under rotations.

found just proceeding by analogy.

$$
\begin{aligned}
&Rot\,(0)\,\Phi_A(\mathbf{K},\mathbf{r}) = \Phi_A(\mathbf{K},\mathbf{r}),\\
&Rot\left(\frac{2\pi}{3}\right)\Phi_A(\mathbf{K},\mathbf{r}) = \Phi_A(\mathbf{K}-\mathbf{b_1}+\mathbf{b_2},\mathbf{r}) = e^{i\frac{2\pi}{3}}\Phi_A(\mathbf{K}-\mathbf{b_1}+\mathbf{b_2},\mathbf{r}),\\
&Rot\left(-\frac{2\pi}{3}\right)\Phi_A(\mathbf{K},\mathbf{r}) = \Phi_A(\mathbf{K}-\mathbf{b_1},\mathbf{r}) = e^{-i\frac{2\pi}{3}}\Phi_A(\mathbf{K}-\mathbf{b_1}+\mathbf{b_2},\mathbf{r}),\\
&Ref\left(\frac{\pi}{6}\right)\Phi_A(\mathbf{K},\mathbf{r}) = e^{-i\theta_2}\Phi_B(\mathbf{K},\mathbf{r}),\\
&Ref\left(\frac{\pi}{2}\right)\Phi_A(\mathbf{K},\mathbf{r}) = e^{-i\theta_2}\Phi_B(\mathbf{K}-\mathbf{b_1}+\mathbf{b_2},\mathbf{r}) = e^{-i\theta_2}e^{i\frac{2\pi}{3}}\Phi_B(\mathbf{K},\mathbf{r}),\\
&Ref\left(\frac{5\pi}{6}\right)\Phi_A(\mathbf{K},\mathbf{r}) = e^{-i\theta_2}\Phi_B(\mathbf{K}-\mathbf{b_1},\mathbf{r}) = e^{-i\theta_2}e^{-i\frac{2\pi}{3}}\Phi_B(\mathbf{K},\mathbf{r}).
\end{aligned}
\tag{2.60}
$$

From now on, we will indicate $e^{i\frac{2\pi}{3}}$ as ω. It is instructive to notice that the effect of the symmetry operations can be guessed just combining the result of the operations in Eq.(2.56-2.57) and how the symmetries act in real space.

Once performed the symmetry operations to all $\Phi_\alpha(\boldsymbol{\tau},\mathbf{r})$, we can find the expression of the six M matrices of the $\mathbf{K}$ valley.

$$
\begin{aligned}
M(Rot(0)) &= \begin{pmatrix} 1 & 0 \\ 0 & 1 \end{pmatrix} & M\left(Rot\left(\tfrac{2\pi}{3}\right)\right) &= \begin{pmatrix} \omega & 0 \\ 0 & \omega^{-1} \end{pmatrix}\\
M\left(Rot\left(-\tfrac{2\pi}{3}\right)\right) &= \begin{pmatrix} \omega^{-1} & 0 \\ 0 & \omega \end{pmatrix} & M\left(Ref\left(\tfrac{\pi}{6}\right)\right) &= \begin{pmatrix} 0 & e^{i\theta_2} \\ e^{-i\theta_2} & 0 \end{pmatrix}\\
M\left(Ref\left(\tfrac{\pi}{2}\right)\right) &= \begin{pmatrix} 0 & \omega^{-1}e^{i\theta_2} \\ \omega e^{-i\theta_2} & 0 \end{pmatrix} & M\left(Rot\left(\tfrac{5\pi}{6}\right)\right) &= \begin{pmatrix} 0 & \omega e^{i\theta_2} \\ \omega^{-1}e^{-i\theta_2} & 0 \end{pmatrix}
\end{aligned}
\tag{2.61}
$$

If we set $e^{i\theta_2} = -\omega^{-1}$, we have that:

$$
\begin{aligned}
&M\left(Ref\left(\frac{\pi}{6}\right)\right) = \begin{pmatrix} 0 & -\omega^{-1} \\ -\omega & 0 \end{pmatrix} M\left(Ref\left(\frac{\pi}{2}\right)\right) = \begin{pmatrix} 0 & -\omega \\ -\omega^{-1} & 0 \end{pmatrix}\\
&M\left(Rot\left(\frac{5\pi}{6}\right)\right) = \begin{pmatrix} 0 & -1 \\ -1 & 0 \end{pmatrix}
\end{aligned}
\tag{2.62}
$$

With this choice of phase, the six M matrices are exactly the representation of the C_{3v} symmetry operations on the basis of vectors:

$$
\begin{pmatrix} x-iy \\ x+iy \end{pmatrix}, \tag{2.63}
$$

that transform according to:

$$
R\begin{pmatrix} x-iy \\ x+iy \end{pmatrix} = [M(R)]^T\begin{pmatrix} x-iy \\ x+iy \end{pmatrix} \tag{2.64}
$$

We now move to the $\mathbf{K}'$ valley. The six symmetry matrices M' are:

$$\begin{aligned} M'(Rot(0)) &= \begin{pmatrix} 1 & 0 \\ 0 & 1 \end{pmatrix} & M'\left(Rot\left(\tfrac{2\pi}{3}\right)\right) &= \begin{pmatrix} \omega^{-1} & 0 \\ 0 & \omega \end{pmatrix} \\ M'\left(Rot\left(-\tfrac{2\pi}{3}\right)\right) &= \begin{pmatrix} \omega & 0 \\ 0 & \omega^{-1} \end{pmatrix} & M'\left(Ref\left(\tfrac{\pi}{6}\right)\right) &= \begin{pmatrix} 0 & \omega^{-1}e^{-i(\theta_3-\theta_4)} \\ \omega e^{i(\theta_3-\theta_4)} & 0 \end{pmatrix} \\ M'\left(Ref\left(\tfrac{\pi}{2}\right)\right) &= \begin{pmatrix} 0 & \omega e^{-i(\theta_3-\theta_4)} \\ \omega^{-1}e^{i(\theta_3-\theta_4)} & 0 \end{pmatrix} & M'\left(Rot\left(\tfrac{5\pi}{6}\right)\right) &= \begin{pmatrix} 0 & e^{-i(\theta_3-\theta_4)} \\ e^{i(\theta_3-\theta_4)} & 0 \end{pmatrix} \end{aligned} \tag{2.65}$$

Here, by setting $e^{i(\theta_3-\theta_4)} = \omega$, we have that:

$$\begin{aligned} M'\left(Ref\left(\frac{\pi}{6}\right)\right) &= \begin{pmatrix} 0 & \omega \\ \omega^{-1} & 0 \end{pmatrix} \quad M'\left(Ref\left(\frac{\pi}{2}\right)\right) = \begin{pmatrix} 0 & 1 \\ 1 & 0 \end{pmatrix} \\ M'\left(Rot\left(\frac{5\pi}{6}\right)\right) &= \begin{pmatrix} 0 & \omega^{-1} \\ \omega & 0 \end{pmatrix} \end{aligned} \tag{2.66}$$

The M' matrices so built are the representation the representation of the C_{3v} on the basis of vectors

$$\begin{pmatrix} x+iy \\ -x+iy \end{pmatrix}, \tag{2.67}$$

that transform according to:

$$R\begin{pmatrix} x+iy \\ -x+iy \end{pmatrix} = [M'(R)]^T \begin{pmatrix} x+iy \\ -x+iy \end{pmatrix} \tag{2.68}$$

With the choices made for the phases, the the two sets of transformation matrices M and M' are isomorphisms of the $\mathbf{K}$ and $\mathbf{K}'$ points. The relative phase factors within the pseudospinors are then:

$$\begin{aligned} e^{i\theta_2} &= -\omega^{-1} \\ e^{i\theta_4} &= \omega^{-1}e^{i\theta_3} \end{aligned} \tag{2.69}$$

We remain with a last unknown phase θ_3 between Bloch states of different valleys. The remaining phase is determined exploiting the inversion symmetry $\mathbb{I}$:

$$\mathbb{I} : \mathbf{r} \to -\mathbf{r}. \tag{2.70}$$

In real space, the inversion symmetry swaps A and B sites, as we see from the third image in Fig. 2.6. In reciprocal space, instead, the inversion symmetry flips $\mathbf{K}$ and $\mathbf{K}'$ points, enabling to establish a link between the wavefunctions of the two valleys.

$$\mathbb{I}\mathbf{K} = \mathbf{K}' + \mathbf{b_2} - \mathbf{b_1}, \tag{2.71}$$

$$\mathbb{I}\mathbf{K}' = \mathbf{K} + \mathbf{b_2} - \mathbf{b_1}. \tag{2.72}$$

The wavefunction must be conserved under the inversion symmetry:

$$\mathbb{I}(\Phi_A(\mathbf{K},\mathbf{r})) = \Phi_B(\mathbf{K}',\mathbf{r}). \tag{2.73}$$

$$\begin{aligned}\mathbb{I}(\Phi_A(\mathbf{K},\mathbf{r})) &= \frac{1}{\sqrt{N}}\sum_{n_1,n_2} e^{i\mathbb{I}(\mathbf{K})\cdot\mathbb{I}(\mathbf{R_A})}\phi_\pi(\mathbf{r}-\mathbb{I}(\mathbf{R_A})) \\ &= \frac{1}{\sqrt{N}}\sum_{n_1,n_2} e^{i(\mathbf{K'}+\mathbf{b_2}-\mathbf{b_1})\cdot(-n_1\mathbf{a_1}-n_2\mathbf{a_1}-\mathbf{R_{0A}})}\phi_\pi(\mathbf{r}-(-n_1\mathbf{a_1}-n_2\mathbf{a_2}-\mathbf{R_{0A}})).\end{aligned} \tag{2.74}$$

Now recalling that $\mathbf{R_{0A}} = -\mathbf{R_{0B}}$, and updating the dumb indices n_1 and n_2, we can write:

$$\begin{aligned}\mathbb{I}(\Phi_A(\mathbf{K},\mathbf{r})) &= \frac{1}{\sqrt{N}}\sum_{n_1,n_2} e^{-i(\mathbf{K'}+\mathbf{b_2}-\mathbf{b_1})\cdot(n_1\mathbf{a_1}+n_2\mathbf{a_2}+\mathbf{R_{0B}})}\phi_\pi(\mathbf{r}-(n_1\mathbf{a_1}+n_2\mathbf{a_2}+\mathbf{R_{0B}})) \\ \mathbb{I}(\Phi_A(\mathbf{K},\mathbf{r})) &= \frac{1}{\sqrt{N}}\sum_{n_1,n_2} e^{-i(\mathbf{K'}+\mathbf{b_2}-\mathbf{b_1})\cdot\mathbf{R_B}}\phi_\pi(\mathbf{r}-\mathbf{R_B}) \\ \mathbb{I}(\Phi_A(\mathbf{K},\mathbf{r})) &= \frac{1}{\sqrt{N}}\omega^{-1}\sum_{n_1,n_2} e^{-i\mathbf{K'}\cdot\mathbf{R_B}}\phi_\pi(\mathbf{r}-\mathbf{R_B})\end{aligned} \tag{2.75}$$

The term at left is exactly $\Phi_B(\mathbf{K}',\mathbf{r})$ provided that $e^{-i\theta_3}\omega^{-1} = \omega^{-1}$ meaning that $e^{i\theta_3}$ is simply 1. The full expression of the Bloch states is:

$$\begin{aligned}\Phi_A(\mathbf{K},\mathbf{r}) &= \frac{1}{\sqrt{N}}\sum_{\{\mathbf{R_A}\}} e^{i\mathbf{K}\cdot\mathbf{R_A}}\phi_\pi(\mathbf{r}-\mathbf{R_A}), \\ \Phi_B(\mathbf{K},\mathbf{r}) &= -\frac{1}{\sqrt{N}}\omega^{-1}\sum_{\{\mathbf{R_B}\}} e^{i\mathbf{K}\cdot\mathbf{R_B}}\phi_\pi(\mathbf{r}-\mathbf{R_B}), \\ \Phi_A(\mathbf{K}',\mathbf{r}) &= \frac{1}{\sqrt{N}}\sum_{\{\mathbf{R_A}\}} e^{i\mathbf{K}'\cdot\mathbf{R_A}}\phi_\pi(\mathbf{r}-\mathbf{R_A}), \\ \Phi_B(\mathbf{K}',\mathbf{r}) &= \frac{1}{\sqrt{N}}\omega^{-1}\sum_{\{\mathbf{R_B}\}} e^{i\mathbf{K}'\cdot\mathbf{R_B}}\phi_\pi(\mathbf{r}-\mathbf{R_B}),\end{aligned} \tag{2.76}$$

2.5 Full Schrödinger Equation of graphene

We now derive the effective Schrödinger equation for the envelope functions $F_{\boldsymbol{\tau}\alpha}(\mathbf{k},\mathbf{r})$. The envelope functions have been defined through the coefficients

$C_A(\boldsymbol{\tau}+\mathbf{k})$ and $C_B(\boldsymbol{\tau}+\mathbf{k})$ (where τ is either $\mathbf{K}$ or $\mathbf{K}'$), eigenstates of the secular equation. These coefficients respect an equation to the eigenvalues:

$$\begin{cases} t\, e^{i(\theta_{\tau A}-\theta_{\tau B})}\alpha(\boldsymbol{\tau}+\mathbf{k})C_B(\boldsymbol{\tau}+\mathbf{k}) = E\, C_A(\boldsymbol{\tau}+\mathbf{k}), \\ t\, e^{-i(\theta_{\tau A}-\theta_{\tau B})}\alpha^*(\boldsymbol{\tau}+\mathbf{k})C_A(\boldsymbol{\tau}+\mathbf{k}) = E\, C_B(\boldsymbol{\tau}+\mathbf{k}), \end{cases} \tag{2.77}$$

where the phases θ are those defined in Eq. (2.76). Starting from this equation for the coefficients, we can write down similar relations for the envelope functions. It is important to remember that the relations for the envelope functions are valid only in the region of the two Dirac cones where the approximation of the envelope functions holds. We first look at the equation for the envelope functions in the $\mathbf{K}$ valley:

$$\begin{cases} -t\,\omega^{-1}\,\alpha(\mathbf{K}+\mathbf{k})F_{\mathbf{K}B}(\mathbf{k},\mathbf{r}) = EF_{\mathbf{K}A}(\mathbf{k},\mathbf{r}), \\ -t\,\omega\,\alpha^*(\mathbf{K}+\mathbf{k})F_{\mathbf{K}A}(\mathbf{k},\mathbf{r}) = EF_{\mathbf{K}B}(\mathbf{k},\mathbf{r}). \end{cases} \tag{2.78}$$

We expand the function $\alpha(\mathbf{K}+\mathbf{k})$ at first order in the neighbourhood of the $\mathbf{K}$ point since the wavevector $\mathbf{k}$ is small:

$$\begin{aligned} \alpha(\mathbf{K}+\mathbf{k}) &= e^{\frac{i\left(\frac{2\pi}{a\sqrt{3}}+k_x\right)a}{\sqrt{3}}} + 2e^{-\frac{i\left(\frac{2\pi}{a\sqrt{3}}+k_x\right)a}{2\sqrt{3}}}\cos\left(\frac{a}{2}\left(\frac{2\pi}{3a}+k_y\right)\right), \\ &\simeq \left(-\frac{1}{2}+i\frac{\sqrt{3}}{2}\right)\left(1+i\frac{a}{\sqrt{3}}k_x\right)+\left(\frac{1}{2}-i\frac{\sqrt{3}}{2}\right)\left(1-i\frac{a}{2\sqrt{3}}k_x\right)\left(1-\frac{\sqrt{3}a}{2}k_y\right). \end{aligned} \tag{2.79}$$

Neglecting mixed products, it becomes:

$$\alpha(\mathbf{K}+\mathbf{k}) \simeq \frac{\sqrt{3}a}{2}\left(-\frac{1}{2}+i\frac{\sqrt{3}}{2}\right)(ik_x+k_y) = \frac{\sqrt{3}a}{2}\omega(ik_x+k_y). \tag{2.80}$$

The envelope functions $F_{\mathbf{K}\alpha}(\mathbf{k},\mathbf{r})$ then follow the equation:

$$\begin{cases} -t\frac{\sqrt{3}a}{2}(ik_x+k_y)F_{\mathbf{K}B}(\mathbf{k},\mathbf{r}) = EF_{\mathbf{K}A}(\mathbf{k},\mathbf{r}), \\ -t\frac{\sqrt{3}a}{2}(-ik_x+k_y)F_{\mathbf{K}A}(\mathbf{k},\mathbf{r}) = EF_{\mathbf{K}B}(\mathbf{k},\mathbf{r}). \end{cases} \tag{2.81}$$

We now repeat the same procedure in the K' valley. We start by looking again at the equation for the envelope functions once introduced the phases of the Bloch states:

$$\begin{cases} t\omega^{-1}\alpha(\mathbf{K}'+\mathbf{k})F_{\mathbf{K}'B}(\mathbf{k},\mathbf{r}) = EF_{\mathbf{K}'A}(\mathbf{k},\mathbf{r}), \\ t\omega\alpha^*(\mathbf{K}'+\mathbf{k})F_{\mathbf{K}'A}(\mathbf{k},\mathbf{r}) = EF_{\mathbf{K}'B}(\mathbf{k},\mathbf{r}). \end{cases} \tag{2.82}$$

We then expand the function $\alpha(\mathbf{K}' + \mathbf{k})$ at first order in the region of the Dirac cones:

$$\begin{aligned}\alpha(\mathbf{K}' + \mathbf{k}) &= e^{\frac{i\left(\frac{2\pi}{a\sqrt{3}}+k_x\right)a}{\sqrt{3}}} + 2e^{-\frac{i\left(\frac{2\pi}{a\sqrt{3}}+k_x\right)a}{2\sqrt{3}}}\cos\left(\frac{a}{2}\left(-\frac{2\pi}{3a}+k_y\right)\right), \\ &\simeq \left(-\frac{1}{2}+i\frac{\sqrt{3}}{2}\right)\left(1+i\frac{a}{\sqrt{3}}k_x\right)+\left(\frac{1}{2}-i\frac{\sqrt{3}}{2}\right)\left(1-i\frac{a}{2\sqrt{3}}k_x\right)\left(1+\frac{\sqrt{3}a}{2}k_y\right).\end{aligned} \tag{2.83}$$

Neglecting once again the mixed products, we get:

$$\alpha(\mathbf{K}' + \mathbf{k}) \simeq \frac{\sqrt{3}a}{2}\left(-\frac{1}{2}+i\frac{\sqrt{3}}{2}\right)(ik_x - k_y) = -\frac{\sqrt{3}a}{2}\omega(-ik_x + k_y). \tag{2.84}$$

The eigenstates equation for the envelope functions $F_{\mathbf{K}'\alpha}(\mathbf{k}, \mathbf{r})$ then is:

$$\begin{cases} -t\frac{\sqrt{3}a}{2}(-ik_x + k_y)F_{\mathbf{K}'B}(\mathbf{k}, \mathbf{r}) = EF_{\mathbf{K}'A}(\mathbf{k}, \mathbf{r}), \\ -t\frac{\sqrt{3}a}{2}(ik_x + k_y)F_{\mathbf{K}'A}(\mathbf{k}, \mathbf{r}) = EF_{\mathbf{K}'B}(\mathbf{k}, \mathbf{r}). \end{cases} \tag{2.85}$$

We introduce $\gamma = -t\frac{\sqrt{3}a}{2}$ with γ positive, being the tight-binding parameter t negative. Recalling the relation between the tight-binding parameter and the Fermi velocity of the Dirac cones, we can also write that $\gamma = \hbar v_F$.

At this stage, we can write in a unified expression the eigenstates equation for the envelope function in the two K valleys. This gives the expression of the full Schrödinger equation of graphene in the $k \cdot p$ approximation:

$$\gamma\begin{pmatrix} 0 & k_y + ik_x & 0 & 0 \\ k_y - ik_x & 0 & 0 & 0 \\ 0 & 0 & 0 & k_y - ik_x \\ 0 & 0 & k_y + ik_x & 0 \end{pmatrix}\begin{pmatrix} F_{\mathbf{K}A}(\mathbf{k}, \mathbf{r}) \\ F_{\mathbf{K}B}(\mathbf{k}, \mathbf{r}) \\ F_{\mathbf{K}'A}(\mathbf{k}, \mathbf{r}) \\ F_{\mathbf{K}'B}(\mathbf{k}, \mathbf{r}) \end{pmatrix} = E\begin{pmatrix} F_{\mathbf{K}A}(\mathbf{k}, \mathbf{r}) \\ F_{\mathbf{K}B}(\mathbf{k}, \mathbf{r}) \\ F_{\mathbf{K}'A}(\mathbf{k}, \mathbf{r}) \\ F_{\mathbf{K}'B}(\mathbf{k}, \mathbf{r}) \end{pmatrix} \tag{2.86}$$

In the next chapter, we will start from this equation to compute the energy and the eigenstates of carbon nanotubes.

Chapter 3

The effective mass theory of Carbon Nanotubes

The aim of this chapter is to illustrate the effective-mass theory for single-wall carbon nanotubes. We start with a brief analysis of the geometrical properties of single-wall carbon nanotubes. We then derive the effective mass states of single-wall carbon nanotubes using the graphene states built in the previous Chapter. In the end, we will limit to consider the lowest-energy states due to our interest in transport properties of single-wall carbon nanotubes.

3.1 Geometry of a nanotube

Geometrically, single-wall carbon nanotube are graphene strips rolled up in a cylindrical form (Fig. 3.1). The typical dimensions of the diameters of the cylin-

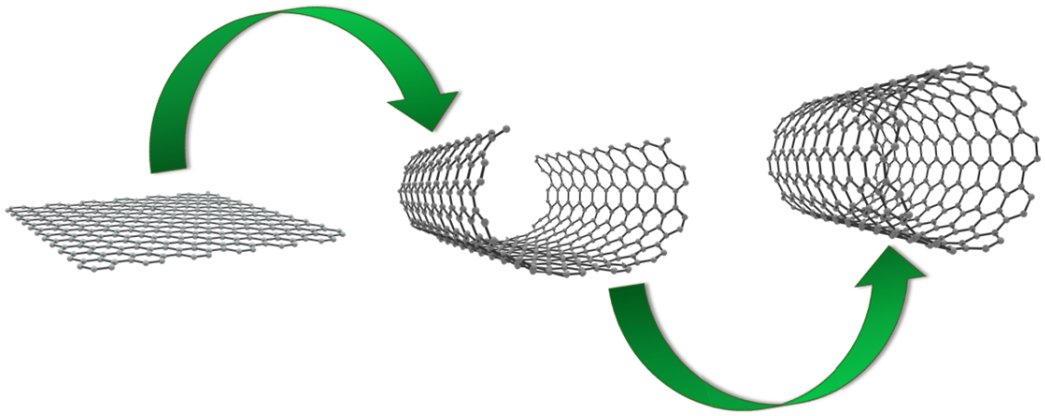

Figure 3.1: Single-wall carbon nanotubes are wrapped up graphene sheets. Nanotubes are classified based on the way of folding.

ders are in the order of few nm. The rolling, except in the smallest tubes, only slightly modifies the interatomic distances between the carbon atoms and hence approximatively the lattice of graphene and of carbon nanotubes can be considered as analogous. Thus, a single-wall carbon nanotube has basically the same microscopic structure of flat graphene with the main difference that the honeycomb lattice is now spread over a cylindrical surface and confined along the curved direction. In order to describe nanotubes, we can define the circumferential vector $\mathbf{C}$ as the chiral vector between a pair of atoms of the same sublattice on the graphene layer which, when rolled onto each other, form the nanotube:

$$\mathbf{C} = (n+m)\mathbf{a_1} + m\mathbf{a_2}, \tag{3.1}$$

where $\mathbf{a_1}$ and $\mathbf{a_2}$ are the graphene lattice vector (Eq.(2.1)). To any chiral vector $\mathbf{C}$ corresponds a unique pair of indices (n, m). The chiral vector $\mathbf{C}$ is the circumference of the nanotube, hence the nanotube radius amounts to:

$$R = \frac{|\mathbf{C}|}{2\pi} = \frac{\sqrt{n^2+m^2+nm}}{2\pi}. \tag{3.2}$$

An other important parameter is the chiral angle θ, that spans the area between $\mathbf{C}$ and the lattice vector $\mathbf{a_1}$:

$$\cos\theta = \frac{\mathbf{C}\cdot\mathbf{a_1}}{|\mathbf{C}||\mathbf{a_1}|} = \frac{2n+m}{2\sqrt{n^2+m^2+nm}}. \tag{3.3}$$

The chiral angle corresponds to the tilt of the hexagonal cells with respect to the nanotube axis. The chiral angle ranges between $0°$ and $30°$ for the hexagonal symmetry of the honeycomb lattice. At $0°$ and $30°$, there are two special types of nanotubes respectively called zigzag and armchair. The two names refer to the line-shape created by the carbon atoms along the circumference. In zigzag nanotubes, that have indices $(n, 0)$ and $\theta = 0°$, the hexagonal cells stack vertically and the carbon-carbon bonds are parallel to the nanotube axis. Whereas, in armchair tubes, that have indices (n, n) and $\theta = 30°$, the hexagonal cells stack horizontally and the carbon-carbon bonds are perpendicular to the nanotube axis. Both zigzag and armchair nanotubes are called achiral tubes because they possess mirror symmetry. All the other nanotubes are, instead, called chiral.

The unit cell of carbon nanotubes is not univocally defined. The most common choices are working with a translational unit cell or an helical unit cell. Here, we work with the translational unit cell, that is the most immediate. The translational unit cell is built through the chiral vector $\mathbf{C}$ and the smallest lattice vector $\mathbf{T}$ perpendicular to $\mathbf{C}$. On the graphene plane, the translational unit cell corresponds to a rectangle. The vector $\mathbf{T}$ is defined as:

$$\mathbf{T} = t_1\mathbf{a_1} + t_2\mathbf{a_2}, \tag{3.4}$$

with

$$t_1 = \frac{2m+n}{d_R}, \quad t_2 = \frac{n-m}{d_R}, \tag{3.5}$$

where d_R is the greatest common divisor between $2m+n$ and $2n+m$. The modulus of the translational vector defines the length t that is the translational period along the tube axis:

$$t = |\mathbf{T}| = a\frac{\sqrt{3(n^2+nm+m^2)}}{d_R}. \tag{3.6}$$

The nanotube unit cell is thus formed by a cylindrical surface with height t and circumference $\mathbf{C}$. The number of primitive graphene unit cells contained within a single translational unit cell is:

$$N = \frac{|\mathbf{C}\times\mathbf{T}|}{|\mathbf{a_1}\times\mathbf{a_2}|} = \frac{2(n^2+nm+m^2)}{d_R}. \tag{3.7}$$

As the translational unit cell is N times bigger than the unit cell of flat graphene, the translational reciprocal cell is N times smaller than the Brillouin zone of graphene. This affects the energy dispersion. In order to retrieve the energy dispersion of the carbon nanotube, one must perform N foldings of the energy dispersion of flat graphene. This leads to the formation of N bands in the carbon nanotube.

3.2 Nanotube reference frame

In the previous chapter, we have developed the effective mass theory of graphene in the (x,y) reference frame that allows to best exploit the symmetry properties of the honeycomb lattice. This has helped us to determine the relative phases between the Bloch wavefunctions. In order to extend the effective mass theory to carbon nanotubes, it is more suitable to make a change of the (x,y) reference frame. The optimal choice is taking a (x,y) reference frame centred on an atom of the B sublattice with the axes parallel to the vectors of the translational unit cell. This choice makes easier to describe the effect of the rolling of the graphene plane along the chiral vector direction and to determine the boundary condition.
In order to pass from the current (x,y) reference frame to the new reference frame, we have to perform three transformations: a rotation of $-\frac{\pi}{2}$, a translation and at last an other rotation to superimpose the x axis on the direction of the chiral vector $\mathbf{C}$. The change of the (x,y) reference frame causes modifications of the phases both in the $\mathbf{k}\cdot\mathbf{p}$ equation and in the Bloch functions. As we have to perform two rotations, we start by analysing the effects of this transformation.

Let us consider a rotation of an angle β. A vector $\mathbf{r}$ of coordinates (x, y) in the old reference frame transforms in the new reference frame to the coordinates (x', y') according to:

$$\begin{pmatrix} x' \\ y' \end{pmatrix} = Rot(-\beta) \begin{pmatrix} x \\ y \end{pmatrix} = \begin{pmatrix} \cos(\beta) & \sin(\beta) \\ -\sin(\beta) & \cos(\beta) \end{pmatrix} \begin{pmatrix} x \\ y \end{pmatrix}. \tag{3.8}$$

Based on the transformations rules of $\mathbf{r}$, we can derive straightforwardly the transformation of the differential operators:

$$\begin{pmatrix} k_x \\ k_y \end{pmatrix} = \begin{pmatrix} \cos(\beta) & \sin(\beta) \\ -\sin(\beta) & \cos(\beta) \end{pmatrix} \begin{pmatrix} k_{x'} \\ k_{y'} \end{pmatrix}. \tag{3.9}$$

The differential operators transform in the opposite manner with respect to $\mathbf{r}$ in consistence to $k_i \cdot r_j = 2\pi\delta_{ij}$. We can write down the transformation for the operators appearing inside the $\mathbf{k} \cdot \mathbf{p}$ equation:

$$\begin{aligned} k_y - ik_x &= e^{-i\beta} \left(k_{y'} - ik_{x'}\right), \\ k_y + ik_x &= e^{i\beta} \left(k_{y'} + ik_{x'}\right). \end{aligned} \tag{3.10}$$

At this point, we may pass to consider the wavefunction. In the new reference frame, the wavefunction is given by:

$$\Psi'(\mathbf{k}, \mathbf{r}) = R(\beta)\Psi(\mathbf{k}, \mathbf{r}) = R(\beta) \sum_{\lambda=A}^{B} \sum_{\boldsymbol{\tau}=\mathbf{K}}^{\mathbf{K}'} F_{\tau\lambda}(\mathbf{k}, \mathbf{r})\Phi_\lambda(\boldsymbol{\tau}, \mathbf{r}), \tag{3.11}$$

where $R(\beta)$ is the general rotation operator. If $R(\beta)$ is applied to a function, it rotates all the quantities appearing inside the function. Thus, $R(\beta)$ acts both on the envelope functions and the Bloch states. Recalling the definition for the Bloch states $\Phi_\lambda(\boldsymbol{\tau}, \mathbf{r})$:

$$\Phi_\lambda(\boldsymbol{\tau}, \mathbf{r}) = e^{i\alpha_{\boldsymbol{\tau},\lambda}} \sum_{\mathbf{R}_\lambda} e^{i\boldsymbol{\tau}\cdot\mathbf{R}_\lambda} \phi_\pi(\mathbf{r} - \mathbf{R}), \tag{3.12}$$

with $\boldsymbol{\tau} = \mathbf{K}, \mathbf{K}'$ and $\lambda = A, B$. We can notice that $\Phi_\lambda(\boldsymbol{\tau}, \mathbf{r})$ is constant with respect to $R(\beta)$. Indeed, the π orbital is invariant under (x, y) rotations and the exponential depends on the scalar product that is invariant by definition. Thus:

$$\Phi'_\lambda(\boldsymbol{\tau}, \mathbf{r}) = R(\alpha)\Phi_\lambda(\boldsymbol{\tau}, \mathbf{r}) = \Phi_\lambda(\boldsymbol{\tau}, \mathbf{r}). \tag{3.13}$$

For what concerns the envelope functions, in general they may change but as they have not been explicitly defined yet, they can be simply renamed. Hence, we can conclude that overall a rotation affects only the operators in the $\mathbf{k} \cdot \mathbf{p}$ equation and

the coordinates of the vectors both in the direct and the reciprocal space.

We are now ready to begin the transformation procedure of the $k \cdot p$ Hamilltonian to pass in the nanotube reference frame. As first operation, we perform the rotation of $-\frac{\pi}{2}$. The correcting phase factors appearing on the differential operators $e^{i\beta}$ of Eq.(3.10) in this case amount to $\mp i$:

$$\gamma \begin{pmatrix} 0 & k_x - ik_y & 0 & 0 \\ k_x + ik_y & 0 & 0 & 0 \\ 0 & 0 & 0 & k_x + ik_y \\ 0 & 0 & k_x - ik_y & 0 \end{pmatrix} \begin{pmatrix} F_{\mathbf{K}A}(\mathbf{k},\mathbf{r}) \\ F_{\mathbf{K}B}(\mathbf{k},\mathbf{r}) \\ F_{\mathbf{K}'A}(\mathbf{k},\mathbf{r}) \\ F_{\mathbf{K}'B}(\mathbf{k},\mathbf{r}) \end{pmatrix} = E \begin{pmatrix} F_{\mathbf{K}A}(\mathbf{k},\mathbf{r}) \\ F_{\mathbf{K}B}(\mathbf{k},\mathbf{r}) \\ F_{\mathbf{K}'A}(\mathbf{k},\mathbf{r}) \\ F_{\mathbf{K}'B}(\mathbf{k},\mathbf{r}) \end{pmatrix} \quad (3.14)$$

In the new reference frame, the coordinates of the lattice vectors become:

$$\begin{aligned} \mathbf{a_1} &= \frac{a}{2} \begin{pmatrix} 1 \\ -\sqrt{3} \end{pmatrix}, \\ \mathbf{a_2} &= \frac{a}{2} \begin{pmatrix} 1 \\ \sqrt{3} \end{pmatrix}, \end{aligned} \quad (3.15)$$

The new positions of the atoms of the two sublattices are:

$$R_A(n_1, n_2) = a \left(\frac{1}{2}(-n_1 + n_2), \frac{1}{2\sqrt{3}} + \frac{\sqrt{3}}{2}(n_2 + n_1) \right), \quad (3.16)$$

$$R_B(n_1, n_2) = a \left(\frac{1}{2}(-n_1 + n_2), -\frac{1}{2\sqrt{3}} + \frac{\sqrt{3}}{2}(n_2 + n_1) \right). \quad (3.17)$$

The $\mathbf{K}$ points rotate as well:

$$\begin{aligned} \mathbf{K} &= \frac{2\pi}{a} \begin{pmatrix} \frac{1}{3} \\ -\frac{1}{\sqrt{3}} \end{pmatrix}, \\ \mathbf{K}' &= \frac{2\pi}{a} \begin{pmatrix} -\frac{1}{3} \\ -\frac{1}{\sqrt{3}} \end{pmatrix}, \end{aligned} \quad (3.18)$$

Remembering that each $\mathbf{K}$ point has two other equivalent points in the BZ, it is possible to change the couple of $\mathbf{K}$ points around which we make the expansion. In particular, here we decide to take a new couple of $\mathbf{K}$ points:

$$\begin{aligned} \mathbf{K_{new}} &= \frac{2\pi}{a} \begin{pmatrix} \frac{1}{3} \\ \frac{1}{\sqrt{3}} \end{pmatrix}, \\ \mathbf{K'_{new}} &= \frac{2\pi}{a} \begin{pmatrix} \frac{2}{3} \\ 0 \end{pmatrix}, \end{aligned} \quad (3.19)$$

Concerning the $\mathbf{k}\cdot\mathbf{p}$ Hamiltonian, the change of $\mathbf{K}$ point has no effects at all. However, we have to pay attention to the Bloch states. In order to be consistent, we need to replace the old $\mathbf{K}$ points with the new ones:

$$\begin{aligned}\mathbf{K_{old}} &= \mathbf{K_{new}} + \frac{2\pi}{a}\begin{pmatrix} 0 \\ -\frac{2}{\sqrt{3}} \end{pmatrix}, \\ \mathbf{K'_{old}} &= \mathbf{K'_{new}} + \frac{2\pi}{a}\begin{pmatrix} -1 \\ -\frac{1}{\sqrt{3}} \end{pmatrix},\end{aligned} \tag{3.20}$$

The updated form of the Bloch states is determined introducing the new $\mathbf{K}$ points inside Eq.(2.76). Changes in the phases occur. From now on, we discard the "new" label.

$$\begin{aligned}\Phi_A(\mathbf{K},\mathbf{r}) &= \frac{1}{\sqrt{N}}\sum_{\{\mathbf{R_A}\}} e^{i\mathbf{K}\cdot\mathbf{R_A}}\phi_\pi(\mathbf{r}-\mathbf{R_A}), \\ \Phi_B(\mathbf{K},\mathbf{r}) &= -\omega\frac{1}{\sqrt{N}}\sum_{\{\mathbf{R_B}\}} e^{i\mathbf{K}\cdot\mathbf{R_A}}\phi_\pi(\mathbf{r}-\mathbf{R_B}), \\ \Phi_A(\mathbf{K'},\mathbf{r}) &= -\omega\frac{1}{\sqrt{N}}\sum_{\{\mathbf{R_A}\}} e^{i\mathbf{K'}\cdot\mathbf{R_A}}\phi_\pi(\mathbf{r}-\mathbf{R_A}), \\ \Phi_B(\mathbf{K'},\mathbf{r}) &= -\omega\frac{1}{\sqrt{N}}\sum_{\{\mathbf{R_B}\}} e^{i\mathbf{K'}\cdot\mathbf{R_B}}\phi_\pi(\mathbf{r}-\mathbf{R_B}).\end{aligned} \tag{3.21}$$

We now perform the second transformation that is the translation. Specifically, we translate the origin of the direct space in order to let it coincide with an atom of the B sublattice.

$$\mathbf{r'} = \mathbf{r} + \boldsymbol{w} = \mathbf{r} + a\left(0, \frac{1}{2\sqrt{3}}\right) \tag{3.22}$$

The four Bloch states of Eq.(3.21) after the translation acquire an additional phase factor coming from the products of the $\mathbf{K}$ vectors with the translation vector $\boldsymbol{w}$. This factor is trivial in the $\mathbf{K'}$ valley.

$$\begin{aligned}\mathbf{K}\cdot\boldsymbol{w} &= e^{i\frac{\pi}{3}} \\ \mathbf{K'}\cdot\boldsymbol{w} &= 1.\end{aligned} \tag{3.23}$$

The $\mathbf{k}\cdot\mathbf{p}$ Hamiltonian is instead constant under the translation. The atomic posi-

tions must be updated once again though:

$$R_A(n_1, n_2) = a\left(\frac{1}{2}(n_1 + n_2), \frac{1}{\sqrt{3}} + \frac{\sqrt{3}}{2}(n_2 - n_1)\right) \tag{3.24}$$

$$R_B(n_1, n_2) = a\left(\frac{1}{2}(n_1 + n_2), \frac{\sqrt{3}}{2}(n_2 - n_1)\right) \tag{3.25}$$

We are now ready to perform the second rotation. The angle of rotation is the chiral angle θ. This rotations leads the x axis to lie along the direction of the chiral vector $\mathbf{C}$ and the y axis to lie along the nanotube axis parallel to $\mathbf{T}$. The $\mathbf{K}$ points after the rotation are:

$$\begin{aligned} \mathbf{K} &= \frac{2\pi}{a}\begin{pmatrix} \frac{1}{3}\cos(\theta) + \frac{1}{\sqrt{3}}\sin(\theta) \\ -\frac{1}{3}\sin(\theta) + \frac{1}{\sqrt{3}}\cos(\theta) \end{pmatrix}, \\ \mathbf{K}' &= \frac{2\pi}{a}\begin{pmatrix} \frac{2}{3}\cos(\theta) \\ -\frac{2}{3}\sin(\theta) \end{pmatrix}, \end{aligned} \tag{3.26}$$

The $\mathbf{k}\cdot\mathbf{p}$ equation becomes:

$$\gamma\begin{pmatrix} 0 & e^{-i\theta}(k_x - ik_y) & 0 & 0 \\ e^{i\theta}(k_x + ik_y) & 0 & 0 & 0 \\ 0 & 0 & 0 & e^{i\theta}(k_x + ik_y) \\ 0 & 0 & e^{-i\theta}(k_x - ik_y) & 0 \end{pmatrix}\begin{pmatrix} F_{\mathbf{K}A}(\mathbf{k},\mathbf{r}) \\ F_{\mathbf{K}B}(\mathbf{k},\mathbf{r}) \\ F_{\mathbf{K}'A}(\mathbf{k},\mathbf{r}) \\ F_{\mathbf{K}'B}(\mathbf{k},\mathbf{r}) \end{pmatrix} = E\begin{pmatrix} F_{\mathbf{K}A}(\mathbf{k},\mathbf{r}) \\ F_{\mathbf{K}B}(\mathbf{k},\mathbf{r}) \\ F_{\mathbf{K}'A}(\mathbf{k},\mathbf{r}) \\ F_{\mathbf{K}'B}(\mathbf{k},\mathbf{r}) \end{pmatrix} \tag{3.27}$$

We redefine the envelope function to avoid keeping explicit the phase factors in the $\mathbf{k}\cdot\mathbf{p}$ equation:

$$F_{\mathbf{K}B}(r) \to e^{i\theta}F_{\mathbf{K}B}(r), \tag{3.28}$$

$$F_{\mathbf{K}'A}(r) \to e^{i\theta}F_{\mathbf{K}'A}(r), \tag{3.29}$$

leading to:

$$\gamma\begin{pmatrix} 0 & k_x - ik_y & 0 & 0 \\ k_x + ik_y & 0 & 0 & 0 \\ 0 & 0 & 0 & k_x + ik_y \\ 0 & 0 & k_x - ik_y & 0 \end{pmatrix}\begin{pmatrix} F_{\mathbf{K}A}(\mathbf{k},\mathbf{r}) \\ F_{\mathbf{K}B}(\mathbf{k},\mathbf{r}) \\ F_{\mathbf{K}'A}(\mathbf{k},\mathbf{r}) \\ F_{\mathbf{K}'B}(\mathbf{k},\mathbf{r}) \end{pmatrix} = E\begin{pmatrix} F_{\mathbf{K}A}(\mathbf{k},\mathbf{r}) \\ F_{\mathbf{K}B}(\mathbf{k},\mathbf{r}) \\ F_{\mathbf{K}'A}(\mathbf{k},\mathbf{r}) \\ F_{\mathbf{K}'B}(\mathbf{k},\mathbf{r}) \end{pmatrix} \tag{3.30}$$

This is the equation we will use to determine the envelope functions of the carbon nanotubes. Before moving on, we need, however, to make a last adjustment. We look at the expression of the full wavefunction:

$$\begin{aligned} \Psi(\mathbf{k},\mathbf{r}) =& F_{\mathbf{K}A}(\mathbf{k},\mathbf{r})\Phi_A(\mathbf{K},\mathbf{r}) + e^{i\theta}F_{\mathbf{K}B}(\mathbf{k},\mathbf{r})\Phi_B(\mathbf{K},\mathbf{r}) \\ &+ e^{i\theta}F_{\mathbf{K}'A}(\mathbf{k},\mathbf{r})\Phi_A(\mathbf{K}',\mathbf{r}) + F_{\mathbf{K}'B}(\mathbf{k},\mathbf{r})\Phi_B(\mathbf{K}',\mathbf{r}'). \end{aligned} \tag{3.31}$$

The $e^{i\theta}$ phases can be absorbed inside the phase factors of the Bloch functions, as:

$$\begin{aligned}
\Phi_A(\mathbf{K},\mathbf{r}) &= \frac{1}{\sqrt{N}}\sum_{\{\mathbf{R_A}\}} e^{i\mathbf{K}\cdot\mathbf{R_A}}\phi_\pi(\mathbf{r}-\mathbf{R_A}),\\
\Phi_B(\mathbf{K},\mathbf{r}) &= -\omega\frac{1}{\sqrt{N}}e^{i\theta}\sum_{\{\mathbf{R_B}\}} e^{i\mathbf{K}\cdot\mathbf{R_A}}\phi_\pi(\mathbf{r}-\mathbf{R_B}),\\
\Phi_A(\mathbf{K}',\mathbf{r}) &= \frac{1}{\sqrt{N}}e^{i\theta}\sum_{\{\mathbf{R_A}\}} e^{i\mathbf{K}'\cdot\mathbf{R_A}}\phi_\pi(\mathbf{r}-\mathbf{R_A}),\\
\Phi_B(\mathbf{K}',\mathbf{r}) &= \frac{1}{\sqrt{N}}\sum_{\{\mathbf{R_B}\}} e^{i\mathbf{K}'\cdot\mathbf{R_B}}\phi_\pi(\mathbf{r}-\mathbf{R_B}).
\end{aligned} \tag{3.32}$$

In this manner, the full wavefunction can be written in its previous form:

$$\Psi(\mathbf{k},\mathbf{r}) = \sum_{\lambda=A}^{B}\sum_{\boldsymbol{\tau}=\mathbf{K}}^{\mathbf{K}'} F_{\boldsymbol{\tau}\lambda}(\mathbf{k},\mathbf{r})\Phi_\lambda(\boldsymbol{\tau},\mathbf{r}). \tag{3.33}$$

3.3 Envelope functions

In this section, we compute the envelope functions of graphene. The combination of the envelope functions with the Bloch states provides the single-particle wavefunctions in the region of the Dirac cones, where the envelope functions are slowly varying with respect to the lattice constant.

$$\gamma\begin{pmatrix} 0 & k_x-ik_y & 0 & 0\\ k_x+ik_y & 0 & 0 & 0\\ 0 & 0 & 0 & k_x+ik_y\\ 0 & 0 & k_x-ik_y & 0\end{pmatrix}\begin{pmatrix} F_{\mathbf{K}A}(\mathbf{k},\mathbf{r})\\ F_{\mathbf{K}B}(\mathbf{k},\mathbf{r})\\ F_{\mathbf{K}'A}(\mathbf{k},\mathbf{r})\\ F_{\mathbf{K}'B}(\mathbf{k},\mathbf{r})\end{pmatrix} = E\begin{pmatrix} F_{\mathbf{K}A}(\mathbf{k},\mathbf{r})\\ F_{\mathbf{K}B}(\mathbf{k},\mathbf{r})\\ F_{\mathbf{K}'A}(\mathbf{k},\mathbf{r})\\ F_{\mathbf{K}'B}(\mathbf{k},\mathbf{r})\end{pmatrix} \tag{3.34}$$

At a close inspection, we can notice that the upper and the lower branch of the Schrödinger equation are completely independent one to another. By introducing two spinors:

$$\begin{aligned}
F^{\mathbf{K}}(r) &= \begin{pmatrix} F_{\mathbf{K}A}(\mathbf{k},\mathbf{r})\\ F_{\mathbf{K}B}(\mathbf{k},\mathbf{r})\end{pmatrix},\\
F^{\mathbf{K}'}(r) &= \begin{pmatrix} F_{\mathbf{K}'A}(\mathbf{k},\mathbf{r})\\ F_{\mathbf{K}'B}(\mathbf{k},\mathbf{r})\end{pmatrix},
\end{aligned} \tag{3.35}$$

we can decouple the Schrödinger equation into two separate parts:

$$\begin{aligned}
\gamma\mathbf{k}\cdot\boldsymbol{\sigma}F_{\mathbf{K}}(\mathbf{r}) &= EF^{\mathbf{K}}(\mathbf{r}),\\
\gamma\mathbf{k}'\cdot\boldsymbol{\sigma}F_{\mathbf{K}'}(\mathbf{r}) &= EF^{\mathbf{K}'}(\mathbf{r}).
\end{aligned} \tag{3.36}$$

The quantities $\mathbf{k}$, $\mathbf{k}'$ are the momentum vectors and $\boldsymbol{\sigma}$ is the Pauli vector:

$$\boldsymbol{k} = k_x\hat{x} + k_y\hat{y} \tag{3.37}$$

$$\boldsymbol{k'} = k_x\hat{x} - k_y\hat{y} \tag{3.38}$$

$$\boldsymbol{\sigma} = \sigma_x\hat{x} + \sigma_y\hat{y} + \sigma_z\hat{z} \tag{3.39}$$

We can notice that Eq.(3.36) are analitically equivalent to the relativistic Dirac equations for massless fermions. For this reason, Eq.(3.36) are commonly called the Dirac equation of graphene. It follows that charge carriers of graphene will have transport properties similar to elementary massless spin ½ particles. Phenomena characteristic of relativistic quantum mechanics have indeed been observed, such as Klein's tunneling [57-61]. The eigenvalues of the relativistic Dirac equations are:

$$E_{\tau\alpha} = s_\alpha\gamma\sqrt{k_x^2 + k_y^2} = s_\alpha\gamma|\mathbf{k}|, \tag{3.40}$$

with $s_\alpha = \pm 1$, respectively, for the conduction and valence bands. We introduce the symbol τ that refers to the $\mathbf{K}$ or $\mathbf{K}'$ point. The energy is degenerate in the two valleys. The eigenfunctions of the relativistic Dirac equations, the envelope functions, have the aspect of spinors:

$$F_\alpha^\tau(r) = \begin{pmatrix} \frac{k_x + i\tau k_y}{\sqrt{k_x^2+k_y^2}} \\ s_\alpha \end{pmatrix} e^{i\mathbf{k}\cdot\mathbf{r}}, \tag{3.41}$$

here the symbol τ once again refers to the $\mathbf{K}$ or $\mathbf{K}'$ point and takes values ± 1 respectively.

3.4 From graphene to carbon nanotubes

In the previous section, we have derived the single-particle wavefunction and the energy dispersion of graphene. Taking advantage from the fact that nanotubes are just rolled up graphene sheets, we can derive the same quantities in carbon nanotubes. When moving to carbon nanotubes, the x-axis of the graphene sheet, once superimposed on the direction of the chiral vector, becomes the circumference of the tube and extends between 0 and $|\mathbf{C}|$. The single-particle wavefunction must adapt to the new topology of the system. Specifically, since a system with cylindrical symmetry is identical under translations of a whole circumference, we impose periodic boundary conditions on the wavefunction along the circumference direction:

$$\Psi(\mathbf{r}) = \Psi(\mathbf{r} + \mathbf{C}). \tag{3.42}$$

The single-particle wavefunction of graphene, defined in Eq.(3.33), is made up of a sum of products between the Bloch function and the envelope function. As the boundary condition $\Psi(\mathbf{r}) = \Psi(\mathbf{r} + \mathbf{C})$ has to hold in every point of the nanotube, each term of the sum must satisfy the equality. Thus, treating the $\mathbf{K}$ and $\mathbf{K}'$ point separately, we have:

$$\begin{aligned} \Phi_{\mathbf{K}\alpha}(\mathbf{r}+\mathbf{C})F_{\mathbf{K}\alpha}(\mathbf{r}+\mathbf{C}) &= \Phi_{\mathbf{K}\alpha}(\mathbf{r})F_{\mathbf{K}\alpha}(\mathbf{r}), \\ \Phi_{\mathbf{K}'\alpha}(\mathbf{r}+\mathbf{C})F_{\mathbf{K}'\alpha}(\mathbf{r}+\mathbf{C}) &= \Phi_{\mathbf{K}'\alpha}(\mathbf{r})F_{\mathbf{K}'\alpha}(\mathbf{r}), \end{aligned} \tag{3.43}$$

with $\alpha = A, B$. By making use of the definition of translation, we have:

$$\begin{aligned} e^{i\mathbf{K}\cdot\mathbf{C}}\Phi_{\mathbf{K}\alpha}(\mathbf{r})e^{i\mathbf{k}\cdot\mathbf{C}}F_{\mathbf{K}\alpha}(\mathbf{r}) &= \Phi_{\mathbf{K}\alpha}(\mathbf{r})F_{\mathbf{K}\alpha}(\mathbf{r}), \\ e^{i\mathbf{K}'\cdot\mathbf{C}}\Phi_{\mathbf{K}'\alpha}(\mathbf{r})e^{i\mathbf{k}'\cdot\mathbf{C}}F_{\mathbf{K}'\alpha}(\mathbf{r}) &= \Phi_{\mathbf{K}'\alpha}(\mathbf{r})F_{\mathbf{K}'\alpha}(\mathbf{r}). \end{aligned} \tag{3.44}$$

It follows that the product of the two translational phases must be equal to the unit:

$$\begin{aligned} e^{i\mathbf{K}\cdot\mathbf{C}}e^{i\mathbf{k}\cdot\mathbf{C}} &= 1 = e^{2\pi i n_C}, \\ e^{i\mathbf{K}'\cdot\mathbf{C}}e^{i\mathbf{k}'\cdot\mathbf{C}} &= 1 = e^{2\pi i n_C}, \end{aligned} \tag{3.45}$$

where n_C is a generic integer. We now compute all the translational phases, starting from the ones coming from the Bloch functions:

$$\begin{aligned} e^{i\mathbf{K}\cdot\mathbf{C}} &= e^{i\frac{2\pi}{3}(m-n)}, \\ e^{i\mathbf{K}'\cdot\mathbf{C}} &= e^{i\frac{2\pi}{3}(n+2m)}. \end{aligned} \tag{3.46}$$

We manipulate the phase factor of the term in $\mathbf{K}'$ to make it more similar to the other one:

$$e^{i\mathbf{K}'\cdot\mathbf{C}} = e^{i\frac{2\pi}{3}(2m+n)} = e^{i\frac{2\pi}{3}(n+2m)}e^{-2\pi i m} = e^{i\frac{2\pi}{3}(n-m)}. \tag{3.47}$$

Hence, both the phases depend on the difference $m - n$. We can write the difference $m - n$ as:

$$m - n = 3N + \nu, \tag{3.48}$$

with N being an integer and $\nu \in [-1, 0, 1]$. Effectively, the phase factors only depend on ν:

$$\begin{aligned} e^{i\mathbf{K}\cdot\mathbf{C}} &= e^{i\frac{2\pi}{3}\nu}, \\ e^{i\mathbf{K}'\cdot\mathbf{C}} &= e^{-i\frac{2\pi}{3}\nu}. \end{aligned} \tag{3.49}$$

The translational phases coming from the envelope functions are instead:

$$\begin{aligned} e^{i\mathbf{k}\cdot\mathbf{C}} &= e^{ik_x|C|}, \\ e^{i\mathbf{k}'\cdot\mathbf{C}} &= e^{ik'_x|C|}. \end{aligned} \tag{3.50}$$

where we have exploited that $\mathbf{C}$ lies along $\hat{x}$. The translational phases depend only on the transverse momentum. Putting everything together, we have:

$$\begin{aligned} e^{i\mathbf{K}\cdot\mathbf{C}}e^{i\mathbf{k}\cdot\mathbf{C}} &= e^{-i\frac{2\pi}{3}\nu}e^{ik_x|C|} = e^{2\pi i n_C}, \\ e^{i\mathbf{K}'\cdot\mathbf{C}}e^{i\mathbf{k}'\cdot\mathbf{C}} &= e^{i\frac{2\pi}{3}\nu}e^{ik'_x|C|} = e^{2\pi i n_C}. \end{aligned} \tag{3.51}$$

Simplifying, we find a condition on the transverse momenta:

$$\begin{aligned} k_x &= \frac{2\pi}{|C|}\left(n_C - \frac{\nu}{3}\right) = \frac{1}{R}\left(n_C - \frac{\nu}{3}\right), \\ k'_x &= \frac{2\pi}{|C|}\left(n_C + \frac{\nu}{3}\right) = \frac{1}{R}\left(n_C + \frac{\nu}{3}\right). \end{aligned} \tag{3.52}$$

We can sum up the two results in a unified expression, introducing the index τ that takes value 1 in the K valley and value -1 in the K' valley:

$$k_x(n_C, \tau) = \frac{1}{R}\left(n_C - \tau\frac{\nu}{3}\right), \quad \text{with} \quad n_c \in \mathbb{Z}. \tag{3.53}$$

So, the transverse momentum of the nanotube is quantized. The momentum along the axis k_y, however, remains continuous. Therefore, the carbon nanotube has a 1D Brillouin zone. If we plot the allowed wavevectors for a nanotube over the Brillouin zone of graphene, we will see a series of parallel lines (Fig 3.2 a-b). Each line creates an energy band of the carbon nanotube:

$$E_{\tau\alpha}(n_C, k) = s_\alpha\gamma\sqrt{k_y^2 + k_x^2(n_C, \tau)} = \gamma\sqrt{k_y^2 + \frac{1}{R^2}\left(n_C - \tau\frac{\nu}{3}\right)^2}. \tag{3.54}$$

Basically, the band dispersion of the nanotube is obtained by cutting the 2D band of graphene into many 1D bands at the different allowed values of the transverse momentum. Among all the bands, we now consider the two lowest lying in energy (Fig 3.2 c-d). These are the bands with $n_C = 0$ and their band dispersion is:

$$E_{\tau\alpha}(0, k) = s_\alpha\gamma\sqrt{k_y^2 + \left(\frac{\nu}{3R}\right)^2}. \tag{3.55}$$

Depending on the value of ν, there could be a finite gap at $k_y = 0$. We distinguish carbon nanotubes into two main groups: semiconducting nanotubes for which

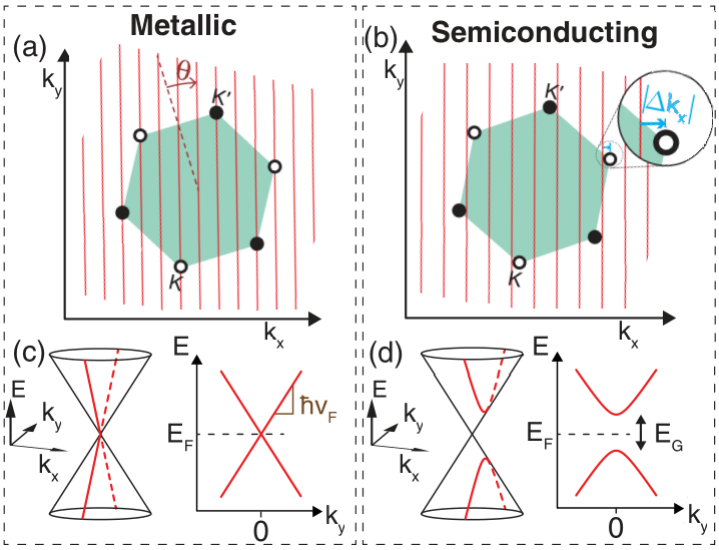

Figure 3.2: Quantization of the Brillouin zone of graphene as provided by the periodic boundary conditions. If the quantization lines intersect the Dirac points the nanotube is (a) metallic; otherwise (b) semiconducting. The offset between the quantization line $|\Delta k_x| = \frac{1}{3R}$ opens a band gap in the lowest-energy bands close to the Dirac points in semiconducting nanotubes (d) while the metallic character is preserved in the other tubes (c). (Figures are adapted from [4])

$\nu = \pm 1$ and nominally metallic nanotubes for which $\nu = 0$. The semiconducting nanotubes have a finite gap amounting to:

$$E_g = \gamma \Delta k_x = \frac{2\gamma}{3R}. \tag{3.56}$$

This gap is called in literature *primary gap* and it is quite large, in the order of $1eV$ for small tubes and decreases slowly with the radius.

In nominally metallic nanotubes, instead, the primary gap is null. As a consequence, the K points are included in the reduced Brillouin zone only of nominally metallic nanotubes and the low lying bands here feature Dirac cones in reciprocal space.

It is instructive to compute the density of states of carbon nanotubes to look at the available states. The density of states is defined as:

$$\rho(E) = \frac{2}{\Omega} Tr[\delta(E - \mathcal{H})], \tag{3.57}$$

where the factor 2 accounts for the spin and Ω is the surface of the nanotube. We

expand the trace within the basis of the envelope function:

$$\begin{aligned}\rho(E) &= \frac{2}{\Omega}\sum_{n_C}\sum_{\tau}\sum_{s_\alpha}\int dk\ \delta(E - E_{\tau\alpha}),\\ &= \frac{2}{\pi\gamma}\sum_{n_C}\sum_{\tau}\sum_{s_\alpha}\frac{E}{\sqrt{E^2 - \gamma^2 k_x^2(n_C,\tau)}}.\end{aligned} \tag{3.58}$$

The density of states shows Van Hove singularities in correspondence of $E = \gamma|k_x(n_C,\tau)|$, that are the energies associated to the quantized momenta (Fig. 3.3). So, a Van Hove singularity appears whenever a new band of the carbon nanotube becomes energetically available. We can focus on the density of states at $E = 0$. In semiconducting tubes, the density of states is null being gapped systems. Instead, in nominally metallic tubes, the density of states at the Fermi energy is a constant and can be expressed analytically [130]:

$$\rho(E_F) = \sum_{\tau}\sum_{s_\alpha}\frac{2}{\pi\gamma} = \frac{4}{\pi\gamma}, \tag{3.59}$$

where the factor 4 is due to the spin and the valley degeneracy. The value of the density at the Fermi energy differs greatly with flat graphene where the density of states vanishes.

3.5 Aharonov–Bohm effect

The most common method to manipulate the gap of carbon nanotubes is through an uniform external magnetic field along the axial direction $\mathbf{B} = B\hat{y}$. Such a

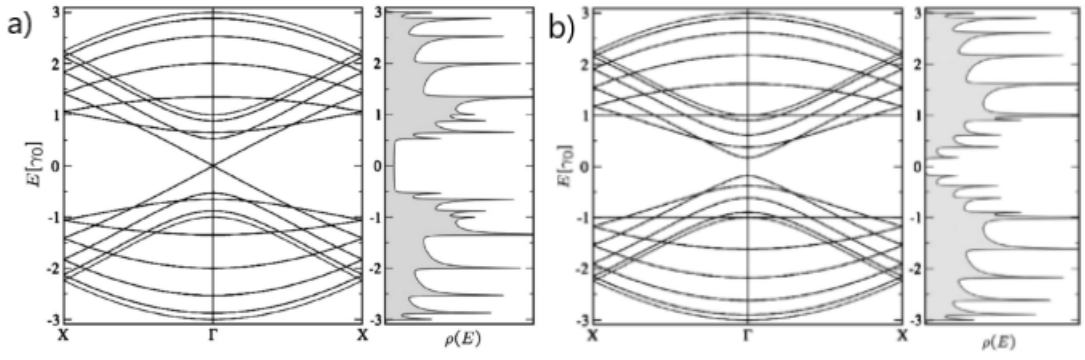

Figure 3.3: Band structure and density of states of a metallic (a) and semiconducting (b) nanotube within the zone-folding model. The Fermi level is located at zero energy. (Figures are taken from [2])

field leads to an Aharonov–Bohm effect [131, 132] for the presence of a vector potential $\mathbf{A}$, related to $\mathbf{B}$ as $\mathbf{B} = \nabla \times \mathbf{A}$. The wavevector of the electrons when a field is present is modified to:

$$\mathbf{k} \to \mathbf{k} - \frac{e}{c\hbar}\mathbf{A}. \tag{3.60}$$

The presence of the field affects the boundary conditions. We repeat the computations of $\Psi_{\tau\alpha}(\mathbf{r}+\mathbf{C},\mathbf{k})$ and impose once again the equality with of $\Psi_{\tau\alpha}(\mathbf{r},\mathbf{k})$.

$$\Phi_{\tau\alpha}(\mathbf{r}+\mathbf{C},\mathbf{k})F_{\tau\alpha}(\mathbf{r}+\mathbf{C},\mathbf{k}) = e^{2\pi i\phi_R}e^{i\tau\frac{2\pi}{3}\nu}\Phi_{\tau\alpha}(\mathbf{r},\mathbf{k})F_{\tau\alpha}(\mathbf{r},\mathbf{k}), \tag{3.61}$$

where the indices τ and α refer to the Dirac valley and the sublattice. The phase ϕ_R is:

$$\phi_R = \oint_{\mathbf{r}}^{\mathbf{r}+\mathbf{C}} (\mathbf{k} - \frac{e}{c\hbar}\mathbf{A}(\mathbf{r}')) \cdot d\mathbf{r}' = k_x|\mathbf{C}| - \frac{2\pi}{\Phi_0}\oint_{\mathbf{r}}^{\mathbf{r}+\mathbf{C}} \mathbf{A}(\mathbf{r}') \cdot d\mathbf{r}', \tag{3.62}$$

where we have introduced $\Phi_0 = ch/e$, the quantum of magnetic flux. By Stokes theorem, the contour integral in Eq.(3.62) can be turned into a magnetic flux:

$$\phi_R = k_x|\mathbf{C}| - \frac{2\pi}{\Phi_0}\int_\Omega BdS = k_x|\mathbf{C}| - \frac{2\pi\Phi(B)}{\Phi_0}. \tag{3.63}$$

Then, going back to Eq.(3.61), we can replace ϕ_R with its extend expression:

$$\Phi_{\tau\alpha}(\mathbf{r}+\mathbf{C},\mathbf{k})F_{\tau\alpha}(\mathbf{r}+\mathbf{C},\mathbf{k}) = e^{i\left(k_x|\mathbf{C}| - \frac{2\pi\Phi(B)}{\Phi_0}\right)}e^{i\tau\frac{2\pi}{3}\nu}\Phi_{\tau\alpha}(\mathbf{r},\mathbf{k})F_{\tau\alpha}(\mathbf{r},\mathbf{k}). \tag{3.64}$$

By applying the boundary conditions, we end up with the quantized momenta acquiring a dependence on the magnetic flux:

$$k_x(n_C,\tau) = \frac{1}{R}\left(n_C + \frac{\Phi(B)}{\Phi_0} - \tau\frac{\nu}{3}\right). \tag{3.65}$$

Thus, by modifying the magnetic flux, it is possible to control the gap. The gap shows large oscillation of period Φ_0 between 0 and γ/R. This giant Aharonov–Bohm effect on the band gap is a special feature of carbon nanotubes [132, 133, 134, 135].

3.6 Curvature gap

Up to now, we have treated the electronic properties of carbon nanotubes just accounting the confinement of the electrons around the tube circumference. However, in this manner, we are neglecting the fact that carbon nanotubes are real 3D

cylinders. The topology of the system is different from flat graphene as the carbon atoms lie over a cylindrical surface. The carbon-carbon bonds between the atoms on the nanotube surface are affected by the curved topology of the nanotube and get slightly distorted with respect to flat graphene. However, the distortion of the carbon-carbon bonds is not observed when the atomic bond is parallel to the nanotube axis. As a consequence, the lattice vector along the axis and along the tube circumference have slightly different lengths. In addition, the π orbitals of neighbouring carbon atoms are generally not parallel on a curved surface, yielding to differences in the hopping terms used in the tight-binding calculations. From an electronic point of view, all these effects lead to a shift of the Fermi wavevector k_F away from the Brillouin zone corners of the graphene sheet [136, 137] (Fig.3.4 a). In armchair nanotubes, the shift of k_F occurs in the direction parallel to the nanotube axis along the line of momenta with $n_C = 0$, consequently the metallic character is preserved. However, in non-armchair nominally metallic nanotubes, the shift of k_F is not along the axial direction and there is a finite shift Δk_x along the quantized direction. The shift Δk_x is opposite in the two Dirac valleys (Fig.3.4 b):

$$\Delta k_x = \tau \frac{a^2}{16R^2} \cos(3\theta) = \tau k_c \tag{3.66}$$

The total value of the quantized component of the momenta then needs to include this further contribution:

$$k_x(n_C, \tau) = \frac{1}{R}\left(n_C + \frac{\Phi(B)}{\Phi_0} + \tau k_c - \frac{\nu}{3}\right) \tag{3.67}$$

In non-armchair nominally metallic nanotubes, then, the lowest energy band $n_C = 0$ no longer passes through k_F and a small band gap amounting to $2\gamma\Delta k_x$ is present. In literature, this gap is often called the secondary gap or curvature gap. The typical magnitude of the secondary gap are tens of meV [136, 138]. Truncated Dirac cones appear in the low energy bands $n_C = 0$. The curvature gap depends on the radius and the chiral angle of the nanotube through:

$$E_g = \frac{\gamma a^2}{8R^2} \cos(3\theta) \tag{3.68}$$

The method illustrated so far to include curvature effects, however, shows problems when dealing with tubes with very small radii. To understand why, we have to look back at the electronic orbitals of the carbon atoms. In a nanotube, the planar sp^2 orbital and the p_z orbitals are not orthogonal and can superimpose. This leads the electronic state of the carbon atoms into hybrid orbitals that exhibit a partial sp^2 and partial sp^3 character. The amount of hybridisation ultimately

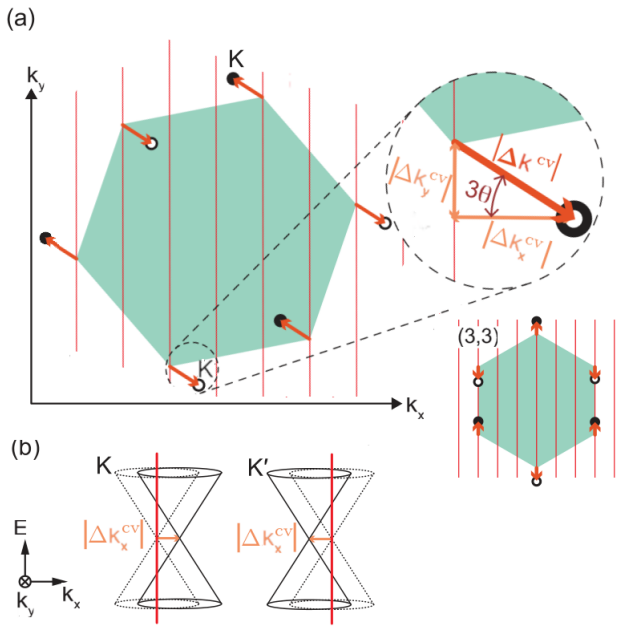

Figure 3.4: Changes to the nanotubes band structure induced by the curvature. In figure (a) we illustrate the direction along which the Dirac points are displaced away from the corners of the Brillouin zone in generic a chiral nanotube. The magnitude of the shift is increased by a factor of 15 to help the reading. Only the displacement vector Δk_x causes a gap opening (b) and Δk_x is opposite in the two K valleys. Armchair carbon nanotubes conserve the Dirac points within their Brillouin zone. (Figures adapted from [4])

depends on the radius, limiting the relevance of this re-hybridisation only to the smallest tubes. The creation of hybrid orbitals is not taken into account in the zone-folding model of graphene, as it is expected that the π orbitals do not mix with the σ states since they have a different parity with respect to planar reflection. Thus, the zone-folding picture fails to capture the true behaviour of the system in small tubes where the re-hybridisation cannot be reduced to a perturbation [139, 140, 141]. These nanotubes have to be treated independently, typically recurring to first principle calculations. A special exception is represented by armchair nanotubes. Even at small radii, the hybridization has almost no effect on the band dispersion of armchair tubes except for causing a strong shift of the k_F point along the line $n_C = 0$. Thus, armchair tubes can always be described within the zone-folding picture.

3.7 Spin-orbit interaction

A last effect that may be accounted is the spin-orbit interaction. The spin-orbit coupling in carbon materials is generally weak as carbon has a low atomic number

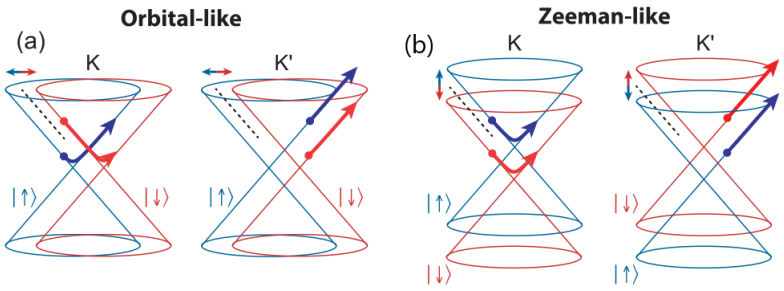

Figure 3.5: The two types of spin-orbit coupling. (a) The orbital-like coupling is equivalent to a spin-dependent magnetic field coupling to μ_{orb}. (b) The Zeeman-like coupling leads to a spin-dependent vertical shift of the band structure, equivalent to a Zeeman splitting that is opposite in the two valleys. (Figures taken from [4])

(Z=6). An example of this is flat graphene, where the spin splitting is only of the order of few μeV [142, 143]. In carbon nanotubes, however, the curved topology of the system enhances the spin-orbit coupling compared to flat graphene [144, 145, 146]. It has been estimated that the spin-orbit splitting is typically in the order of tenth of meV and is made up of two different contributions (Fig 3.5): an orbital type coupling, that shifts the quantization lines k_x, and a Zeeman type, which causes a spin-dependent shift of the energies. In the envelope functions formalism, the combined Hamiltonian of the two spin-orbit interactions is:

$$H_{SO} = \alpha S_z \sigma_x + \tau_z \beta \cos(3\theta) S_z, \tag{3.69}$$

where S_z is a Pauli matrix in the spin basis. The first term is the orbital-type coupling, while the second is the Zeeman-type coupling. The Zeeman-type of spin-orbit interaction depends on the chirality of the tube, being maximum at a zigzag wrapping and null in armchairs.

The estimated values of the parameters α and β vary a lot in literature. Partly due to the fact that they are very small, at the very limit of the experimental accuracy. In addition, the measurement of β is very challenging. For example, techniques based on observing changes in the quantized momenta due to the spin flavour that are used to determine α do not work for β. The only method currently available is analysing the spin flavour of the transport gap. However, this is not an optimal choice as other more pronounced effects add up on the transport gap preventing a clear measurement of β.

3.8 Two band model of narrow-gap carbon nanotubes

In the next chapters, we are going to restrict our interest to nanotubes with null primary gap, also known as narrow-gap carbon nanotubes. As discussed in the

introduction, the main motivation of this work is studying excitonic effects in carbon nanotubes especially for what concerns a possible formation of an excitonic insulator. The presence of large gaps between the valence and conduction bands of tubes with primary gaps hinders the realisation of an excitonic insulator in these systems; allowing to reduce the search only in narrow-gap nanotubes. To fully describe the electronic properties of of narrow-gap tubes, it is sufficient to include the valence and conduction bands closest to the gap. In this short section, we make a final recap of the main electronic properties of narrow-gap carbon nanotubes in the two band model without including spin-orbit interaction. The Hamiltonian is:

$$[\gamma k_\tau \sigma_x + \gamma \tau k \sigma_y] F_\alpha^\tau(\mathbf{r}) = E_{\tau\alpha} F^\tau(\mathbf{r}) \tag{3.70}$$

where σ_x and σ_y are Pauli matrices, the symbol τ refers to the $\mathbf{K}$ or $\mathbf{K}'$ point and takes values ± 1 respectively. The momentum is split into a continuous component along the nanotube axis, from now on indicated as k, and a quantized momentum k_τ equal to:

$$k_\tau = \frac{1}{R}\left(\frac{\Phi(B)}{\Phi_0} + \tau k_c\right) \tag{3.71}$$

The envelope functions are two dimensional spinors:

$$F_\alpha^\tau(r) = \begin{pmatrix} \frac{k_\tau + i\tau k_y}{\sqrt{k_\tau^2 + k_y^2}} \\ s_\alpha \end{pmatrix} e^{ik_\tau x} e^{iky}, \tag{3.72}$$

being x along the tube circumference and y along the nanotube axis. The energies of the electronic states are:

$$E_{\tau\alpha} = s_\alpha \gamma \sqrt{k_\tau^2 + k_y^2}, \tag{3.73}$$

with $s_\alpha = \pm 1$, respectively, for the conduction and valence bands.

Chapter 4

Anomalous screening in narrow-gap carbon nanotubes

In this chapter, we carry out the study of screening properties of narrow-gap carbon nanotubes. The study is based on selected first principles calculations generalised at model level for tubes of any size and chirality.

The contents of the current chapter and of its appendix (appendix A) are a paper just submitted to Physical Review B. With respect to the paper under revision, here the layout is modified to adapt it to the style of the thesis work.

4.1 Calculations from first principles

Calculations from first principles proved to be very reliable to study electronic properties of physical systems [147, 148]. In this work, we use ab-initio results as a benchmark to investigate screening properties of selected carbon NTs. The systems considered are the (3,3) and (5,5) armchair NTs as well as the (9,0) and the (12,0) zigzag NTs. Our calculations from first principles are performed in two steps. In first instance, we perform density functional theory (DFT) computations of the NTs. On top of the DFT computation, we then compute the dielectric function and the screened potential. The real-space screened potential is reconstructed by performing an expansion over the reciprocal lattice basis:

$$W(\boldsymbol{r},\boldsymbol{r'}) = \sum_{\boldsymbol{q}}\sum_{\boldsymbol{G}}\sum_{\boldsymbol{G'}} e^{i(\boldsymbol{G}+\boldsymbol{q})\cdot\boldsymbol{r}} e^{-i(\boldsymbol{G'}+\boldsymbol{q})\cdot\boldsymbol{r'}} \epsilon^{-1}_{\boldsymbol{G},\boldsymbol{G'}}(\boldsymbol{q},0) v(\boldsymbol{q}+\boldsymbol{G'}), \qquad (4.1)$$

where $\epsilon^{-1}_{\boldsymbol{G},\boldsymbol{G'}}(\boldsymbol{q},\omega)$ is the momentum- and frequency-dependent inverse dielectric matrix, $v(\boldsymbol{q}) = 4\pi e^2 \Omega^{-1}/q^2$ is the bare Coulomb potential, $\boldsymbol{G}$ is the reciprocal lattice vector, and Ω is the system volume. We treat the screening within the

random phase approximation (RPA):

$$\epsilon^{-1}_{\boldsymbol{G},\boldsymbol{G'}}(\boldsymbol{q},\omega) = \left[\delta_{\boldsymbol{G},\boldsymbol{G'}} - \Pi_{\boldsymbol{G},\boldsymbol{G'}}(\boldsymbol{q},\omega)v(\boldsymbol{q}+\boldsymbol{G})\right]^{-1}, \tag{4.2}$$

with $\Pi_{\boldsymbol{G},\boldsymbol{G'}}(\boldsymbol{q},\omega)$ being the irreducible polarisation:

$$\Pi_{\boldsymbol{G},\boldsymbol{G'}}(\boldsymbol{q},\omega) = 2\sum_{n,n'}\sum_{\boldsymbol{k}} \frac{f(E_{n,\boldsymbol{k}}) - f(E_{n',\boldsymbol{k}+\boldsymbol{q}})}{\omega + E_{n,\boldsymbol{k}} - E_{n',\boldsymbol{k}+\boldsymbol{q}} + i\eta}\rho^{*}_{n,n'}(\boldsymbol{k},\boldsymbol{q},\boldsymbol{G'})\rho_{n,n'}(\boldsymbol{k},\boldsymbol{q},\boldsymbol{G}). \tag{4.3}$$

The $f(E)$ are the occupation factors, the overlap integrals are defined as $\rho_{n,n'}(\boldsymbol{k},\boldsymbol{q},\boldsymbol{G}) = \langle n\boldsymbol{k}|e^{i(\boldsymbol{G}+\boldsymbol{q})\cdot\boldsymbol{r}}|n'\boldsymbol{k}+\boldsymbol{q}\rangle$, and η is a positive infinitesimal. The indexes n, n' run over the electronic bands. The energies, $E_{n,\boldsymbol{k}}$, and wavefunctions, $|n\boldsymbol{k}\rangle$, we employ in Eq. (4.3) are those determined by the DFT computations. As we mainly look at the long-range potential of carbon NTs, only the static polarisation $\Pi_{\boldsymbol{G},\boldsymbol{G'}}(\boldsymbol{q},0)$ is necessary in our work.
Density functional theory calculations were performed using the QUANTUM ESPRESSO package [149, 150], where wave functions are expanded in plane waves and pseudopotentials are used to account for the electron-ion interaction. We used the local density approximation (LDA) for the exchange-correlation potential, according to the Perdew-Zunger parametrization [151], and norm conserving pseudopotentials. The kinetic energy cutoff to represent the Kohn-Sham wavefunction was set to 70 Ry and an amount of vacuum of 38 Bohr in the direction perpendicular to the nanotube axis was considered to avoid replica interactions. The screened potential and the dielectric function were calculated using the Yambo code [152, 153], where we considered 80, 120, 300, and 600 bands in the summation of Eq.4.3 for the (3,3), (5,5), (9,0), and (12,0) NTs, respectively. A cutoff of 4 Ry in the $\epsilon^{-1}_{G,G'}$ matrix dimension was considered for all NTs. The Brillouin zone was sampled using a one dimensional grid of respectively 1973 and 205 k-points for armchair and zigzag NTs.

4.2 Effective-mass theory

4.2.1 Envelope function

Within the effective mass (EM) and envelope function approximations, a single-wall carbon NT is treated as a rolled graphene sheet [132, 5, 1, 2], as illustrated in Fig. 4.1. In the limit of large radius, the Bloch states, $\psi_\tau(\boldsymbol{r})$, that multiply the envelopes coincide with the π tight-binding states of graphene located at $\tau = \mathrm{K,K'}$ corners of the hexagonal Brillouin zone, the charge neutrality points where Dirac

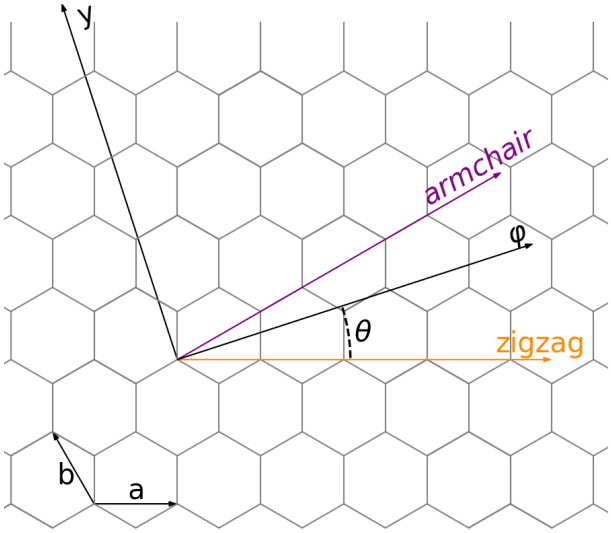

Figure 4.1: Pictorial illustration of the folding of a graphene sheet. Here φ and y are, respectively, the direction of folding and of the nanotube axis, whereas a and b are the basis vectors of the graphene lattice. The chiral angle θ spans the region between φ and a.

cones touch. For each valley τ, the NT orbital wave functions are

$$\Psi_{\alpha\tau k}(\boldsymbol{r}) = F^{\tau A}_{\alpha k}(\boldsymbol{r})\,\psi_{\tau A}(\boldsymbol{r}) + F^{\tau B}_{\alpha k}(\boldsymbol{r})\,\psi_{\tau B}(\boldsymbol{r}), \tag{4.4}$$

where A and B label the two inequivalent sublattices spanning the graphene honeycomb lattice. The envelope function sublattice components, $F^{\tau A}(\boldsymbol{r})$ and $F^{\tau B}(\boldsymbol{r})$, are just plane waves, provided the projection of the wave vector onto the direction perpendicular to the NT axis, φ, is properly quantized (Fig. 4.1). This procedure, which corresponds to extract from the two-dimensional bands of graphene many one-dimensional sub-bands α, leads to a graphene-like Dirac equation for the two-component envelope vector, $\boldsymbol{F}^{\tau}_{\alpha k}$,

$$\begin{pmatrix} 0 & \gamma k_\tau - i\tau\gamma k \\ \gamma k_\tau + i\tau\gamma k & 0 \end{pmatrix} \boldsymbol{F}^{\tau}_{\alpha k} = E_{\alpha\tau}(k)\,\boldsymbol{F}^{\tau}_{\alpha k}, \tag{4.5}$$

where k_τ is the quantized, transverse wave vector component, k is the wave vector along the NT axis, and $\tau = 1$ for K, $\tau = -1$ for K$'$ valleys. As we are interested in the long-range screening properties of narrow-gap NTs, out of all sub-bands α we consider only the top valence ($\alpha = c$) and bottom conduction ($\alpha = v$) bands closest to Dirac apexes. As shown below, this choice is validated a posteriori by comparing the dielectric function obtained from first principles with that obtained within the EM approximation as well as within the model of Sec. 4.3. The dispersion of bands c and v is Dirac-like:

$$E_{\alpha\tau}(k) = s_\alpha \gamma \sqrt{k_\tau^2 + k^2}. \tag{4.6}$$

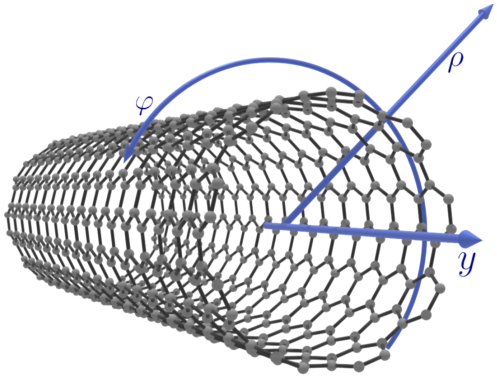

Figure 4.2: Pictorial representation of a nanotube with an armchair chirality. Here y, φ, and ρ are the directions of the nanotube axis, the direction on the circumference along which the folding has been performed, and the radial direction, respectively. The tube surface has radial coordinate $\rho = R$.

Here γ is graphene band parameter, $s_\alpha = 1$ and $s_\alpha = -1$ for c and v bands, respectively.

The solution of Dirac equation (4.5) provides the phase relation between the two plane wave components of the envelope:

$$\boldsymbol{F}^{\tau}_{\alpha k}(\boldsymbol{r}) = \begin{pmatrix} F^{A}_{\tau\alpha k} \\ F^{B}_{\tau\alpha k} \end{pmatrix} e^{i\boldsymbol{k}\cdot\boldsymbol{r}} = \frac{1}{\sqrt{2}} \begin{pmatrix} \frac{k_\tau - i\tau k}{\sqrt{k_\tau^2 + k^2}} \\ s_\alpha \end{pmatrix} e^{iky} e^{ik_\tau R\varphi}, \tag{4.7}$$

where R is the NT radius, φ the azimuthal angle, and y is the coordinate parallel to the NT axis, as shown in Fig. 4.2.

The gap $2\gamma k_\tau$ we consider here is narrow [154, 2], usually ranging between 0 and 100 meV and hence smaller than the typical value characteristic of semiconducting NTs, of the order of 1 eV. This narrow gap originates from the curvature of the nanotube [154] and may be tuned by an axial magnetic field through the Aharonov-Bohm effect [132], the two contributions to the gap adding in one valley and cancelling out in the other one. At zero field, the quantized wave vector k_τ is estimated as [154, 2]

$$k_\tau = \tau \frac{0.625 \text{ eV}}{\gamma R^2} \cos(3\theta), \tag{4.8}$$

with $\gamma = 6.58$ eV Å. Here θ is the chiral angle identifying the direction along which the graphene is rolled, the zigzag and armchair orientations corresponding to $\theta = 0$ and $\theta = \pi/6$, respectively (see Fig. 4.1).

4.2.2 Dielectric function

The EM dielectric function is built starting from the form that Coulomb interaction takes on a cylindrical surface[5]:

$$V_{cyl}(\boldsymbol{r}, \boldsymbol{r'}) = \frac{e^2}{\sqrt{4R^2 \sin^2\left(\frac{\varphi-\varphi'}{2}\right) + (y-y')^2}}. \tag{4.9}$$

This potential may be expanded over azimuthal quantum number, m, and axial wave vector, q, components as

$$V_{\text{cyl}}(\boldsymbol{r}, \boldsymbol{r'}) = \frac{2e^2}{A} \sum_q \sum_{m=-\infty}^{\infty} I_{|m|}(qR)\, K_{|m|}(qR) e^{im(\varphi-\varphi')}\, e^{iq(y-y')}. \tag{4.10}$$

Here A is the nanotube length, while $I_m(x)$ and $K_m(x)$ are the modified Bessel functions of first and second kind, respectively. The RPA dielectric function, whose generic expression is given by Eq. (4.2), may then be recasted in terms of angular momenta m rather than $\boldsymbol{G}$ vectors:

$$\epsilon_{\text{EM}}(m, q) = 1 - \frac{2e^2}{A} I_{|m|}(qR)\, K_{|m|}(qR) \Pi_{\text{EM}}(m, q). \tag{4.11}$$

The polarisation Π_{EM}, which provides the independent-particle response, is written in terms of the wave functions (4.4):

$$\begin{aligned}\Pi_{\text{EM}}(m, q) = 2 \sum_{\alpha,\alpha'} \sum_{\tau,\tau'} \sum_{k \in BZ} &\langle \alpha\tau k | e^{-iqy} e^{-im\varphi} | \alpha'\tau' k+q \rangle \langle \alpha'\tau' k+q | e^{iqy'} e^{im\varphi'} | \alpha\tau k \rangle \\ \times \quad &\frac{f(E_{\alpha'\tau'}(k+q)) - f(E_{\alpha\tau}(k))}{E_{\alpha'\tau'}(k+q) - E_{\alpha\tau}(k)},\end{aligned} \tag{4.12}$$

where the ket $|\alpha\tau k\rangle$ is the NT orbital state $\Psi_{\alpha\tau k}$ in Dirac notation.[5]

A few simplifications are now in order. At zero temperature the difference between the Fermi-Dirac factors, $f(E)$, selects virtual electron-hole excitations from filled valence to empty conduction band states only, hence the only relevant overlap integrals are $(\alpha = c, \alpha' = v)$ and $(\alpha = v, \alpha' = c)$. We ignore intervalley scatterings terms ($\tau \neq \tau'$), as they require large momentum transfer and are therefore negligible within the EM approximation. Whereas in principle the sum over k extends through the whole Brillouin zone, we truncate it through a cut-off k_o, as done in Ref. [5]. We choose the cut-off to include only those k-points providing the bands with a Dirac-like shape, consistently with the previous work [28].

Eventually, by converting the sum over k into an integral, one obtains

$$\epsilon_{\text{EM}}(m,q) = 1 - \frac{4e^2}{\pi} I_{|m|}(qR)\, K_{|m|}(qR) \sum_{\alpha,\alpha'} \sum_{\tau} \int_{-k_o}^{k_o} dk \langle \alpha\tau k | e^{-iqy} e^{-im\varphi} | \alpha'\tau k{+}q \rangle \\ \times \quad \langle \alpha'\tau k + q | e^{iqy'} e^{im\varphi'} | \alpha\tau k \rangle \frac{f(E_{\alpha' k+q}) - f(E_{\alpha k})}{E_{\alpha'\tau'}(k+q) - E_{\alpha\tau}(k)}. \quad (4.13)$$

Importantly, the overlap integrals have the same form as those of graphene, the curved topology of the nanotube entering only through the quantized wave vector k_τ:

$$\langle \alpha k | e^{-iqy} e^{-im\varphi} | \alpha' k{+}q \rangle = \frac{1}{2} \left(\frac{k(k+q) + k_\tau^2 - iqk_\tau}{\sqrt{k^2 + k_\tau^2}\sqrt{(k+q)^2 + k_\tau^2}} + (2\delta_{\alpha,\alpha'} - 1) \right) \delta_{m,0}. \quad (4.14)$$

Since only the $m = 0$ angular momentum component is relevant within the two-band approximation, the dielectric function reduces to

$$\epsilon_{\text{EM}}(q) = 1 + \frac{2e^2}{\pi\gamma} I_0(qR) K_0(qR) \sum_{\tau} \left[\frac{\sqrt{(k_o+q)^2 + k_\tau^2} - \sqrt{(k_o-q)^2 + k_\tau^2}}{q} \right. \\ + \quad \frac{2k_\tau^2}{q\sqrt{q^2 + 4k_\tau^2}} \log \left(\frac{\sqrt{q^2 + 4k_\tau^2}\sqrt{k_o^2 + k_\tau^2} + 2k_\tau^2 - k_o q}{\sqrt{q^2 + 4k_\tau^2}\sqrt{(k_o+q)^2 + k_\tau^2} + 2k_\tau^2 + q(k_o+q)} \right. \\ \left. \left. \times \quad \frac{\sqrt{q^2 + 4k_\tau^2}\sqrt{(k_o-q)^2 + k_\tau^2} + 2k_\tau^2 + q(q-k_o)}{\sqrt{q^2 + 4k_\tau^2}\sqrt{k_o^2 + k_\tau^2} + 2k_\tau^2 + k_o q} \right) \right], \quad (4.15)$$

which, in the limit of large cut-off k_o, simplifies to:

$$\epsilon_{\text{EM}}(q) = 1 + \frac{4e^2}{\pi\gamma} I_0(qR) K_0(qR) \sum_{\tau} \left[1 + \frac{2k_\tau^2}{q\sqrt{q^2 + 4k_\tau^2}} \log \left(\frac{\sqrt{q^2 + 4k_\tau^2} - q}{\sqrt{q^2 + 4k_\tau^2} + q} \right) \right]. \quad (4.16)$$

4.3 Model dielectric function

In this section we improve the EM dielectric function by fully taking into account the three-dimensional topology of Bloch states $\psi_{\tau A/B}(\boldsymbol{r})$ that occur in the expression (4.4) for NT wave functions, while keeping the envelopes F unchanged. The three-dimensional modelization of the Bloch states is illustrated in subsection 4.3.1. We introduce (subsection 4.3.2) a large cylindrical supercell that contains

the NT and then expand the states ψ over the vectors $\boldsymbol{G}$ of the supercell three-dimensional reciprocal lattice. Here we avoid spurious interactions among supercell replicas by using the exact Coulomb cutoff technique of Refs. [118, 155]. The expressions for the dielectric function and dressed Coulomb interaction we obtain in subsection 4.3.3 exhibit an explicit dependence on reciprocal lattice vectors perpendicular to the NT axis, which accounts for the effect of tube curvature on wave functions.

4.3.1 Three-dimensional Bloch states

The $\psi_{\tau A/B}(\boldsymbol{r})$ tight-binding Bloch states of Eq. (6.1) are localised on the atomic sites of the curved NT surface, whereas the EM model treats the lattice as two-dimensional. The position of these atoms depends in turn on the NT chirality, which may lead to a complex structure. For the sake of simplicity, we consider the exact atom location in two exemplar cases only, i.e., armchair and zigzag NTs, which are detailed, respectively, in Appendixes A.2 and A.3. Importantly, the forms of dielectric function and screened Coulomb potential that we obtain turn out to be identical to those derived from a simpler structural three-dimensional model [114] that applies to all NT chiralities. Therefore, in this section we present only the model, which is validated in subsection 4.8 through comparison with the results for the true lattice.

The model treats the NT structure as a series of N rings over which the charge is spread homogeneously. As illustrated in Fig. 4.3, the rings are perpendicular to the NT axis and their radius is equal to the tube radius, R. There are two species of rings, one for each sublattice. The ring positions along the y axis, $\boldsymbol{R}_l^A = R_l^A \hat{y}$ or $\boldsymbol{R}_l^B = R_l^B \hat{y}$, are given by:

$$\begin{cases} R_l^A = \lambda l + y_0^A \\ R_l^B = \lambda l + y_0^B \end{cases} \quad \text{with} \quad l = 1, ..., N. \tag{4.17}$$

Here, $\lambda = a\cos(\pi/6 - \theta)$ is the supercell length and $a = 2.46$ Å is graphene lattice constant. The rings are localised and equally spaced along the NT axis, hence their y coordinate may be thought of as an average over the positions of all atoms within a stripe of width λ (shadowed area in Fig. 4.3). Therefore, as the simplest possible approximation, we take the ring location at the origin to be the same for the two sublattices, i.e., $y_0^A = y_0^B = 0$. The corresponding Bloch states

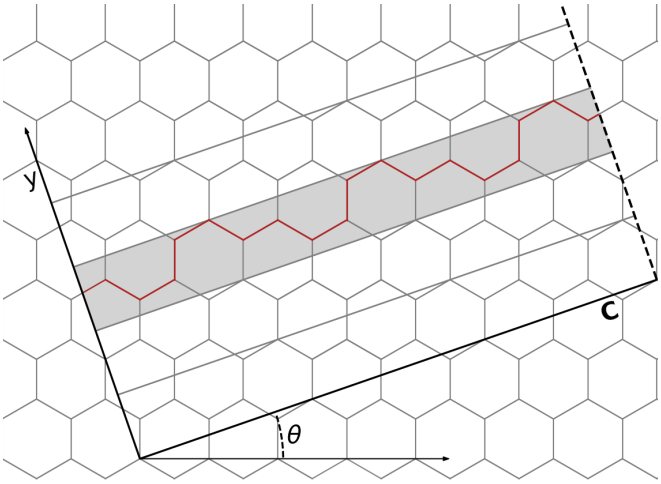

Figure 4.3: Pictorial illustration of the method used to build the homogeneous charge rings. $\boldsymbol{C}$ and y are, respectively, the chiral vector and the nanotube axis. The dashed line on the right hand side signals where the cut of the graphene sheet is performed. We divide the nanotube surface into equally spaced stripes. Each stripe contains a unique closed chain of atoms (indicated in red in the highlighted stripe). The chains of atoms are replaced with two homogeneous charge rings, one for each sublattice. The rings are placed at the centre of the stripe.

are:

$$\psi_{\tau A}(\boldsymbol{r}) = \frac{1}{\sqrt{2N}} \frac{e^{i\phi_{\tau A}}}{\sqrt{2\pi R}} \sum_{l=1}^{N} \left[e^{i\boldsymbol{K_\tau}\cdot\boldsymbol{R}_l^A} g(\boldsymbol{r} - \boldsymbol{R}_l^A) \right],$$
$$\psi_{\tau B}(\boldsymbol{r}) = \frac{1}{\sqrt{2N}} \frac{e^{i\phi_{\tau B}}}{\sqrt{2\pi R}} \sum_{l=1}^{N} \left[e^{i\boldsymbol{K_\tau}\cdot\boldsymbol{R}_l^B} g(\boldsymbol{r} - \boldsymbol{R}_l^B) \right], \tag{4.18}$$

where $\boldsymbol{K_\tau}$ is either K or K′, and $\phi_{KA} = 0$, $\phi_{K'A} = \theta$, $\phi_{KB} = -\frac{\pi}{3} + \theta$, $\phi_{K'B} = 0$ (see Ref. [129]). The g are functions localized on the tube surface, modeled as a homogeneous cylinder, whose square moduli behave as Dirac functions and which are defined as follows:

$$g^*(\boldsymbol{r} - \boldsymbol{R}_l^\eta)\, g(\boldsymbol{r} - \boldsymbol{R}_{l'}^{\eta'}) = \delta_{\eta,\eta'}\delta_{l,l'}\, \delta(\rho - R)\, \delta(y - R_l^\eta), \tag{4.19}$$

with ρ being the radial coordinate. As the states (4.18) are achiral, NT orbitals $\Psi_{\alpha\tau k}(\boldsymbol{r})$ depend on chirality solely through the curvature wave vector k_τ that enters the envelopes $\boldsymbol{F}^\tau_{\alpha k}$.

4.3.2 Supercell calculation

In this subsection we mimic the approach from first principles by building replicas of the tube along the directions perpendicular to the axis, as illustrated in Fig. 5.2.

As the whole system is now periodic, we may compute the polarisation $\Pi^{\mathrm{CNT}}_{\boldsymbol{G},\boldsymbol{G}'}(\boldsymbol{q})$ as in Eq. (4.3) through the three-dimensional plane-wave expansion, the reciprocal lattice vectors $\boldsymbol{G}$ depending on the size of the supercell containing a tube replica. Throughout we use the acronym CNT to discriminate relevant quantities obtained in this section from the corresponding first-principles and EM results.

Here we use a cylindrical supercell to contain the single NT unit (Fig. 4.4). As the tube model structure is a sequence of rings along the axis, we identify a single ring as the building unit of the tube and hence allocate each ring of given axial coordinate y in a different supercell. Thus, the length of the supercell λ along the axis is equal to the distance between two subsequent rings, and the total length of the nanotube A just amounts to $A = N\lambda$, where N is the number of repetitions of the supercell along the axis. We work with a discretized set of axial wave vectors $q \to q_j$, where $q_j = 2\pi j/A$ with $j = -N/2, ..., N/2$. In the directions perpendicular to the nanotube axis we arrange the cylindrical supercells in a square superlattice with side equal to twice the radius of the supercell, $\mathfrak{R}$. We take $\mathfrak{R}$ to be much larger than R to avoid quantum mechanical interactions among replicas. Since the quantities of interest are obtained by sums over reciprocal lattice vectors, it is convenient to derive both axial and trasverse components, respectively $\boldsymbol{G}_{\parallel}$ and $\boldsymbol{G}_{\perp}$, in Cartesian form, from the periodic boundary conditions for the square superlattice:

$$\boldsymbol{G}_{\perp} = \frac{\pi}{\mathfrak{R}}\left(n_1\hat{x} + n_3\hat{z}\right), \quad \boldsymbol{G}_{\parallel} = \frac{2\pi}{\lambda}n_2\hat{y}, \tag{4.20}$$

where $n_i = 0, \pm1, \pm2, \ldots$, and $i = 1, 2, 3$. The set of vectors over which we sum is determined through both a radial and an axial cutoff of the vector modulus, respectively $|\boldsymbol{G}_{\perp}| \leq G_{\perp\mathrm{max}}$ and $\boldsymbol{G}_{\parallel} \leq G_{\parallel\mathrm{max}}$, the error with respect to the usage of cylindrical coordinates being small in the limit of a dense set.

In order to describe an isolated tube and hence avoid spurious Coulomb in-

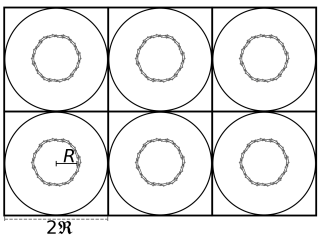

Figure 4.4: Sketch of the supercell structure in the non-periodic directions. Cylindrical supercells of radius $\mathfrak{R}$ are replicated and arranged on a square lattice. Each supercell contains a tube section, modeled as a ring of homogeneous charge, of radius R.

teractions among replicas of the system, which are due to the long range of the potential, we follow Ref. [118] and employ a form of the interaction that is truncated along the transverse directions:

$$v(\mathbf{q}+\mathbf{G}) = v_{\text{full}}(\mathbf{q}+\mathbf{G})\Big[1 + \mathfrak{R}\, G_\perp\, J_1(\mathfrak{R}G_\perp)\, K_0(\mathfrak{R}|q+G_\parallel|) \quad + \\ - \quad \mathfrak{R}\,|q+G_\parallel|\, J_0(\mathfrak{R}G_\perp)\, K_1(\mathfrak{R}|q+G_\parallel|)\Big]. \quad (4.21)$$

Here v_{full} is the standard, bare three-dimensional Coulomb potential,

$$v_{\text{full}}(\mathbf{q}+\mathbf{G}) = \frac{4e^2}{A\mathfrak{R}^2(\mathbf{q}+\mathbf{G})^2}, \quad (4.22)$$

$J_0(x), J_1(x)$ are Bessel functions of first kind, $K_0(x), K_1(x)$ are modified Bessel functions of second kind, and $\mathbf{q} = q\hat{y}$. In the case of armchair tubes only, which are gapless, we use v_{full} instead of v as the full dressed interaction is cut-off in reciprocal space, and hence harmless.

The truncated potential v oscillates in reciprocal space and is less divergent than v_{full} at long wavelength, as Bessel functions $J_0(x), J_1(x)$ occurring in Eq. (5.3) vanish with the argument x. As v decreases quadratically with the magnitude of reciprocal lattice vectors, it is sufficient to include a limited number of $\boldsymbol{G}$ to reconstruct the Coulomb potential, either in real space [Eq. (5.1) for the dressed potential W] or projected onto NT orbitals. Since the smallest $\boldsymbol{G}_\parallel$'s have magnitudes much larger than the first $\boldsymbol{G}_\perp$'s, the most relevant Fourier components are those with $\boldsymbol{G}_\parallel = 0$ and $\boldsymbol{G}_\perp$ finite and small. In order to achieve convergence, both the supercell radius $\mathfrak{R}$ and the cutoffs $G_{\perp\text{max}}$ and $G_{\parallel\text{max}}$ must be carefully chosen, differing for the bare and screened Coulomb potential. The reconstruction of the bare potential requires large supercells and many $\mathbf{G}$ vectors, whereas the screened potential converges faster. For the dressed potential W, we take $\mathfrak{R} = 7R$ and $-15 \leq n_1, n_3 \leq 15$, including only the smallest finite axial vector $\boldsymbol{G}_\parallel$.

4.3.3 Dielectric function and dressed Coulomb potential

The derivation of the polarisation $\Pi^{\text{CNT}}_{\boldsymbol{G},\boldsymbol{G}'}(\boldsymbol{q})$ requires the knowledge of the overlap integrals ρ_{cv} between c and v states that occur in Eq. (4.3). We compute these integrals by expanding the Bloch states Eq. (4.18) over the basis of three-dimensional plane waves with wave vector $\boldsymbol{G}+\boldsymbol{q}$, as detailed in Appendix A.1. Explicitly, one

has

$$\epsilon^{\text{CNT}}_{\boldsymbol{G},\boldsymbol{G'}}(\boldsymbol{q}) = \delta_{\boldsymbol{G},\boldsymbol{G'}} - \frac{2A}{\pi} v(\mathbf{q}+\mathbf{G}) \sum_{\alpha,\alpha'} \sum_{\tau} \int_{-k_o}^{k_o} dk \\ \langle \alpha\tau k | e^{-i(\boldsymbol{G}+\boldsymbol{q})\cdot\boldsymbol{r}} | \alpha'\tau k+q \rangle \langle \alpha'\tau k+q | e^{i(\boldsymbol{G'}+\boldsymbol{q})\cdot\boldsymbol{r'}} | \alpha\tau k \rangle \\ \times \quad \frac{f(E_{\alpha'\tau'}(k+q)) - f(E_{\alpha\tau}(k))}{E_{\alpha'\tau'}(k+q) - E_{\alpha\tau}(k)}, \quad (4.23)$$

with the overlap integrals being given by

$$\langle \alpha k | e^{-i(\boldsymbol{G}+\boldsymbol{q})\cdot\boldsymbol{r}} | \alpha' k+q \rangle \quad = \left[(F^A_{\tau\alpha k})^* F^A_{\tau\alpha' k+q} + (F^B_{\tau\alpha k})^* F^B_{\tau\alpha' k+q}) \right] J_0(RG_\perp) \quad = \\ \frac{1}{2} \left(\frac{k(k+q) + k_\tau^2 - iqk_\tau}{\sqrt{k^2+k_\tau^2}\sqrt{(k+q)^2+k_\tau^2}} + (2\delta_{\alpha,\alpha'} - 1) \right) J_0(RG_\perp). \quad (4.24)$$

Note that the overlap integral is similar to its EM counterpart Eq. (4.14) except for the presence of the Bessel function J_0 of argument $RG_\perp$. This factor, absent in the EM expression, provides ϵ^{CNT} with the explicit dependence on tube curvature. After integration over k and in the limit $k_o \to \infty$, the dielectric function reads:

$$\epsilon^{\text{CNT}}_{\boldsymbol{G},\boldsymbol{G'}}(\boldsymbol{q}) = \delta_{\boldsymbol{G},\boldsymbol{G'}} + \frac{2A}{\pi\gamma} v(\boldsymbol{q}+\boldsymbol{G}) J_0(RG_\perp) J_0(RG'_\perp) \\ \times \quad \sum_{\tau} \left[1 + \frac{2k_\tau^2}{q\sqrt{q^2+4k_\tau^2}} \log \left(\frac{\sqrt{q^2+4k_\tau^2} - q}{\sqrt{q^2+4k_\tau^2} + q} \right) \right]. \quad (4.25)$$

In this work we focus on the matrix elements of the screened Coulomb interaction that bind electrons and holes together, mainly at small momentum transfer, q. Due to symmetry, electron-hole and electron-electron interaction have the same magnitude. The interaction matrix element, $W^\tau(k, k+q)$, is obtained by projecting the screened potential (4.1) over the electron-hole pair states $(c,\tau,k)(v,\tau,k+q)$ and $(c,\tau,k+q)(v,\tau,k)$ within the same valley τ:

$$W^\tau(k,k+q) = \sum_{\boldsymbol{G}} \sum_{\boldsymbol{G'}} \langle c\tau k | e^{-i(\boldsymbol{G'}+\boldsymbol{q})\cdot\boldsymbol{r'}} | c\tau k+q \rangle \langle v\tau k+q | e^{i(\boldsymbol{G}+\boldsymbol{q})\cdot\boldsymbol{r}} | v\tau k \rangle \\ \times \quad (\epsilon_{\boldsymbol{G},\boldsymbol{G'}}(\boldsymbol{q}))^{-1} v(\boldsymbol{q}+\boldsymbol{G'}). \quad (4.26)$$

Since the corresponding first-principles quantity is evaluated on the grid $(k_j, k_j + q_l)$, it is convenient to integrate $W^\tau(k, k+q)$ over the reciprocal-space mesh $2\pi/A$.

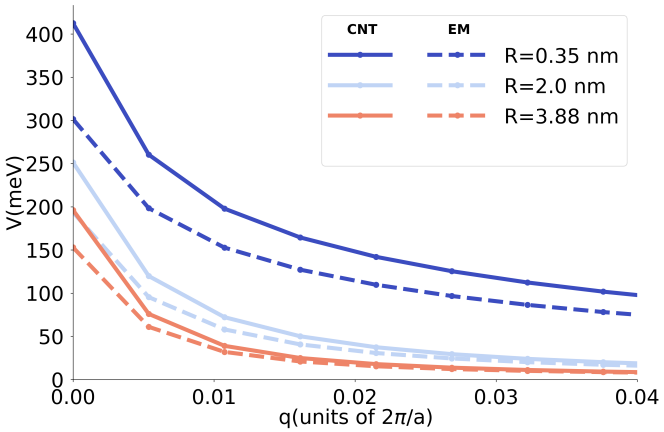

Figure 4.5: Bare electron-hole interaction $V^{\tau}(q)$ vs q computed from effective-mass theory (EM) and supercell model (CNT) for different tube radii R.

After inserting expressions (4.25) and (4.24) into (4.26), one obtains:

$$W^{\tau}_{\mathrm{CNT}}(k_j, k_j{+}q_l) = \frac{A}{4\pi}\int_{q_l-\pi/A}^{q_l+\pi/A} dq \sum_{\boldsymbol{G}}\sum_{\boldsymbol{G'}} J_0(RG'_{\perp})\, J_0(RG_{\perp})[\epsilon^{\mathrm{CNT}}_{\boldsymbol{G},\boldsymbol{G'}}(\boldsymbol{q})]^{-1} v(\boldsymbol{q}{+}\boldsymbol{G'}) \left(1 + \frac{k_j(k_j+q)+k_\tau^2}{\sqrt{k_j^2+k_\tau^2}\sqrt{(k_j+q)^2+k_\tau^2}}\right). \quad (4.27)$$

Note that integration regularizes the logarithmic singularity of Coulomb potential (4.21) for $q \to 0$, as $v(\mathbf{q}+\mathbf{G}_{\perp}) \simeq -\log(\Re\,|q|)$ for all allowed $G_{\perp}$. For reference, the corresponding EM matrix element is:

$$W^{\tau}_{\mathrm{EM}}(k_j, k_j+q_l) = \frac{e^2}{2\pi}\int_{q_l-\pi/A}^{q_l+\pi/A} dq\, \epsilon^{-1}_{\mathrm{EM}}(q)\, I_0(qR)\, K_0(qR) \times \left(1 + \frac{k_j(k_j+q)+k_\tau^2}{\sqrt{k_j^2+k_\tau^2}\sqrt{(k_j+q)^2+k_\tau^2}}\right). \quad (4.28)$$

4.4 Bare electron-hole interaction

The key improvement of the supercell model of Sec. 4.3 with respect to the effective-mass theory of Sec. 4.2 shows up even in the absence of screening, when projecting the bare electron-hole interaction onto c and v Bloch states. This

quantity, $V(q)$, is the matrix element $W^\tau(k_j, k_j + q_l)$ of equations (4.27) and (4.28) evaluated for vanishing electronic polarisation, $\Pi = 0$, that is $V^\tau(q_l) = [W^\tau(0, q_l)]_{\Pi=0}$.

We compare in Fig. 4.5 the supercell model and EM matrix elements, respectively $V^\tau_{\text{CNT}}(q_l)$ and $V^\tau_{\text{EM}}(q_l)$, for different NT radii R. Recall that the numerical discretization of momentum space regularizes the logarithmic singularity expected for $q \to 0$. The supercell model bare electron-hole interaction systematically exceeds its EM counterpart, as only the former is sensitive to the curved tube topology. The enhancement of the interaction originates from the the form factors of the kind $J_0(RG_\perp)$ that modify graphene overlap integrals. The mismatch between V_{CNT} and V_{EM} is stronger for smaller R and softens as the tube curvature becomes negligible.

Note that V_{CNT} and V_{EM} build on different expression of the full, non-projected Coulomb potential, depending respectively on $\boldsymbol{G}$ vectors and azimuthal quantum numbers m. However, the two potential forms, once evaluated on the same cylindrical surface of radius R, are identical at long wavelength in the macroscopic limit, $v \sim 2e^2/A \log(A/R)$, as we show explicitly in Appendix A.4.

4.5 Dielectric function

Large-gap semiconducting carbon nanotubes are known to poorly screen charge carriers at electron-electron separations that are either large or small with respect to the NT radius, as an effect of the low dimensionality [113, 114]. Our calculations from first principles for narrow-gap NTs show a qualitatively similar behaviour, provided one replaces the crossover length R with $|k_\tau|^{-1}$.

Figure 4.6 (a) reports the dependence of the inverse "macroscopic" dielectric function $\epsilon^{-1}_{0,0}(\boldsymbol{q})$ on the wave vector q for the (9,0) zigzag NT (red curve), whose calculated gap is 110 meV. For both small and large q the inverse dielectric constant is close to one, the crossover occurring close to $q \approx |k_\tau| = 6 \times 10^{-3}$ $2\pi/a$. The trend of ϵ^{-1} of is qualitatively similar to that of large-gap NTs, like the (8,0) tube shown in Fig. 1a of Deslippe *et al.* [114], except for the different crossover location. The rationale is that, for large-gap semiconducting NTs, the "secondary" contribution to the gap, due to curvature and proportional to $|k_\tau|$ as defined in Eq. (4.8), is negligible with respect to the "primary gap" proportional to $1/R$, whereas in narrow-gap NTs the primary gap is absent [2]. The gapless limit of armchair tubes is regained for $k_\tau \to 0$, which allows for metallic screening at long wavelength, i.e., $\epsilon^{-1}_{0,0}(q = 0) = 0$. This is shown for the (3,3) tube by the red curve of Fig. 4.6 (b), which exactly reproduces Fig. 2 of Spataru *et al.* [156]. This result, which builds on the full bare potential v_{full}, is cell-independent and hence may be used a benchmark for model approaches, whereas $\epsilon^{-1}_{0,0}(\boldsymbol{q})$ of panel

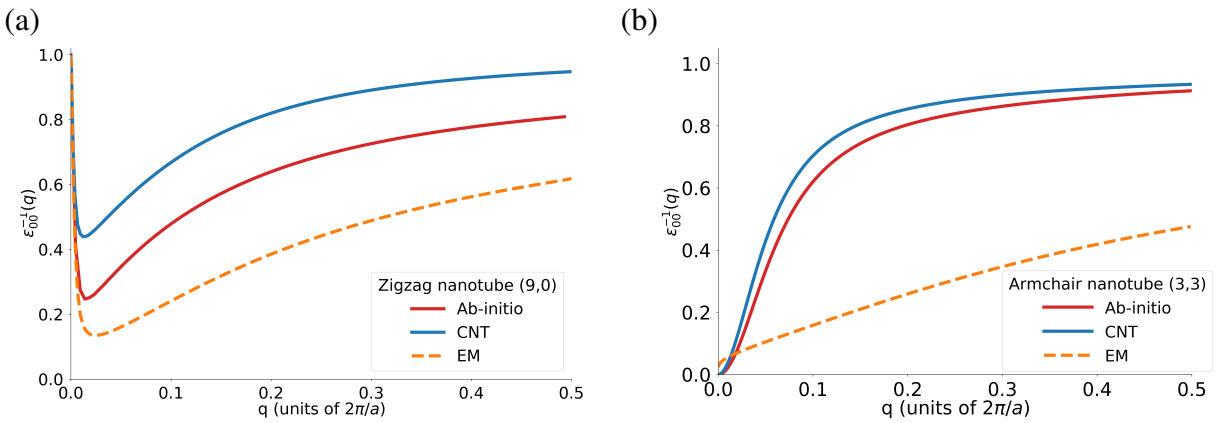

Figure 4.6: Macroscopic dielectric function $\epsilon^{-1}_{0,0}(q)$ vs q computed from first principles (ab initio), effective-mass theory (EM), and supercell model (CNT). Panels (a) and (b) show data for zigzag (9,0) and armchair (3,3) nanotubes, respectively.

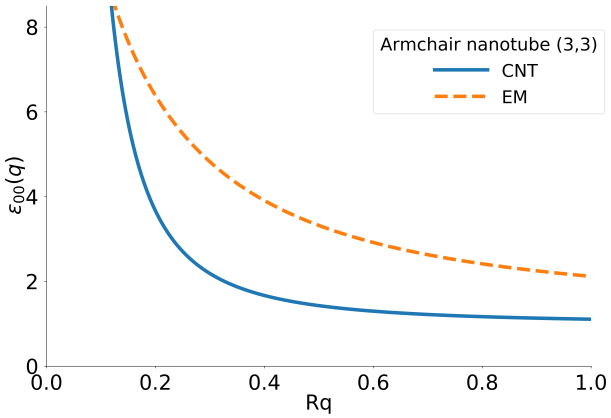

Figure 4.7: Macroscopic dielectric function $\epsilon_{0,0}(q)$ vs q computed from effective-mass theory (EM), and supercell model (CNT) in the armchair (3,3) nanotube.

(a) depends on the supercell size.

The supercell model calculation of $\epsilon^{-1}_{0,0}$ (blue curves in Fig. 4.6, CNT) reproduces quantitatively the inverse dielectric constant of the armchair tube from first principles, the difference between ab-initio and CNT curves remaining small in the whole q range. On the other hand, a direct comparison with the zigzag tube is not possible, due to the size mismatch between first-principles and model supercells, which affects the magnitude of the macroscopic bare truncated potential v and hence $\epsilon^{-1}_{0,0}$. The systematic enhancement of the model result with respect to first-principles data is likely due to the neglect of higher-energy virtual electron-hole excitations, which are responsible for the screening effect.

Contrary to the model prediction, the EM calculation of the inverse dielectric

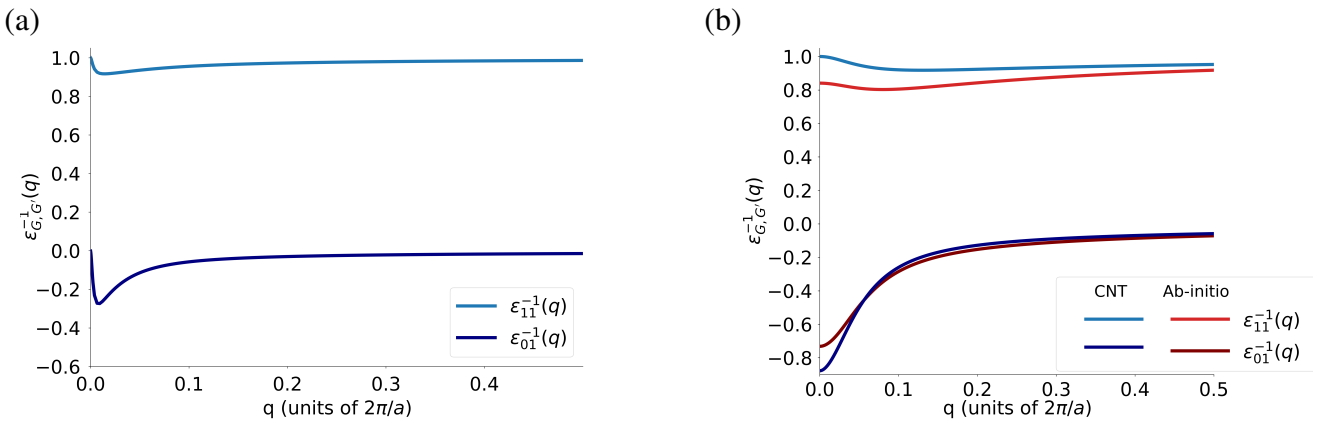

Figure 4.8: Diagonal, $\epsilon^{-1}_{\boldsymbol{G}_\perp,\boldsymbol{G}_\perp}(\boldsymbol{q})$, and wing term, $\epsilon^{-1}_{0,\boldsymbol{G}_\perp}(\boldsymbol{q})$, of the inverse dielectric matrix vs momentum q for the smallest vector $\boldsymbol{G}_\perp$ with $n_1 = 1$, $n_2 = n_3 = 0$. Panel (a): Supercell model results for the (9,0) zigzag nanotube. Panel (b): first-principles (ab initio) and model (CNT) results for the (3,3) armchair nanotube.

constant performs poorly for the armchair tube [dashed curve in Fig. 4.6(b) and Fig. 4.7], even failing to reproduce the correct curvature of $\epsilon^{-1}_{0,0}(q)$ at $q \approx 0$ and grossly missing its magnitude. Regardless of chirality, the EM theory overestimates substantially the electronic polarization with respect to the supercell model. The misjudgement is even more pronounced in the EM model in literature (eg Fig(4b) of Tomio *et al.* [157] compared to Fig. 4.7) as the two-band approximation adopted here is mainly thought for the small q region and does not work perfectly at large q missing the higher-energy subbands.

We have checked that the non-local terms of the inverse dielectric matrix $\epsilon^{-1}_{\boldsymbol{G},\boldsymbol{G}'}(\boldsymbol{q})$ that have finite transverse vectors $\boldsymbol{G}_\perp$ strongly affect the dressed electron-hole interaction W. The most relevant terms turn out to be the diagonal matrix elements of kind $\epsilon^{-1}_{\boldsymbol{G}_\perp,\boldsymbol{G}_\perp}(\boldsymbol{q})$ and the "wing" terms of type $\epsilon^{-1}_{\boldsymbol{G}_\perp,0}(\boldsymbol{q})$ [or $\epsilon^{-1}_{0,\boldsymbol{G}_\perp}(\boldsymbol{q})$]. For the sake of illustration, Fig. 4.8 shows the dependence of the first diagonal and wing matrix elements of ϵ^{-1} on momentum q for selected tubes. The shown trend is generic for all vectors $\boldsymbol{G}_\perp$, the model and first-principles results being almost identical. The diagonal elements are close to unity and thus enhance the dressed interaction, whereas the wing terms are small and negative, thus increasing the screening effect. As clear from Eq. (4.27), as the magnitude of $\boldsymbol{G}_\perp$ increases the weight of its contribution to W decreases approximately as $|\boldsymbol{G}_\perp|^{-2}$.

At long wavelength, gapped and gapless tubes behave differently. As shown for the gapped zigzag (9,0) tube in panel (a), both diagonal and wing terms of the inverse dielectric constant exhibit a minimum close to $q \approx |k_\tau|$, like the macroscopic term $\epsilon^{-1}_{0,0}$ of Fig. 4.6(a), corresponding to a maximum of the polarisation Π. For $q \to 0$ the polarisation vanishes quadratically, as apparent from the analytical

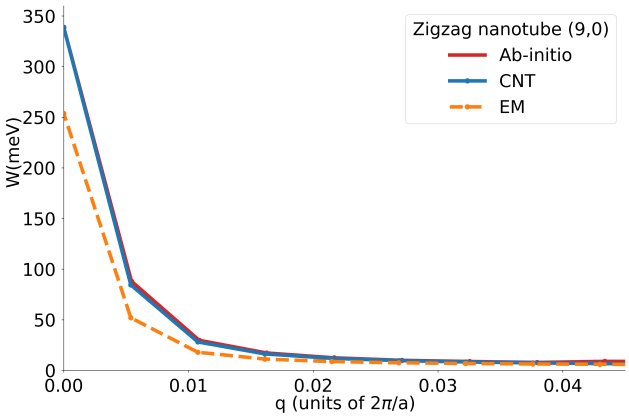

Figure 4.9: Screened electron-hole interaction $W(q)$ vs q for the zigzag (9,0) nanotube derived from first-principles (ab-initio), effective mass (EM) and and supercell model (CNT) approaches.

behaviour of the model polarisation (only valid in the presence of the gap),

$$\Pi^{\mathrm{CNT}}_{\boldsymbol{G},\boldsymbol{G}'}(\boldsymbol{q} \simeq 0) = -\frac{2A}{3\pi\gamma k_\tau^2}\, q^2 J_0(RG_\perp) J_0(RG'_\perp). \tag{4.29}$$

Therefore, the diagonal (wing) term tends to unity (zero). For gapless tubes, like the (3,3) armchair tube of Fig. 4.8(b), the maximum of Π moves to $q = 0$ together with the mimimum of wing terms, whereas the diagonal terms weakly depend on q.

4.6 Screened electron-hole interaction

The key quantity we focus on is the screened, momentum-dependent electron-hole interaction, $W(q)$, projected on c and v bands. This matrix element provides the Bethe-Salpeter equation of motion for excitons with the non-trivial information about screening. Furthermore, the dressed interaction obtained from the supercell and EM approaches, $W(q) = W^\tau(0, q_l)$ as defined in equations (4.27) and (4.28), may be directly compared with the matrix element obtained from first principles, for given sampling of momentum space. In this subsection we discuss gapped NTs and postpone the gapless case to subsection 4.7, as the latter case requires special handling in view of its singular behaviour in the limit $q \to 0$, $k_\tau \to 0$.

As illustrated by Fig. 4.9, the supercell model calculation of W_{CNT} (blue curve) agrees very well with first-principles data (red curve) for the zigzag (9,0) tube. On the contrary, EM theory (dashed curve) substantially overestimates screening at small momentum transfer, and hence invariably underestimates exciton binding energies. The key to the perfect matching of first-principles and model approaches

is the full inclusion of local-field effects, as illustrated by the model calculation of Fig. 4.10. Here we separate the "macroscopic" and "microscopic" contributions to $W(q)$ of equation (4.27) in the sum over terms proportional to $\epsilon^{-1}_{\boldsymbol{G}_\perp,\boldsymbol{G'}_\perp}(\boldsymbol{q})$, where the former is term $(\boldsymbol{G}_\perp, \boldsymbol{G'}_\perp) = (0,0)$ and the latter is the remainder of the sum. The macroscopic term provides W with the gross contibution, but local-field terms are essential to regain the actual potential. Whereas diagonal terms $(\boldsymbol{G}_\perp, \boldsymbol{G}_\perp)$ increase the interaction strength and are most effective at $q \approx 0$, the wing terms $(\boldsymbol{G}_\perp, 0)$ enhance screening and are most relevant for $q > |k_\tau|$, where the microscopic contribution (labeled $W_{CNT} - W_{macro}$) becomes negative.

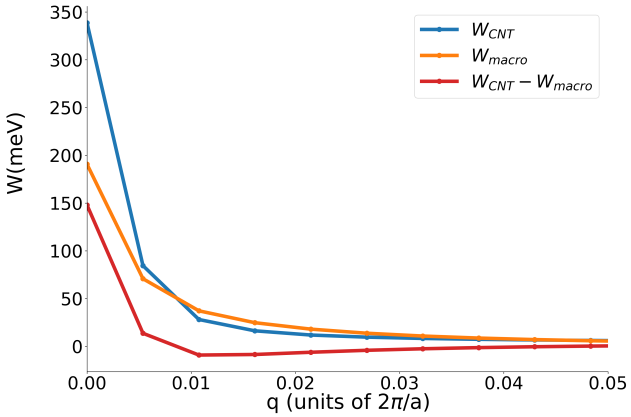

Figure 4.10: Macroscopic and microscopic contribution to the model dressed electron-hole interaction, $W(q)$ vs q, for the zigzag (9,0) nanotube. In the sum over terms depending on $\epsilon^{-1}_{\boldsymbol{G}_\perp,\boldsymbol{G'}_\perp}(\boldsymbol{q})$, the macroscopic term ($W_{macro}$) corresponds to $(\boldsymbol{G}_\perp, \boldsymbol{G'}_\perp) = (0,0)$ and the microscopic term ($W_{CNT} - W_{macro}$) is the remainder.

The model calculation allows to derive the screened electron-hole interaction for tubes of any radius, R, and gap size, E_g, the latter being fixed by the combination of R and θ given in equation (4.8). This is illustrated for selected sets of (R, E_g) values by Figs. 4.11 and 4.12. Here we fix either the radius ($R = 1$ nm in Fig. 4.11) or the gap size ($E_g = 20$ meV in Fig. 4.12) and plot the dressed interaction $W(q)$ as a function of the renormalized momentum $q/|k_\tau|$. All plots of W exhibit an almost identical dependence on $q/|k_\tau|$, which demonstrates that the most relevant length scale is $|k_\tau|^{-1}$, whereas the absolute magnitude of W at long wavelength, $W(q = 0)$, depends in a non-trivial way on both R and $|k_\tau|^{-1}$. In particular, $W(q = 0)$ decreases weakly with R for given energy gap (Fig. 4.12), whereas the bare interaction $V(q = 0)$ substantially depends on R (Fig. 4.5). Thus, screening tends to weaken the dependence of the dressed potential on R and to enhance that on $|k_\tau|^{-1}$. A key result is that, for $q < |k_\tau|$, EM and supercell model predictions systematically depart, the EM approximation substantially overestimating screening.

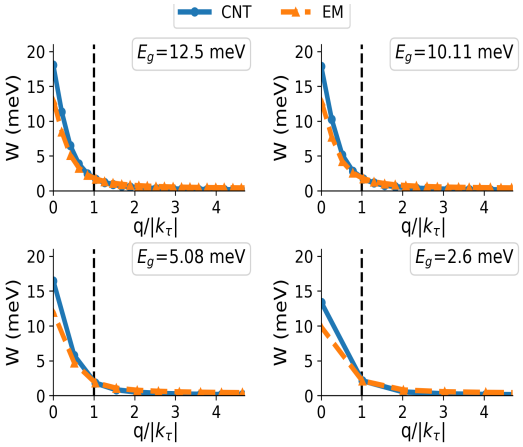

Figure 4.11: Screened electron-hole interaction potential, $W(q)$, vs renormalized momentum, $q/\left|k_\tau\right|$, from model and effective-mass calculations, for different gap values, E_g. The nanotube radius is fixed, $R = 1$ nm, and the vertical dashed line corresponds to $q = |k_\tau|$.

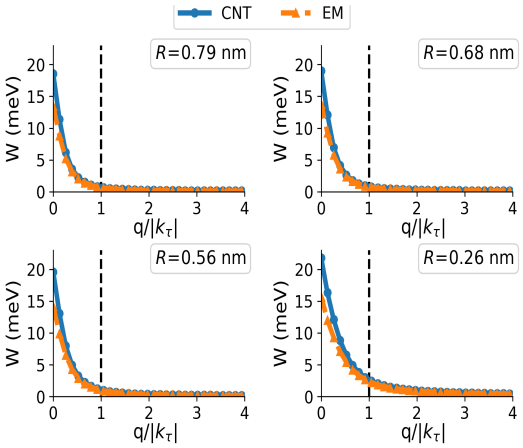

Figure 4.12: Screened electron-hole interaction potential, $W(q)$, vs renormalized momentum, $q/\left|k_\tau\right|$, from model and effective-mass calculations, for different nanotube radii, R. The nanotube gap is fixed, $E_g = 20$ meV, and the vertical dashed line corresponds to $q = |k_\tau|$.

4.7 Armchair tubes and excitonic instability

As the gap vanishes, as in armchair NTs, screening acquires a metallic character, becoming effective even at long wavelength. As a consequence, the electronic polarization Π exhibits a non-analytic behaviour in the limit $q \to 0$, $k_\tau \to 0$. This is illustrated by the quadratic expansion of Π (Eq. 4.29) for small q values, which tends to zero or infinity depending on the order of the limits $\lim_{q\to 0}$ and $\lim_{k_\tau \to 0}$.

A counterpart to the singularity of Π is the enhanced role of microscopic local fields in the building of the dressed electron-hole interaction, as shown in Fig. 4.13

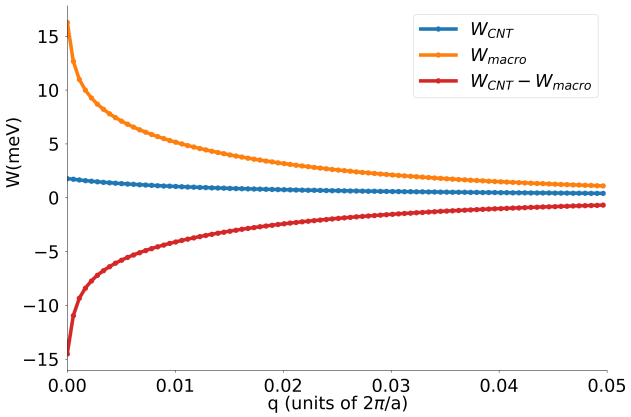

Figure 4.13: Macroscopic and microscopic contribution to the model dressed electron-hole interaction, $W(q)$ vs q, for the armchair (5,5) nanotube. In the sum over terms depending on $\epsilon^{-1}_{\boldsymbol{G}_\perp,\boldsymbol{G'}_\perp}(\boldsymbol{q})$, the macroscopic term ($W_{macro}$) corresponds to $(\boldsymbol{G}_\perp, \boldsymbol{G'}_\perp) = (0,0)$ and the microscopic term ($W_{CNT} - W_{macro}$) is the remainder.

for the armchair (5,5) tube. Here the microscopic contribution ($W_{CNT} - W_{macro}$) to W is large and negative for $q \to 0$, due to dominance of wing terms $(\boldsymbol{G}_\perp, 0)$ in the sum over $(\boldsymbol{G}_\perp, \boldsymbol{G'}_\perp)$, sensitive to the magnitude of Π. This enhancement leads to a major cancellation of the macroscopic term $(\boldsymbol{G}_\perp, \boldsymbol{G'}_\perp) = (0,0)$, which has opposite sign and comparable magnitude (W_{macro} in Fig. 4.13), and hence requires careful numerical handling.

In order to achieve high numerical accuracy, we correct the model polarization Π through a multiplicative factor, q- and θ-dependent, which very slightly differs

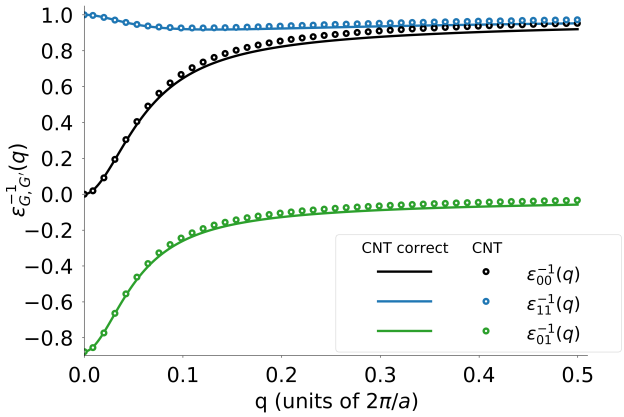

Figure 4.14: Corrected vs original matrix elements of the model dielectric function for the armchair (3,3) nanotube. Head term, $\epsilon^{-1}_{0,0}(\boldsymbol{q})$, diagonal term, $\epsilon^{-1}_{\boldsymbol{G}_\perp,\boldsymbol{G}_\perp}(\boldsymbol{q})$, and wing term, $\epsilon^{-1}_{0,\boldsymbol{G}_\perp}(\boldsymbol{q})$, vs q for the smallest vector $\boldsymbol{G}_\perp$ with $n_1 = 1$, $n_2 = n_3 = 0$.

from unity. We derive this factor by fitting the macroscopic, first diagonal, and first wing terms of Π to first-principles data, according to

$$\Pi^{\text{correct}}_{\boldsymbol{G},\boldsymbol{G}'}(\boldsymbol{q}) = \Pi^{\text{CNT}}_{\boldsymbol{G},\boldsymbol{G}'}(\boldsymbol{q}) \left\{ 5\cos[2.7\,(\pi/6-\theta)]Rq + 0.107\,[R/(1\text{ Å})]^{1.46} \right\}. \quad (4.30)$$

Here the numerical coefficients fit the first-principles matrix elements of armchair tubes (3,3), (4,4), (5,5), and zigzag tubes (9,0), (12,0). As this correction is immaterial for zigzag tubes, we employ the corrected form Π^{correct} throughout the paper. For the sake of illustration, we compare the corrected and uncorrected terms of ϵ^{-1} for the (3,3) armchair tube in Fig. 4.14, the discrepancies being small and only relevant at short wavelength. The correction of Π allows for an excellent matching between model and first-principles predictions of the dressed electron-hole interaction in armchair tubes, as shown in Fig. 4.15.

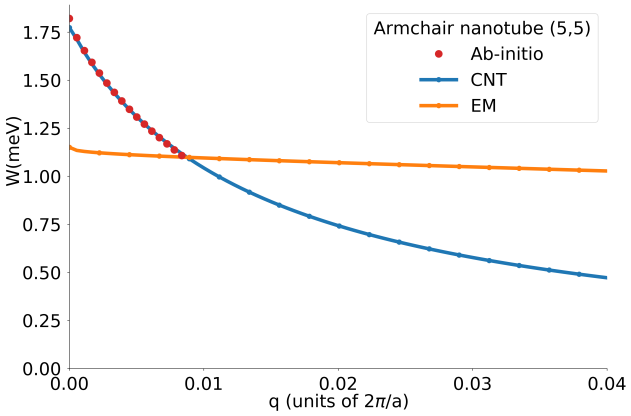

Figure 4.15: Screened electron-hole interaction $W(q)$ vs q for the armchair (5,5) nanotube derived from first-principles (ab-initio), effective mass (EM) and and supercell model (CNT) approaches.

Figure 4.15 illustrates the key findings of this chapter. The EM theory (orange curve) predicts that the dressed electron-hole attraction depends weakly on the transferred momentum q in gapless tubes, hence corresponding to a short-range force. The force range is given by the expression (4.15) of Π_{EM} for $k_\tau \to 0$, i.e., $\Pi_{\text{EM}}(q) = -4A/\pi\gamma$, with $4A/\pi\gamma$ being the density of states. This is just the Thomas-Fermi result for an effectively one-dimensional metal. On the contrary, both first-principles (red dots) and supercell model calculations (blue curve) predict that W has a singular-like profile at long wavelength, roughly logarithmic [28], signaling that the force binding electrons and holes is actually long-ranged. As W in Figure 4.15 is represented once integrated over the reciprocal-space mesh (Eq. 4.27), the singular-like profile here appears as a finite peak. The singular-like profile of W is a substantial effect of microscopic local fields, which emerges as electrons effectively move on a cylindrical surface and not on a line.

	Triplet	Singlet
Ab initio (Ref. 27)	-7.91meV	-6.10 meV
CNT correct	-7.07 meV	-5.22 meV
CNT, tiny gap	-5.79meV	-4.87meV
CNT, gapless	-2.00 meV	-1.13 meV

Table 4.1: Excitation energy of the lowest lying triplet and singlet exciton in the (3,3) armchair carbon nanotube from first-principles (ab intio) and model (CNT) approaches.

As a consequence, gapless tubes are unstable against the spontaneous condensation of excitons [28], whereas the EM theory [5] predicts the exciton binding energy to vanish with the gap.

We will use the results of the present work to treat excitonic effects in narrow-gap NTs elsewhere. In order to complete our discussion of gapless tubes, here we reconsider the calculation of exciton properties from first principles reported in Ref. [28]. In the calculation by Varsano *et al.*[28] for the (3,3) armchair tube, the system was actually gapped by a tiny quantity, 1.08 meV, arising from the numerical discretization of the reciprocal space. In the following we show that this artefact does not harm the claim of excitonic instability.

First, the tiny gap does not affect the calculation of ϵ^{-1} reported in Figs. 4.6(b) and 4.8(b) in any way, since: (i) the reciprocal-space mesh in energy units, $\gamma\,\mathrm{d}q = 1.5$ meV, is obviously larger than the gap (ii) the computed macroscopic inverse dielectric constant, $\epsilon^{-1}_{0,0}(q)$, already vanishes at small momenta $q > \mathrm{d}q$, as apparent from Fig. 4.6(b).

Furthermore, we checked the effect of the artificial gap on the exciton energy, by numerically solving the Bethe-Salpeter equation within the supercell model for the screened interaction presented in this paper. The resulting excitation energies of the lowest singlet and triplet excitons are reported in Table 4.1 (CNT correct) for the gap being exactly zero, and compared with the first-principles results (ab initio). The discrepancies are minor, smaller than 1 meV and of the order of magnitude of the artificial gap. One might also wonder whether the supercell model calculation performed without applying the corrective factor to Π, which fits first-principles data, were still able to predict the excitonic instability. The results of such calculation, respectively in the presence of the tiny gap (CNT, tiny gap) and in the gapless case (CNT, gapless), are reported in the last two rows of Table 4.1. In all events the excitation energy of the exciton remains negative, which points to the tendency of excitons to spontaneously form.

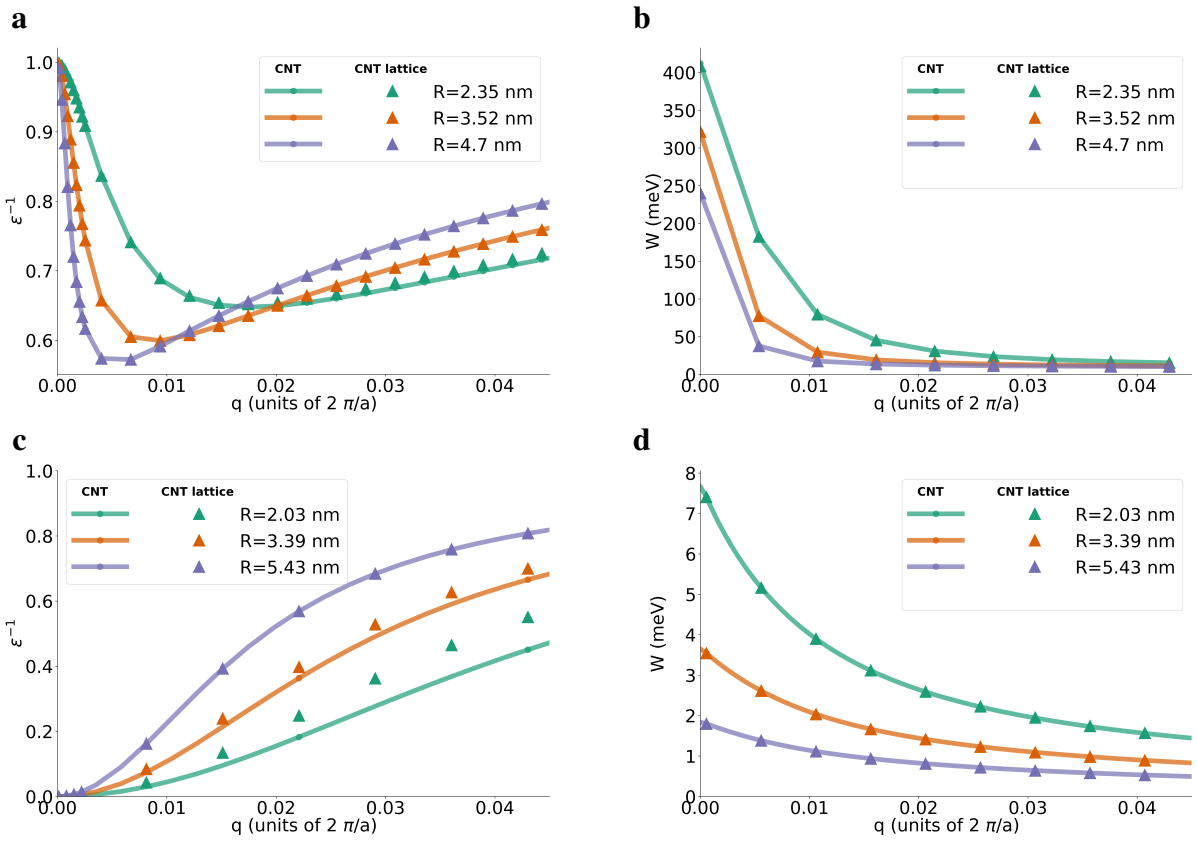

Figure 4.16: Macroscopic inverse dielectric function, $\epsilon^{-1}_{0,0}(q)$ (panel a and c), and screened electron-hole interaction, $W(q)$ (panel b and d), vs momentum, q, computed from different model approaches for selected zigzag (a and b) and armchair (c and d) nanotubes, respectively. Data are derived by considering either the lattice structure (triangles) or by spreading homogeneously the electronic charge (solid curves) over the cylindrical tube surface.

4.8 Validation of the structural model through comparison with results for armchair and zigzag lattices

Throughout this work we model the carbon nanotube structure as a cylindrical surface over which the electrons occupying the Bloch states $\psi(\boldsymbol{r})$, which multiply the envelopes in Eq. (6.1), are spread homogeneously according to the ansatz of Eq. (4.18) (see Subsec. 4.3.1). In this subsection we validate this model by comparing both the dielectric function and the screened electron-hole interaction with those computed by considering the actual location of atoms in the curved honeycomb lattice. To this aim, we replace the "jellium" of Eq. (4.18) with orbitals

localized on either the zigzag or the armchair lattice, as detailed in Appendixes A.2 and A.3, respectively. This change affects the overlap integrals that enter the expressions of the dielectric function (Eq. 4.23) and screened electron-hole interaction (Eq. 4.26). As we show below, the discrepancies are minor.

4.8.1 Zigzag lattice

Zigzag carbon nanotubes $(n,0)$ have a chiral vector $\boldsymbol{\mathcal{C}} = n\boldsymbol{a}$ stretching over n units cells of graphene (the vectors $\boldsymbol{a}$ and $\boldsymbol{b}$ are shown in Fig. 4.1). Whereas in the simpler structural model the n units cells are represented as two rings and the electron charges are spread into a "jellium", here we consider all n cells and all $2n$ atom positions per sublattice. The overlap integrals, derived in Appendix A.2, are:

$$\langle \alpha k | e^{-i(\boldsymbol{G}+\boldsymbol{q})\cdot\boldsymbol{r}} | \alpha' k+q \rangle = \frac{1}{2}\left[\frac{k(k+q)+k_\tau^2 - iqk_\tau}{\sqrt{k^2+k_\tau^2}\sqrt{(k+q)^2+k_\tau^2}} + (2\delta_{\alpha,\alpha'}-1)\right] \times \quad \left[J_0(RG_\perp) + 2(-1)^n J_{2n}(RG_\perp)\right], \quad (4.31)$$

with J_{2n} being the Bessel function of first kind of order $2n$. This overlap integral is similar to the "jellium" expression (4.24) except for the correction due to the higher order Bessel function, the order being linked to the number of atoms in the cell.

Similarly, the dielectric function is:

$$\epsilon^{\text{zigzag}}_{\boldsymbol{G},\boldsymbol{G'}}(\boldsymbol{q}) = \delta_{\boldsymbol{G},\boldsymbol{G'}} + \frac{2A}{\pi\gamma}\, v(\boldsymbol{q}+\boldsymbol{G}) \left[J_0(RG_\perp) + 2(-1)^n J_{2n}(RG_\perp)\right] \left[J_0(RG'_\perp) + 2(-1)^n J_{2n}(RG'_\perp)\right] \sum_\tau \left[1 + \frac{2k_\tau^2}{q\sqrt{q^2+4k_\tau^2}} \log\left(\frac{\sqrt{q^2+4k_\tau^2}-q}{\sqrt{q^2+4k_\tau^2}+q}\right)\right]. \quad (4.32)$$

The inverse macroscopic dielectric function derived above, $[\epsilon^{\text{zigzag}}_{0,0}]^{-1}(q)$, as well as the screened electron-hole interaction, $W^{\text{zigzag}}(q)$, are reported for selected zigzag tubes in Figs. 4.16(a) and (b), respectively (triangles, CNT lattice). The results are essentially identical to those derived from the simpler structural model used throughout the paper (solid curves, CNT).

4.8.2 Armchair lattice

Armchair carbon nanotubes (n,n) have a chiral vector $\boldsymbol{\mathcal{C}} = 2n\boldsymbol{a} + n\boldsymbol{b}$ corresponding to the chiral angle $\theta = \pi/6$. The vector $\boldsymbol{\mathcal{C}}$ extends over $2n$ units cells of

graphene. The overlap integrals of armchair nanotubes, derived in Appendix A.3, take into account the locations of the atoms occupying these $2n$ units cells:

$$\langle \alpha k | e^{-i(\boldsymbol{G}+\boldsymbol{q})\cdot\boldsymbol{r}} | \alpha' k+q \rangle = \frac{1}{2}\left\{\text{sign}[k(k+q)] + (2\delta_{\alpha,\alpha'}-1)\right\} J_0(RG_\perp) + \frac{(-1)^n}{2}\Big[2\,\text{sign}[k(k+q)] - (2\delta_{\alpha,\alpha'}-1)\Big] J_{2n}(RG_\perp). \tag{4.33}$$

This overlap integral differs from the "jellium" expression (4.24) in the addition of an extra term, originating by the Bessel function of order equal to the number of unit cells. This in turn changes the dielectric function, through the occurrence of an extra, cut-off dependent term:

$$\epsilon^{\text{armchair}}_{\boldsymbol{G},\boldsymbol{G'}}(\boldsymbol{q}) = \delta_{\boldsymbol{G},\boldsymbol{G'}} + \frac{A}{\pi\gamma} v(\boldsymbol{q}+\boldsymbol{G}) \Big[(2\,J_0(RG_\perp) + (-1)^n J_{2n}(RG_\perp))(2J_0(RG'_\perp) + (-1)^n J_{2n}(RG'_\perp)) + \frac{9}{2} J_{2n}(RG_\perp) J_{2n}(RG'_\perp) \log\left(\frac{4k_o^2}{q^2} - 1\right)\Big]. \tag{4.34}$$

The extra-term ensures that the dielectric function diverges for $q \to 0$, the expected behaviour in gapless tubes.

The inverse macroscopic dielectric function derived above, $[\epsilon^{\text{armchair}}_{0,0}]^{-1}(q)$ [triangles, CNT lattice in Fig. 4.16(c)] differs only slightly from that derived from the simpler structural model (solid curves, CNT), and only for $q > 0.01(2\pi)/a$ and small radii. Importantly, these small discrepancies are irrelevant for the computation of the screened electron-hole interaction, as apparent from Fig. 4.16(d).

4.9 Super Coulombic interaction

Direct measurements of electron-electron interaction in materials are generally hard to perform, due to the interference between the measured system and the probe. Recently, the group of S. Ilani at Weizmann Institute of Science developed a new sensing technique to minimize such interference [24], by means of using a suspended carbon nanotube as a scanning tool to probe, with minimal invasiveness, few-electron states within another nanotube. A new experiment, which focused on the case of just two electrons populating the c band of a narrow-gap nanotube, was able to directly measure the Coulomb force repelling the two charges in real space [119].

Therefore, we have computed the screened electron-electron interaction, projected onto the c band and Fourier-transformed in real space. Figures 4.17 and

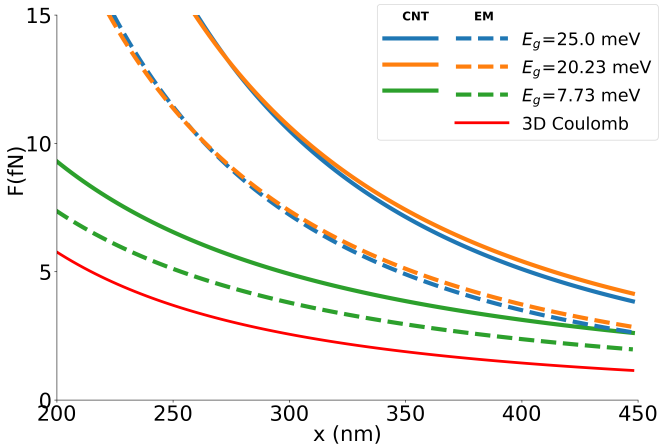

Figure 4.17: Effective electron-electron force along the nanotube axis vs electron separation, x, in tubes having different energy gaps, E_g. The tube radius is $R = 1$ nm. The solid and dashed curves are respectively the model calculation (CNT) and the effective-mass (EM) prediction. The red curve is the standard three-dimensional Coulomb force.

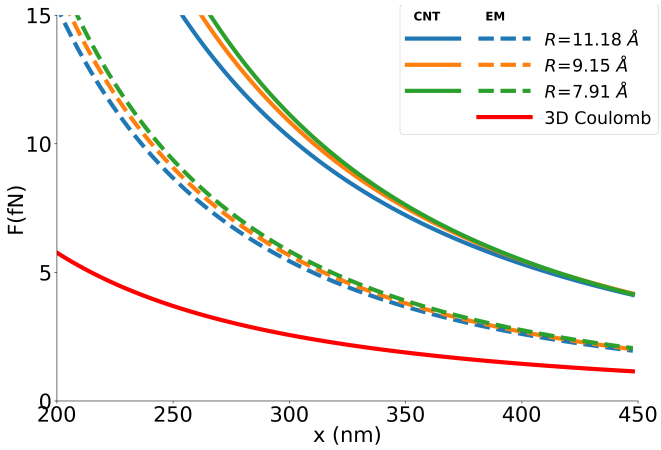

Figure 4.18: Effective electron-electron force along the nanotube axis vs electron separation, x, in tubes of different radii, R. The energy gap is E_g= 20 meV. The solid and dashed curves are respectively the model calculation (CNT) and the effective-mass (EM) prediction. The red curve is the standard three-dimensional Coulomb force.

4.18 show the force dependence on the electron separation in the range of hundreds of nm, which is relevant to the experiment of Ref. [119], and compare it to the standard, three-dimensional bare Coulomb force (red curve). Both effective-mass (EM) and supercell model (CNT) calculations predict that the effective force is stronger than the bare Coulomb force, regardless of the gap (Fig. 4.17) or radius (Fig. 4.18) size, as a consequence of the non-local character of screening in nanotubes [114]. However, only the inclusion into the model of microscopic local

fields, induced by the motion of electrons on the curved tube surface, leads to a major enhancement of the effective force, as seen by contrasting CNT and EM curves for given tube.

Chapter 5

Phase diagram of the Excitonic Insulator in narrow-gap CNT

In the previous section, we have theoretically investigated the screening properties of carbon nanotubes and showed that the long-range Coulomb potential of armchair carbon nanotubes is sufficiently strong to induce an EI phase both according to model and first-principle calculations. Here, we explore the possibility that the EI phase appears even in narrow-gap carbon nanotubes, whose band gaps, we recall, are induced by curvature and in the order of tens of meV.
Narrow-gap carbon nanotubes have electronic structures very similar to armchair tubes featuring truncated Dirac cones in momentum space. The semiconducting nature of the tubes causes more intense Coulomb attraction compared to armchair tubes, allowing the formations of bound excitons with binding energy larger than the band gap, which makes the system unstable against an excitonic condensation.

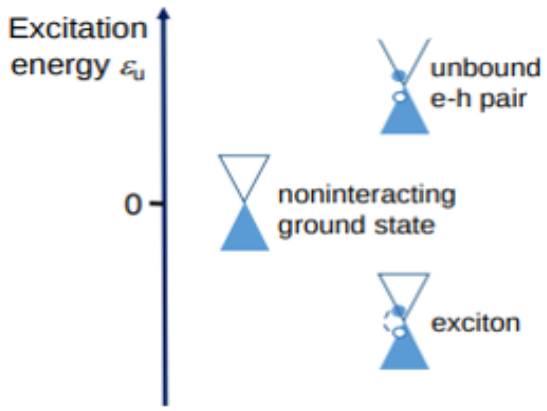

Figure 5.1: Pictorial illustration of an excitonic instability. Figure taken from [28].

The process leading to an EI is analogous to the Cooper instability of a superconducting state, with the excitons playing the role of the Cooper pairs. Pictorially, this is shown in Fig. 5.1. We employ a mean-field theory, developed in a previous work [28], to describe the excitonic instability.

5.1 Electron-Hole interaction

The electron-hole interaction, that is the bonding energy of the excitons, is determined by scatterings processes both on long and short range. Long-range scatterings are, in particular, the dominating processes for the formations of excitons in carbon nanotubes. However, a comprehensive treatment requires even to account the short-range part of the electron-hole interaction [158]. We treat in a different manner the two parts of the electron-hole interaction.
Concerning the long-range part of the electron-hole interaction, we follow the model theory of screening developed in the previous chapter. We recall that in this theory the Coulomb potential $W(\boldsymbol{r}, \boldsymbol{r'})$ is expanded on a plain wave basis set to include the tube-like topology of the Bloch states.

$$W(\boldsymbol{r}, \boldsymbol{r'}) = \sum_{\boldsymbol{q},\boldsymbol{G},\boldsymbol{G'}} e^{-i(\boldsymbol{G'}+\boldsymbol{q})\cdot\boldsymbol{r'}} e^{i(\boldsymbol{G}+\boldsymbol{q})\cdot\boldsymbol{r}} \epsilon^{-1}_{\boldsymbol{G},\boldsymbol{G'}}(\boldsymbol{q}) v(\boldsymbol{q}+\boldsymbol{G'}). \tag{5.1}$$

The reciprocal lattice vectors $\boldsymbol{G}$ are determined with the periodically repeated cell technique on a cylindrical supercell (Fig. 5.2):

$$\boldsymbol{G}_\perp = \frac{\pi}{\Re}\left(n_1\hat{x} + n_3\hat{z}\right), \quad \boldsymbol{G}_\parallel = \frac{2\pi}{\lambda} n_2 \hat{y}. \tag{5.2}$$

In consistence with the previous chapter, the cylindrical supercells have length $\lambda = a\cos(3\theta)$ along the axis and a radius $\Re = 7R$ in the other directions. We fix the total length of the nanotube along the axis to $A = N\lambda$, with N being the number of repetitions of supercells along the axis.

We use the form of the Coulomb potential truncated in the non-periodic directions at the margins of the supercells:

$$v(\mathbf{q}+\mathbf{G}) = \frac{4e^2}{A\Re^2(\mathbf{q}+\mathbf{G})^2}\Big[1 + \Re G_\perp J_1(\Re G_\perp) K_0(\Re|q \tag{5.3}$$

$$+G_\parallel|) - \Re|q+G_\parallel| J_0(\Re G_\perp) K_1(\Re|q+G_\parallel|)\Big], \tag{5.4}$$

The RPA dielectric function is:

$$\epsilon_{\boldsymbol{G},\boldsymbol{G'}}(\boldsymbol{q}) = \delta_{\boldsymbol{G},\boldsymbol{G'}} - \Pi_{\boldsymbol{G},\boldsymbol{G'}}(\boldsymbol{q}) v(\boldsymbol{q}+\boldsymbol{G}), \tag{5.5}$$

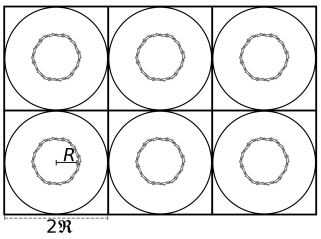

Figure 5.2: Sketch of the supercell structure in the non-periodic directions. The nanotube of radius R is replicated using cylindrical supercell of radius $\mathfrak{R}$ arranged on a square lattice.

with polarisation:

$$\Pi_{\boldsymbol{G},\boldsymbol{G'}}(\boldsymbol{q}) = -\frac{2}{\pi\gamma} J_0(RG_\perp) J_0(RG'_\perp) \sum_\tau \left[1 + \frac{2k_\tau^2}{q\sqrt{q^2+4k_\tau^2}} \log\left(\frac{\sqrt{q^2+4k_\tau^2}-q}{\sqrt{q^2+4k_\tau^2}+q} \right) \right] \quad (5.6)$$

The long-range e-h interaction is retrieved by projecting $W(\boldsymbol{r},\boldsymbol{r'})$ from an initial state $(c,\tau,k)(v,\tau,k+q)$ to a final state $(c,\tau,k+q)(v,\tau,k)$ on the same valley τ. We only include intravalley scatterings ($\tau=\tau'$) as intervalley scatterings ($\tau\neq\tau'$) can be neglected requiring a large momentum that is suppressed by screening.

$$W_{(c\tau k+q,v\tau k,v\tau k+q,c\tau k)} = \iint d\boldsymbol{r} d\boldsymbol{r'} W(\boldsymbol{r},\boldsymbol{r'}) [\boldsymbol{F}^{\tau\dagger}_{ck+q}(\boldsymbol{r}) \boldsymbol{F}^{\tau}_{ck}(\boldsymbol{r})] [\boldsymbol{F}^{\tau'\dagger}_{vk}(\boldsymbol{r'}) \boldsymbol{F}^{\tau'}_{vk+q}(\boldsymbol{r'})] \quad (5.7)$$

By replacing the Coulomb potential with its extended expression, we find that the long-range electron-hole interaction can be rewritten in a very simple form:

$$W_{(c\tau k+q,v\tau k,v\tau k+q,c\tau k)} = f_\tau(k,k+q) w(q), \quad (5.8)$$

where the function $f_\tau(k,k+q)$ is the form factor that comes from the product of the envelope functions:

$$f_\tau(k,k+q) = \frac{1}{2}\left(1 + \frac{k(k+q)+k_\tau^2}{\sqrt{k^2+k_\tau^2}\sqrt{(k+q)^2+k_\tau^2}} \right), \quad (5.9)$$

$w(q)$ is instead the effective screened Coulomb potential felt by the electrons on the nanotube surface:

$$w(q) = \frac{1}{A} \sum_{\boldsymbol{G},\boldsymbol{G'}} J_0(RG_\perp) J_0(RG'_\perp) \epsilon^{-1}_{\boldsymbol{G},\boldsymbol{G'}}(\boldsymbol{q}) v(\boldsymbol{q}+\boldsymbol{G'}). \quad (5.10)$$

We see that there is no dependence on the individual lattice vectors, meaning that the microscopical composition of the system does not matter. As we operate with a

finite size tube of length A, we regularise the long-range electron-hole interaction between wavevectors $(k_j, k_j + q_l)$ on the mesh $2\pi/A$ adopted in the calculations:

$$W_{(c\tau k_j+q_l,v\tau k_j,v\tau k_j+q_l,c\tau k_j)} = \frac{A}{2\pi}\int_{q_l-\frac{\Delta k}{2}}^{q_l+\frac{\Delta k}{2}} dq\ f_\tau(k_j, k_j + q)w(q). \tag{5.11}$$

The short-range part of the electron-hole interaction is originated by two types of scatterings, either intravalley or intervalley [158]. We indicate, respectively, the two contributions to the short-range e-h interactions as $V^{(1)}$ and $V^{(2)}$. First principle computations have found that the magnitude of the two short range contributions are rather constant in reciprocal space and much smaller than W [158, 28]. In addition, the short range contributions are weakly sensible on the screening of the system. For this reason, $V^{(1)}$ and $V^{(2)}$ can be modelled through two constant interactions. We keep however explicit account of the spin structure of the electrons and holes involved in the scattering processes:

$$\begin{aligned} V^{(1)}_{(c\tau'\sigma'k',v\tau'\sigma'k,v\sigma\tau k',c\sigma\tau k)} =& \frac{\Omega_0 w_1}{4\pi RA}(-1)^{\sigma-\sigma'}, \\ V^{(2)}_{(c\tau'\sigma'k',v\tau'\sigma'k,v\sigma\tau k',c\sigma\tau k)} =& \frac{\Omega_0 w_2}{4\pi RA}\,\delta_{\sigma,\sigma'}, \end{aligned} \tag{5.12}$$

where $\Omega_0 = (\sqrt{3}/2)a^2$ is the area of graphene unit cell, and the characteristic energies are estimated as from first principle $w_1 = 4.33eV$ and $w_2 = 2.6eV$ [28].

5.2 Self-energy correction

In the effective-mass approximation, the mutual interaction between the electrons on the π orbitals is generally neglected. Yet, this quantity is particularly relevant when studying the excitonic behaviour of a system [159]. We can take into account this interaction by computing the self energy Σ. We evaluate the self-energy in the screened Hartree-Fock approximation.

$$\Sigma^{HF}(\boldsymbol{r}, \boldsymbol{r}') = \lim_{\eta\to 0^+}\frac{i}{2\pi}\int d\omega' G_0(\boldsymbol{r}, \boldsymbol{r}', \omega')W(\boldsymbol{r}, \boldsymbol{r}')e^{i\eta\omega'}. \tag{5.13}$$

The long-range screened potential $W(\boldsymbol{r}, \boldsymbol{r}')$ is chosen static, because we are mainly concerned with the renormalization of the energies in the region around the K point where the single-particles states are long-living. The propagator G_0 is built in terms of the single-particle wavefunctions:

$$G_0(\boldsymbol{r}, \boldsymbol{r}', \omega) = \sum_{\alpha,\tau,k}\frac{\Psi^*_{\alpha\tau k}(\boldsymbol{r})\Psi_{\alpha\tau k}(\boldsymbol{r'})}{\omega - E^0_{\alpha\tau k} + i\eta\ \text{sign}(E^0_{\alpha\tau k} - \mu)}, \tag{5.14}$$

where the sign function ensures that the valence poles are above the real axis and the conduction poles below.

We treat the self-energy as a first-order perturbation. The self-energy correction to the electronic states of the effective-mass theory $|\alpha\tau k\rangle$ amounts to:

$$\langle\alpha\tau k|\Sigma^{HF}(\boldsymbol{r},\boldsymbol{r}')|\alpha\tau k\rangle = -\frac{A}{2\pi}\int dq\,|F^{*}_{\alpha\tau}(k)F_{\alpha\tau}(k+q)|^2 w(q). \tag{5.15}$$

Rather than computing the self-energy correction of the valence and conduction band separately, we directly compute their difference:

$$\Sigma^{HF}_{\tau}(k) = \langle c\tau k|\Sigma^{HF}(\boldsymbol{r},\boldsymbol{r}')|c\tau k\rangle - \langle v\tau k|\Sigma^{HF}(\boldsymbol{r},\boldsymbol{r}')|v\tau k\rangle, \tag{5.16}$$

$$\Sigma^{HF}_{\tau}(k) = \frac{A}{2\pi}\int dq\,\frac{k_\tau^2 + k(k+q)}{\sqrt{k_\tau^2+k^2}\sqrt{k_\tau^2+(k+q)^2}} w(q). \tag{5.17}$$

The screened Hartree-Fock approximation is known however for overestimating the interaction between the outer electrons [160, 161]. As a solution, we reduce the self-energy correction in our computations by means of a constant multiplicative factor:

$$\Sigma_{\tau}(k) = \beta\,\Sigma^{HF}_{\tau}(k). \tag{5.18}$$

The multiplicative factor β has been taken equal to 0.4 for all carbon nanotubes. This value of β has been chosen by setting the single-particle gap of the (9,0) zigzag carbon nanotube to $110meV$, that it is the value of the gap obtained from first-principle computations. The first-principle computations consist in density functional theory computations on top of which is performed GW. For the computational details, we refer to section 1 of chapter 4.

5.3 Bethe-Salpeter Equation

The wavefunction of a direct exciton is:

$$|\Psi\rangle = \sum_{\sigma\sigma'\tau k}\psi_{\tau\sigma}(k)\chi_{\sigma\sigma'}\hat{c}^{\tau\dagger}_{k,\sigma}\hat{v}^{\tau}_{k,\sigma'}|0\rangle, \tag{5.19}$$

where $|0\rangle$ is the non-interacting ground state, that has the energy levels filled up to the Fermi energy. $\chi_{\sigma\sigma'}$ is a 2×2 spin matrix, equal to the identity for the

spin-singlet exciton $\chi_{\sigma\sigma'} = \mathbb{1}$ and equal to a sum of the three Pauli matrices in a generic direction $\boldsymbol{n}$ for the spin triplet exciton $\chi_{\sigma\sigma'} = \boldsymbol{\sigma} \cdot \boldsymbol{n}$. The energies of the direct exciton are the eigenvalues of the Bethe-Salpeter equation [159, 28]:

$$E^{eh}_{\tau}(k)\psi_{\tau\sigma}(k) - \sum_{\tau q} W^{\tau}_{k+q,k}\psi_{\tau\sigma}(k+q) + \frac{\Omega_0 w_1}{4\pi RA}\sum_{\tau'}\sum_{q}\sum_{\sigma'}(-1)^{\sigma-\sigma'}\psi_{\tau'\sigma'}(k+q) - \frac{\Omega_0 w_2}{4\pi RA}\sum_{\tau\neq\tau'}\sum_{q}\psi_{\tau'\sigma}(k+q) = \mathcal{E}_u\psi_{\tau\sigma}(k), \quad (5.20)$$

where $E^{eh}_{\tau}(k)$ is the energy required to create a free electron-hole pair:

$$E^{eh}_{\tau}(k) = E_{c\tau}(k) - E_{v\tau}(k) + \Sigma_{\tau}(k). \quad (5.21)$$

The other three terms at left in Eq.(5.20) are the contributions of the long-range and short-range e-h interaction. The spin dependence in the Bethe-Salpeter equation rests in the phases of the wavefunctions $\psi_{\tau\sigma}(k)$ as all the other physical quantities are symmetric with respect to the spin. We directly compute the eigenvalues of Eq.(5.20) keeping track of the spin structure. In this manner, we are able to determine the energies of both triplet and singlet excitons, later distinguished using the symmetries of the wavefunctions $\psi_{\tau\sigma}(k)$. Our primary interest is in particular the ground state of the triplet exciton of energy $\mathcal{E}_u$ because it is the lowest lying excitonic state. In case the energy $\mathcal{E}_u$ required to excite the triplet is negative, this unequivocally indicates that the carbon nanotube is unstable with respect to the formation of excitons, allowing us to claim that the true ground state of the carbon nanotube is an excitonic insulator.

5.4 The Excitonic Gap

We build up the wavefunction of the excitonic insulator in resemblance of the ground state of a superconductor, with the excitons playing the role of the Cooper pairs:

$$|\Psi\rangle = \prod_{\sigma\sigma'\tau k}[u_{\tau k\sigma} + \chi_{\sigma\sigma'}v_{\tau k\sigma'}\hat{c}^{\tau\dagger}_{k,\sigma}\hat{v}^{\tau}_{k,\sigma'}]|0\rangle. \quad (5.22)$$

The positive variational quantities $u_{\tau k\sigma}$ and $v_{\tau k\sigma}$ are the population amplitudes of the valence and conduction states, respectively. The population amplitudes depends on the spin index only for what concern the phases. The energy of the ground state is:

$$
\begin{aligned}
E_{GS} = &\sum_{\tau k\sigma} E^{eh}_{\tau}(k) v^2_{\tau k\sigma} - \sum_{\tau kk'} \sum_{\sigma} \bar{W}^{\tau}_{kk'} v_{\tau k\sigma} u_{\tau k\sigma} v_{\tau k'\sigma} u_{\tau k'\sigma} \\
&+ \frac{\Omega_0 w_1}{4\pi RA} \sum_{\tau,\tau'} \sum_{kk'} \sum_{\sigma'} (-1)^{\sigma-\sigma'} v_{\tau k\sigma} u_{\tau k\sigma} v_{\tau' k'\sigma'} u_{\tau' k'\sigma'} \\
&- \frac{\Omega_0 w_2}{4\pi RA} \sum_{\tau\neq\tau'} \sum_{kk'} \sum_{\sigma} v_{\tau k\sigma} u_{\tau k\sigma} v_{\tau' k'\sigma} u_{\tau' k'\sigma}.
\end{aligned}
\tag{5.23}
$$

We introduce the excitonic order parameter $\Delta_\sigma(\tau k)$ that represents the energy gain in creating the electron-hole pairs:

$$
\begin{aligned}
\Delta_\sigma(\tau k) = &\sum_{k'} \left(\bar{W}^{\tau}_{kk'} v_{\tau k'\sigma} u_{\tau k'\sigma} + \frac{\Omega_0 w_1}{4\pi RA} \sum_{\tau'} \sum_{\sigma'} (-1)^{\sigma-\sigma'} v_{\tau' k'\sigma'} u_{\tau' k'\sigma'} \right. \\
&+ \left. \frac{\Omega_0 w_2}{4\pi RA} \sum_{\tau'\neq\tau} v_{\tau' k'\sigma} u_{\tau' k'\sigma} \right).
\end{aligned}
\tag{5.24}
$$

We can rewrite the ground state energy in terms of the order parameter:

$$
E_{GS} = \sum_{\tau k} \left[\frac{E^{eh}_{\tau}(k)}{2} (v^2_{\tau k\sigma} - u^2_{\tau k\sigma} + 1) - \Delta_\sigma(\tau k) u_{\tau k\sigma} v_{\tau k\sigma} \right]. \tag{5.25}
$$

We use the Lagrange multipliers method, exploiting that the ground state energy is minimized at equilibrium. All the variational quantities are determined in terms of $\Delta_\sigma(\tau k)$.

$$
\begin{aligned}
\mathcal{E}_{\tau k} &= \sqrt{\frac{(E^{eh}_{\tau}(k))^2}{4} + \Delta_\sigma(\tau k)^2}, \\
u^2_{\tau k\sigma} &= \frac{1}{2} \left(1 + \frac{E^{eh}_{\tau}(k)}{2\mathcal{E}_{\tau k}} \right), \\
v^2_{\tau k\sigma} &= 1 - u^2_{\tau k\sigma}.
\end{aligned}
\tag{5.26}
$$

Replacing the population amplitudes through their dependence on the order parameter in Eq.(5.24), we find that the order parameter $\Delta_\sigma(\tau k)$ satisfies a set of self consistent equations:

$$
\begin{aligned}
\Delta_\sigma(\tau k) = &\sum_{k'} \left(\frac{\bar{W}^{\tau}_{kk'} \Delta_\sigma(\tau k')}{\mathcal{E}_{\tau k'}} + \frac{\Omega_0 w_1}{4\pi RA} \sum_{\tau'} \sum_{\sigma'} (-1)^{\sigma-\sigma'} \Delta_{\sigma'}(\tau' k) \right. \\
&+ \left. \frac{\Omega_0 w_2}{4\pi RA} \sum_{\tau'\neq\tau} \frac{\Delta_\sigma(\tau' k')}{\mathcal{E}_{\tau' k'}} \right).
\end{aligned}
\tag{5.27}
$$

The resolution of this set of self-consistent equations is done numerically from a starting guess value for the order parameter. At each step, the order parameter is updated until convergence is met. The starting value is chosen exploiting the similarities between Eq.(5.27) and the Bethe-Salpeter equation of Eq.(5.20) when introducing a pseudo-wavefunction $\varphi_{\tau\sigma}(\boldsymbol{k})$, defined as:

$$\varphi_{\tau\sigma}(k) = \frac{\Delta_\sigma(\tau k)}{2\sqrt{\frac{E_\tau^{eh}(k)}{4} + \Delta_\sigma(\tau k)^2}}. \tag{5.28}$$

$$2\sqrt{\frac{(E_\tau^{eh}(k))^2}{4} + \Delta_\sigma(\tau k)^2}\varphi_\tau(k) - \sum_{k'} \bar{W}^\tau_{kk'}\varphi_{\tau\sigma}(k') + \frac{\Omega_0 w_1}{4\pi RA}\sum_{k'}\sum_{\tau'}\sum_{\sigma'} (-1)^{\sigma-\sigma'}\varphi_{\tau'\sigma'}(k') - \frac{\Omega_0 w_2}{4\pi RA}\sum_{k'}\sum_{\tau'\neq\tau}\varphi_{\tau'\sigma}(k') = 0. \tag{5.29}$$

We exploit the eigenstates and eigenvalues of the Bethe-Salpeter equation for building the ansatz used in the numerical resolution of the self-consistent equation. In particular, we take:

$$\Delta_\sigma^{start}(\tau k) = \frac{E_\tau^{eh}(k) - \mathcal{E}_u}{2}\left|\frac{\psi_{\tau\sigma}(k)}{\psi_{\tau\sigma}(0)}\right|. \tag{5.30}$$

We proceed with the self-consistent calculation only in the case in which an excitonic instability is present in the system. Indeed, if not the case, Eq.(5.29) gives a trivial output since the ground state is minimized (Eq. 5.25) with the standard low-temperature occupation of the energy levels, a full valence band and an empty conduction band, as the the nanotubes has no energy gain in forming excitons.

5.5 Solutions of the Self-Consistent Equation

The excitons in the carbon nanotube are energetically favoured in a tight region of the Brillouin zone around the K points, where the Coulomb binding energy is sufficiently large to overcome the single-particle gap [28]. These excitons spontaneously formed lead the carbon nanotube to the Excitonic Insulator phase. In the Excitonic phase, electrons and holes are gapped quasiparticle excitations. The valence and conduction band of the Excitonic Insulator phase differ with respect to their single-particle counterparts for having a flatter dispersion in the region close to the K points and an enhanced gap. We illustrate the band dispersion in a case of example in Fig. 5.3. We can notice that the band dispersion remains symmetric

under swapping of both valleys and wavevectors ($\boldsymbol{k} \to -\boldsymbol{k}$) even in the excitonic phase as long as the axial magnetic fields is absent.

The transport gap at the K points in the Excitonic Insulator phase is:

$$\mathcal{E}_{\tau}^{Gap} = \sqrt{(E_{\tau}^{eh}(0))^2 + 4\Delta(\tau 0)^2}, \tag{5.31}$$

where $E_{\tau}^{eh}(0)$ is the single-particle energy and $|\Delta(\tau, k = 0)|$ the many body order parameter. Making a simple analogy, we associate the order parameter to the binding energy between the electron-hole couple, while the single-particle energy to energy required to promote the freed electron-hole couple to the respective bands. The order parameter gives information about the strength of the Excitonic Insulator phase.

We have determined the magnitude of $|\Delta(K, k = 0)|$ and $\mathcal{E}_{\tau}^{Gap}$ for a wide range of nanotubes, varying the radius R and the chiral angle θ. We map the results in Fig. 5.4. The strongest excitonic phases are realised in carbon nanotubes with small radii close to the zigzag configuration so nanotubes with the largest single-particle gap. This result may seem surprising, since the electrons have to be promoted to the conduction band in order to form the excitons. However, nan-

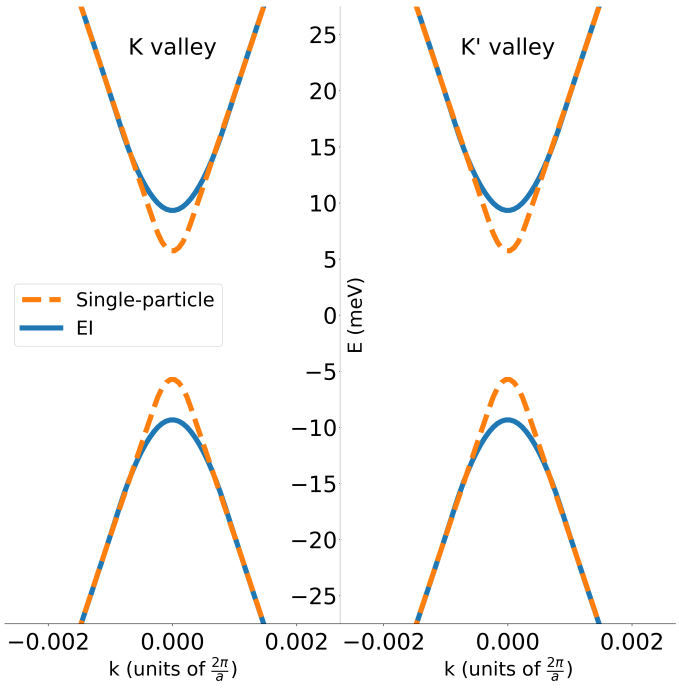

Figure 5.3: Band structure in the regions of the BZ zone close to the two K points for the carbon nanotube with radius $R = 1nm$ and chiral angle $\theta = 20°$. The continuous line indicates the bands in the EI phase, while the dashed lines are the single-particle bands. The left panel refers to the K valley and the right panel to the K' valley.

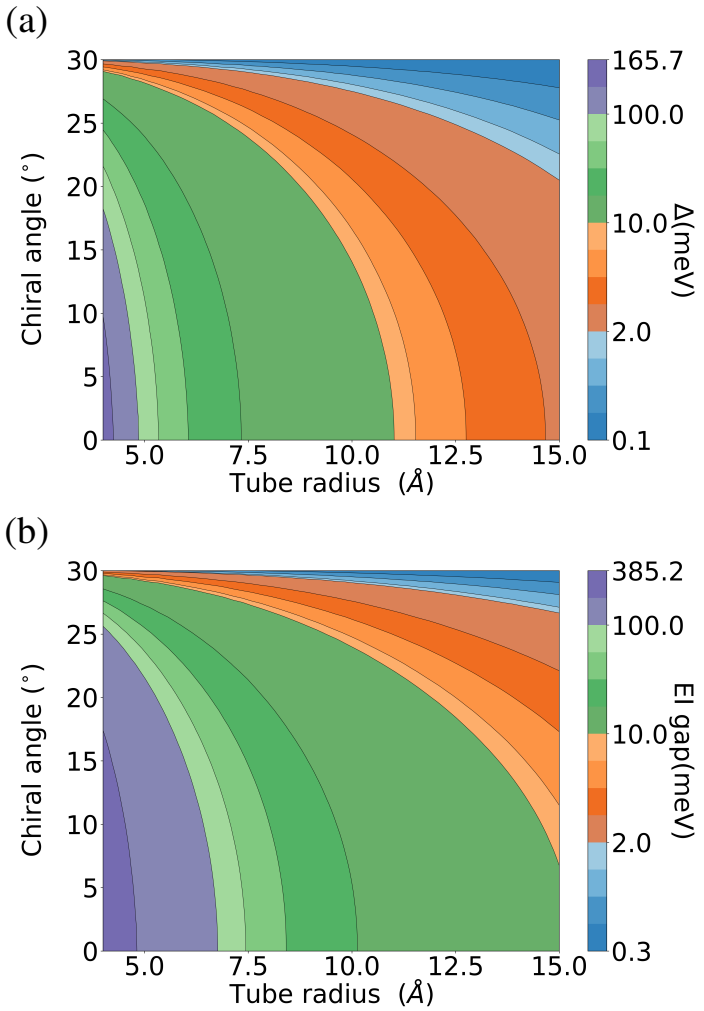

Figure 5.4: Map plot of the order parameter $|\Delta(K', k = 0)|$ (a) and the excitonic gap (b) for a wide set of carbon nanotubes. The shading colours indicate the order of magnitude.

otubes with large single-particle gap are subject to very poor screening (Eq. 5.6) allowing the quasi-1D Coulomb interaction of the nanotube to be very strong. The direct consequence are large values of $|\Delta(K, k = 0)|$. In nanotubes with smaller values of the single-particle gap, the energy required to promote the electrons diminishes but at the same time the screening in the carbon nanotube becomes more effective. Overall, a weaker EI phase is realized. Therefore, we can conclude that in narrow-gap carbon nanotubes exists a general relation between the strength of the excitonic phase and the size of the single-particle gap, suggesting that the single-particle gap is the main quantity to influence the size of the total gap in the EI phase. Further proof of this general dependence can be seen in Fig.

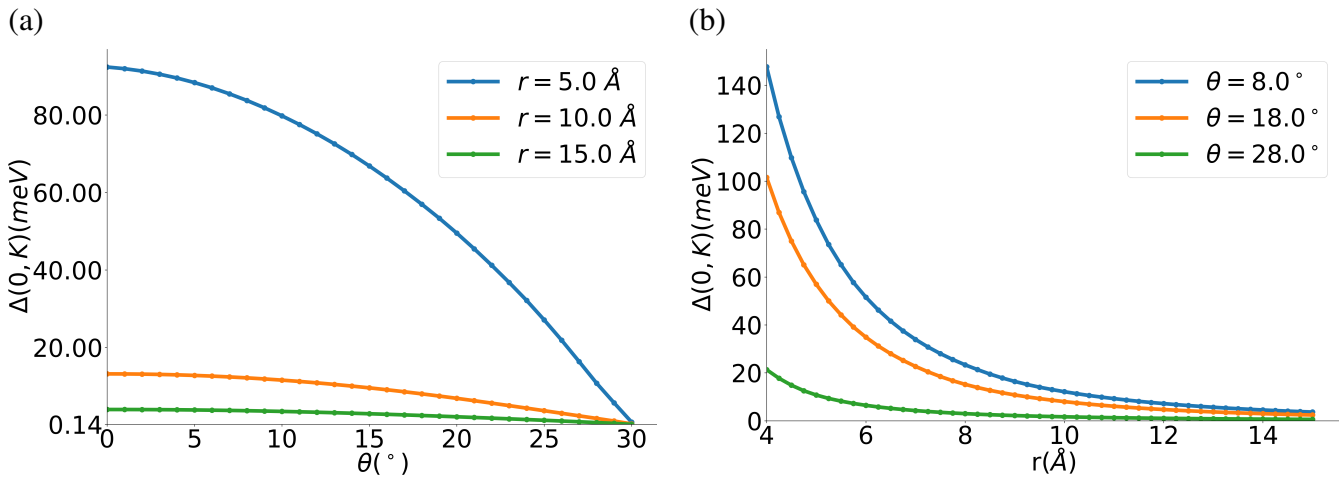

Figure 5.5: Plots of the order parameter $|\Delta(K, k = 0)|$ for selected radii (a) and chiral angles (b).

5.5(a), where we have cut the map of Fig. 5.4 for selected radii. As the chirality is changed from zigzag up to armchair, the single-particle gap is progressively reduced and at the same time even the order parameter diminishes.

The order parameter exhibits even an inverse proportionality to the nanotube radius at fixed chiral angles as emerges from Fig. 5.5 (b). In non-armchair nanotubes, due to the presence of the curvature gap, the order parameter decreases with an almost general power law as $R^{-\beta}$ with β between 2.6 and 2.8. In case of armchair nanotubes, instead, the order parameter decreases more slowly as $R^{-1.5}$. Independently on the chirality of the tube, we expect that in the limit of very large radii the Excitonic Insulator phase fades out in consistence with the fact that flat graphene is not subject to an excitonic instability.

In conclusion, in this chapter, we give evidence that an Excitonic Insulator phase is stable in a wide range of narrow-gap carbon nanotubes. The sizes of the transport gap in the Excitonic Insulator phase remain greatly influenced by the radii and the chirality of the nanotube. It is relevant to mention that our computations mainly reproduce the correct trends since we are limited by not accounting for the contributions of phonons. Phonons could play a relevant role in influencing the overall size of the transport gap, especially in nanotubes with a small chiral angle close to zigzag.

Chapter 6

Excitonic vs Mott Insulator in carbon nanotubes: a proposed experimental test

In the previous section, we have demonstrated that the semiconducting/metallic phase of narrow-gap carbon nanotubes is unstable with respect to a spontaneous excitonic condensation at low temperatures. This finding, even if very promising, does not ensure that the low-temperature correlated phase of narrow-gap carbon nanotubes observed in transport experiments [27, 37] is an excitonic phase. Indeed, there is the possibility that narrow-gap carbon nanotubes are unstable towards diverse kinds of many-body instabilities. In literature, alternative proposed possibilities for the nanotube ground state are that narrow-gap carbon nanotubes are unstable with respect a Mott-Hubbard transition [13, 27] or with respect to lattice distortion [29, 30, 31]. Usually, it is possible to correctly identify a correlated phase studying the characteristic physical quantities associated to the phase. Unfortunately, the low dimensionality of carbon nanotubes and the strong susceptibility to external stimuli make challenging to measure the characteristic physical quantities preventing to easily assess the nature of the correlated phase.

Here, we address the withstanding uncertainty, arguing that exists an unambiguous way to determine if the ground state of narrow-gap carbon nanotubes hosts a condensate of excitons by observing the dependence of the transport gap on the magnetic field. We show that the transport gap of the nanotube features a cusp at the closing of the single-particle gap, which occurs at the Dirac field, when an excitonic condensate is present. We connect this behaviour of the transport gap to the strong sensibility of the excitons to the screening of the carbon nanotube. The other correlated phases, such as a Mott-Hubbard Insulator or a Peierls instability, do not show any particular feature at the Dirac field, being weakly affected by the screening of the carbon nanotube. In particular, here, we draw a compari-

son showing the expected behaviour of nanotubes in the Mott-Hubbard phase. In the course of the work, we describe the correlated phase of the nanotubes within the effective-mass theory for the π quasi-particle states of single-wall carbon nanotubes, properly adapted to include many-body corrections. The magnitude of the many-body corrections is estimated from the theory exposed in the two previous chapter and is corroborated by first principle calculations.

6.1 Quasi-particle theory of carbon nanotubes in the presence of many-body effects

The effective-mass theory of carbon nanotubes, illustrated in chapter 3 and summed up in the two-band model version in section 3.8, describes the electronic states in the valence and conduction bands ($\alpha = c, v$) employing the Bloch states $\psi_\tau(\boldsymbol{r})$ of the corners of the Brillouin zone of graphene ($\tau = K, K'$) multiplied by suitable envelope functions:

$$\Psi_{\alpha\tau k}(\boldsymbol{r}) = F^{\tau A}_{\alpha k}(\boldsymbol{r})\psi_{\tau A}(\boldsymbol{r}) + F^{\tau B}_{\alpha k}(\boldsymbol{r})\psi_{\tau B}(\boldsymbol{r}). \tag{6.1}$$

The set of envelope functions $\boldsymbol{F}^\tau_{\alpha k}$ in the previous sections were chosen as the eigenfuctions of the Dirac Hamiltonian of graphene, that from now on we will call $\mathcal{H}_{sp}$. We recall that $\mathcal{H}_{sp}$ can be represented in the space of the $\boldsymbol{F}^\tau_{\alpha k}$ as the product of couples of Pauli matrices σ and τ, that, respectively, act on the sublattices and on the K valleys indices:

$$\mathcal{H}_{sp} = \gamma \mathbb{1}_\tau \otimes \sigma_x k_\tau + \gamma \tau_z \otimes \sigma_y k. \tag{6.2}$$

The eigenvalues of $\mathcal{H}_{sp}$ are

$$E^{sp}_{\alpha\tau}(k) = s_\alpha \gamma \sqrt{k_\tau^2 + k^2}, \tag{6.3}$$

with k being the continuous component of the wavevector along the axis direction and k_τ being the quantized momenta, generally valley dependent. k_τ cancels out in one of the two K valleys at the Dirac field.

$$k_\tau = k_\perp + \tau k_c \tag{6.4}$$

$$= \frac{1}{R}\frac{\Phi_B}{\Phi_0} + \tau \frac{0.625\ eV}{\gamma R^2}\cos(3\theta). \tag{6.5}$$

The many-body effects enlarge the electronic gap of narrow-gap carbon nanotubes compared to the single-particle treatment, but do not shift the electronic

dispersion in momentum space. The electronic bands preserve a Dirac-like character in the neighbourhood of the Brillouin zone corners. We may then imagine that the electronic state can be written as in Eq.(6.1) using as envelope functions $\boldsymbol{F}^{\tau}_{\alpha k}$ the eigenfunctions of a new quasi-particle hamiltonian composed of $\mathcal{H}_{sp}$ plus a term, that we will call $\mathcal{H}_x$, related to the many-body phase of the carbon nanotube:

$$\mathcal{H} = \mathcal{H}_{sp} + \mathcal{H}_x. \tag{6.6}$$

The many-body hamiltonian $\mathcal{H}_x$ does not commute with the terms featuring inside $\mathcal{H}_{sp}$ and is built based on the symmetries of the nanotubes in the many-body phase. Carbon nanotubes share some of the symmetry properties of graphene among which the time reversal symmetry $\mathbb{T}$ and the inversion symmetry $\mathbb{I}$, discussed in section 2.4. We represent these operations in the same space used for the Hamiltonian. The time-reversal operator $\mathbb{T}$ acts on the $\boldsymbol{F}^{\tau}_{\alpha k}$ swapping the valley index but conserving the sublattice [162, 128, 28]:

$$\mathbb{T} = \tau_x \otimes \sigma_z \hat{K}, \tag{6.7}$$

where $\hat{K}$ is the complex-conjugation operator.
The inversion symmetry $\mathbb{I}$ consists in the inversion of the atomic sites on the graphene plane around the origin. On the $\boldsymbol{F}^{\tau}_{\alpha k}$ functions, this corresponds to swapping the valley index as well as the sublattice. The inversion operator $\mathbb{I}$ takes the form:

$$\mathbb{I} = -\tau_y \otimes \sigma_y \hat{R}, \tag{6.8}$$

where $\hat{R}$ is the inversion operator in the xy space or equivalently a rotation of π. The single-particle Hamiltonian $\mathcal{H}_{sp}$ respects both the symmetry properties in absence of external fields:

$$\begin{matrix} [\mathbb{T}, \mathcal{H}_{sp}] = 0, \\ [\mathbb{I}, \mathcal{H}_{sp}] = 0, \end{matrix} \quad \text{if} \quad B = 0. \tag{6.9}$$

$$\tag{6.10}$$

In the followings, we discuss, separately, how to write the quasi-particle Hamiltonian of nanotubes in the EI phase and in the Mott-Hubbard Insulator phase.

6.1.1 Excitonic Insulator

Signature of the EI phase is the displacement of the electronic charge between the atoms of the two sublattices of the carbon nanotube. This rifts apart the two

sublattices and breaks the inversion symmetry of the carbon nanotube. In the quasi-particle theory, this symmetry property of the EI phase is reproduced within the many-body term of the hamiltonian $\mathcal{H}_{EI}$. Furthermore, since the EI phase is induced by the long-range part of the potential that acts within a single K valley, $\mathcal{H}_{EI}$ must not mix effective mass states with different valley index τ. The form of $\mathcal{H}_{EI}$ upholding these requirements is:

$$\mathcal{H}_{EI} = \Delta_{EI}^{(1)}(k)\, \mathbb{1}_\tau \otimes \sigma_z + \Delta_{EI}^{(2)}(k)\, \tau_z \otimes \sigma_z, \tag{6.11}$$

that gives a valley dependent many-body order parameter $\Delta_{EI}(k,\tau) = \Delta_{EI}^{(1)}(k) + \tau\Delta_{EI}^{(2)}(k)$. Both $\Delta_{EI}^{(1)}(k)$ and $\Delta_{EI}^{(2)}(k)$ generally vary with the magnetic field. At zero magnetic field the EI phase respects the time reversal symmetry, so in this limit $\Delta_{EI}^{(2)}(k) = 0$ restoring the symmetry between the two K valleys. The full form of the effective-mass Hamiltonian of the carbon nanotube in the EI phase is:

$$\mathcal{H}_{tot-EI} = \gamma \mathbb{1}_\tau \otimes \sigma_x \hat{k}_x + \gamma \tau_z \otimes \sigma_y \hat{k}_y + \Delta_{EI}^{(1)}(k)\, \mathbb{1}_\tau \otimes \sigma_z + \Delta_{EI}^{(2)}(k)\, \tau_z \otimes \sigma_z, \tag{6.12}$$

leading to a dispersion in the two closest bands to the gap of the kind:

$$E_{\tau\alpha}(k) = s_\alpha \sqrt{\gamma^2(k^2 + k_\tau^2) + \Delta_{EI}^2(k,\tau)} = s_\alpha \sqrt{E_\tau^{sp}(k) + \Delta_{EI}^2(k,\tau)}. \tag{6.13}$$

6.1.2 Mott-Hubbard insulator

In the Mott-Hubbard phase, the energy cost to hop electrons between neighbouring atoms gets enhanced by the presence of a strong short-range interaction in the nanotube. As this occurs independently on the atomic sublattice, the inversion symmetry is respected in this many-body phase. In addition, at zero magnetic field, even the time-reversal symmetry holds. The many-body term $\mathcal{H}_{HU}$ that satisfies the symmetry requirements at zero field while not commuting with the terms of $\mathcal{H}_{sp}$ reads in the space of the effective-mass functions:

$$\mathcal{H}_{HU}(B=0) = \Delta_u\, \tau_y \otimes \mathbb{1}_\sigma. \tag{6.14}$$

We now put a finite magnetic field and try to use as many-body hamiltonian $\mathcal{H}_{HU}(B=0)$ even with a magnetic field different from zero. The full form of the quasi-particle Hamiltonian is:

$$\mathcal{H}_{tot-HU} = \gamma \mathbb{1}_\tau \otimes \sigma_x k_\perp + \gamma \tau_z \otimes \sigma_x k_c + \gamma \tau_z \otimes \sigma_y k + \Delta_u \tau_y \otimes \mathbb{1}_\sigma, \tag{6.15}$$

where we have split the quantized component of the wavevector in the part linked to the magnetic flux $k_\perp$ and in the part due to curvature k_c. This form of $\mathcal{H}_{tot-HU}$

breaks the time-reversal symmetry as expected when a finite magnetic field is present. Another thing however occurs. The many-body hamiltonian of the Mott-Hubbard phase $\mathcal{H}_{HU}$ commutes with the term in $k_\perp$:

$$[\gamma \mathbb{1}_\tau \otimes \sigma_x k_\perp, \Delta_u \tau_y \otimes \mathbb{1}_\sigma] = 0 \tag{6.16}$$

This leads the energy eigenvalues to be of the kind:

$$\mathcal{H}^2_{tot-HU} = \gamma^2(k_\perp^2 + k_c^2 + \tau_z k_\perp k_c + k^2) + \Delta_u^2 + 2\gamma\tau_y \otimes \sigma_x k_\perp \Delta_u. \tag{6.17}$$

The eigenstates and eigenvalues of a quasi-particle hamiltonian describing the Mott-Hubbard phase are expected to hold to the atomic limit, as the Mott-Hubbard phase acts at the atomic level. However, the last term appearing in Eq.(6.17), $2\gamma\tau_y \otimes \sigma_x k_\perp \Delta_u$, does not respect this fundamental property of the Mott-Hubbard phase going like σ_x in the space of the carbon nanotube sublattices and hence causing the sublattice indices mixing. Since the presence of this term is not consistent with the Mott-Hubbard phase, we modify the form of $\mathcal{H}_{HU}$ at finite magnetic field through two additional terms:

$$\mathcal{H}_{HU} = \Delta_u \tau_y \otimes \mathbb{1}_\sigma + \eta\tau_x \otimes \sigma_y + \zeta\tau_y \otimes \sigma_y, \tag{6.18}$$

defined as $\eta = -i|k_\perp|$ and $\zeta = -|k_\perp|$. We see that the two additional terms vanish at zero field, hence are only presents when the time-reversal symmetry disappears. The new general form of the Hamiltonian in the Mott-Hubbard phase becomes:

$$\begin{aligned}\mathcal{H}_{tot-HU} = \gamma\mathbb{1}_\tau \otimes \sigma_x k_\perp + \gamma\tau_z \otimes \sigma_x k_c + \gamma\tau_z \otimes \sigma_y k + \Delta_u \tau_y \otimes \mathbb{1}_\sigma \\ + \quad \eta\tau_x \otimes \sigma_y + \zeta\tau_y \otimes \sigma_y,\end{aligned} \tag{6.19}$$

The energy of the higher valence and lower conduction bands are:

$$E_\alpha(k) = s_\alpha \sqrt{\gamma^2(k^2 + (|k_\perp| - k_c)^2) + \Delta_u^2}. \tag{6.20}$$

The expression of the energy is very similar to the one we obtain in the Excitonic Insulator phase, differing only for the many-body term. The many-body order parameter of a Mott-Hubbard insulator Δ_u, however, behaves fundamentally different to Δ_{EI} with respect to the magnetic field since Δ_u is induced by the short-range interaction, that acts on a range much shorter than the screening. Thus, in the Mott-Hubbard phase, the total gap depends on the magnetic field only in the single-particle contribution.

6.2 On the computation of the many-body terms

The many-body contributions can thus be incorporated inside quasi-particle theories for carbon nanotubes through symmetry arguments. The quasi-particle theories, however, does not give way to compute the magnitude of the many-body contributions directly. We recur to different methods for the two many-body phases.

In the case of the Excitonic Insulator phase, the computation is done following the scheme presented in the previous chapter in sections 5.3-5.4. We solve the Bethe-Salpeter equation to determine the ground state energy of the triplet excitons. If the ground state energy is negative, we employ a mean field theory, modelled on the BCS theory of superconductivity, to determine self-consistently the magnitude of the excitonic many-body gap $\Delta_{EI}(k,\tau)$. In the computations at finite magnetic field, we disregard the Zeeman coupling of the spins to the magnetic field as it represents a fine structure correction.

$$\Delta_{EI}(k,\tau) = \sum_{\tau k'} \bar{W}(k,k') \frac{\Delta^2_{EI}(k,\tau)}{2\sqrt{(E^{sp}_{\tau}(k))^2 + \Delta^2_{EI}(k,\tau)}}. \tag{6.21}$$

The long-range potential $\bar{W}(k,k')$ couples the electron-hole pairs into excitons and represents the energy gain in establishing the excitonic phase. The computation of $\bar{W}(k,k')$, that is fully detailed in chapter 4, is done at the RPA level starting from the single-particle energies. This enables to take into account the magnetic field effect in the self-consistent computation of the many-body energies $\Delta_{EI}(k,\tau)$.

The order parameter of the Mott-Hubbard insulator Δ_u has been investigated extensively in literature both theoretically [13, 17] and experimentally [27]. It has been found that Δ_u can be taken constant with respect the magnetic field and is inversely proportional to the nanotube radius. Here, as the Mott-Hubbard phase is our comparison, we do not repeat the computation, but we take a value of Δ_u of magnitude comparable with literature:

$$\Delta_u = \frac{2\ meVnm}{R}. \tag{6.22}$$

6.3 Results

We have studied the transport gap of selected carbon nanotubes at varying magnetic fields both in the EI phase and in the Mott-Hubbard Insulator phase. The trends of the transport gap in the two phases are shown in Fig. 6.1 for a nanotube of example. The behaviour of the transport gap differs greatly between the two phases in the region around the Dirac field, where the single-particle gap nullifies. In particular, the dispersion in the EI phase features a sharp cusp close to the Dirac field whereas in the Mott-Hubbard phase the minimum is approached regularly. As the single-particle contribution to the transport gap is the same in both the correlated phases Eq.(6.13,6.20), any difference is originated by the many-body contributions $\Delta_{EI}(\tau)$ and Δ_u. The order parameter $\Delta_{EI}(\tau)$ depends on the long-range potential Eq.(6.21), that is sensible on the screening of the system.

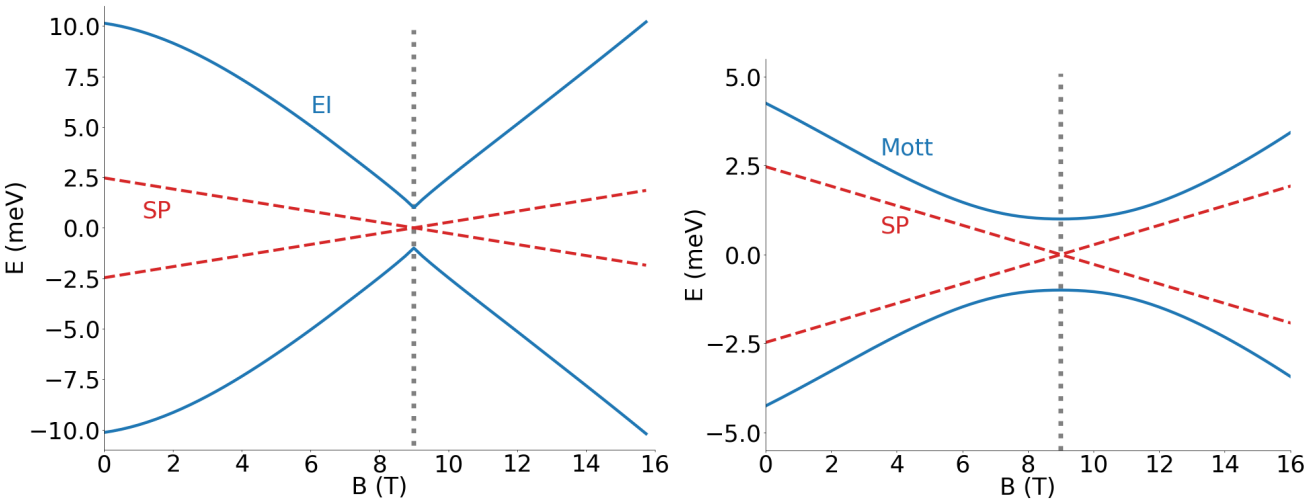

Figure 6.1: Dispersion of the gap with respect to the magnetic field in the EI phase and the Mott-insulator phase of a carbon nanotube of radius $R = 5.5$ Å and chiral angle $\theta = 27.8°$. We plot with a red dashed line the single-particle dispersion for guidance. The dotted vertical line in grey corresponds to the magnetic field that closes the single particle-gap, also known as Dirac field.

Approaching the Dirac field, the single-particle gap shrinks hence the carbon nanotube is subject to stronger screening which lead to smaller values of $\Delta_{EI}(\tau)$. The variations of the screening are especially high in proximity of the Dirac field where the single-particle gap closes, here the $\Delta_{EI}(\tau)$ turns out be almost proportional to the single-particle energy. In the Mott-Hubbard insulator phase, instead,

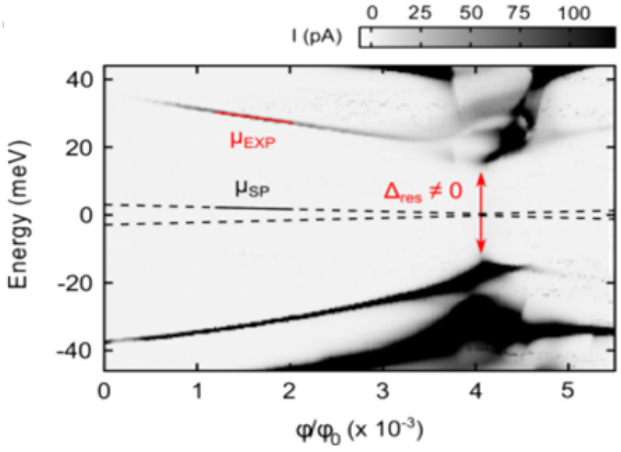

Figure 6.2: Measured current for a nanotube with a radius of 5.5 Å as a function of energy and magnetic flux for the first electron (positive band) and hole (negative band). The Dirac field is at $4 \times 10^{-3}\phi/\phi_0$ ($\simeq 9$ T). Figure taken from [163].

the order parameter Δ_u is always constant so no special feature emerges.

The experimental studies of nanotubes narrow-gaps, like [27] and [37] (reported here in Fig. 6.2), show the appearance of small cusps at the Dirac field. The cusps observed are however less pronounced than in our prediction for the EI phase, meaning that there is still some discrepancy between theory and experiments. In addition, we cannot exclude that the transport experiments may be partly affected by noise, as the gaps studies are very small, leading to the necessity of further studies on the subject for any conclusive proof. The transport experiments, however, even signal a clear giant enhancement of the orbital magnetic moment of the electrons [37]. This behaviour is more compatible with a correlated phase very susceptible to the magnetic field like the EI phase rather than a Mott-Hubbard phase.

To conclude this chapter, we show the EI transport gap in nanotubes of varying chiralities with finite magnetic fields. The corresponding map plot is shown in Fig. 6.3 (a). The generic trend is very reminiscent of the behaviour without many-body effects Fig. 6.3 (b). The transport gap reaches its minimum in correspondence of the Dirac fields of each carbon nanotube, in the figures indicated with a dashed line. Even if small, the transport gap stays always finite for all the chiralities of the tubes. Moving away from the minimum, the transport gap is significantly enhanced compared to the single-particle energies.

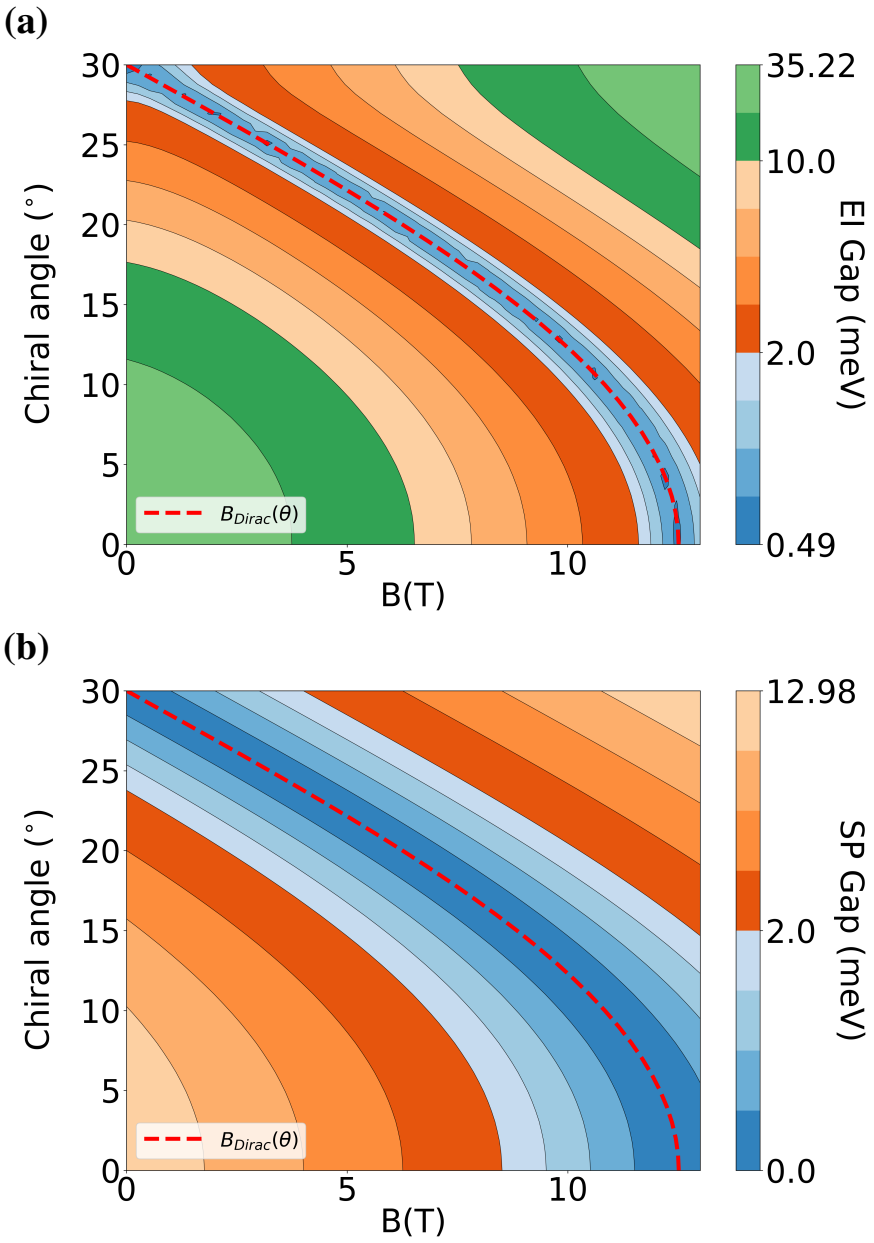

Figure 6.3: Map plots of the total gap (a) and of the single-particle gap in the EI phase (b) at varying axial magnetic fields and chiral angles in narrow-gap carbon nanotubes of radius $R = 1\ nm$. The dashed line in red indicates the Dirac fields for any possible chirality of the tubes.

Chapter 7

Conclusions

In this work, I have performed a novel study of excitonic properties of narrow-gap carbon nanotubes starting from an accurate evaluation of screening properties of carbon nanotubes. As a general result, my findings provide a deeper insight into the previous claim [28] that undoped narrow-gap carbon nanotubes are excitonic and not Mott insulators.

Concerning nanotubes screening, I have developed a simplified approach to compute the dielectric function of narrow-gap carbon nanotubes of any size and chirality, which has the same accuracy of first-principles calculations but is computationally cheaper. A detailed analysis shows a giant enhancement of the screened Coulomb interaction at long wavelength with respect to the one expected for an effectively one-dimensional system. I find that this is caused by the strong, microscopic local fields generated by the electron motion on the curved tube surface. The paradoxical consequence is that the screened electron-hole interaction, once projected onto the lowest conduction and highest valence band, remains long-ranged even in the presence of Fermi points (armchair tubes). Furthermore, the calculated electron-electron interaction in real space shows that the force is super Coulombic, well beyond expectations based on simple EM models. I anticipate that our theory lays the quantitative basis for future studies of many-body physics in carbon nanotubes, where the long-range character of interaction leads to novel phenomena.

The computation of excitonic instabilities has revealed that an Excitonic Insulator phase is possible for a wide range of narrow-gap carbon nanotubes. The size of the transport gap in the Excitonic Insulator phase is greatly influenced by the radii and the chirality of the nanotube. It is relevant to mention that phonons, not accounted for in this work, generally can couple to excitonic degrees of freedom in non-armchair NTs to give rise to hybrid excitonic-phononic phases [33, 34, 35]. I expect that the exciton-phonon coupling may be especially significant in nanotubes with a small chiral angle, close to a zigzag chirality. Despite this

drawback, the quantitative predictions of this work concerning the general trends of the transport gaps are valid and signal the measurable presence of excitonic instabilities in carbon nanotubes.

Finally, I show that studies of nanotubes transport gaps with respect to the magnetic field allow to signal the presence of an excitonic condensate and distinguish this many-body phase from a Mott insulator. The current results from transport experiments [164, 37] seem to support the hypothesis of narrow-gap carbon nanotubes hosting an excitonic condensate. Nevertheless, due to the small sizes of the gaps involved and in view of recent advancements in sensing techniques, further transport experiments are necessary to correctly assess the many-body physics causing the intrinsic semiconducting nature of narrow-gap carbon nanotubes.

Bibliography

[1] R. Saito, G. Dresselhaus, and M. S. Dresselhaus. London: Imperial College Press, 1998.

[2] J.-C. Charlier, X. Blase, and S. Roche. In: *Rev. Mod. Phys.* 79 (2007), pp. 677–732.

[3] S. Ilani and P. L. McEuen. In: *Ann. Rev. of Cond. Mat. Phys.* 1 (2010), pp. 1–25.

[4] E. A. Laird, F. Kuemmeth, G. Steele, K. Grove-Rasmussen, J. Nygård, K. Flensberg, and L. P. Kouwenhoven. In: *Rev. Mod. Phys.* 87 (2015), pp. 703–764.

[5] T. Ando. In: *J. Phys. Soc. Jpn.* 66 (1997), pp. 1066–1073.

[6] J. Maultzsch, R. Pomraenke, S. Reich, E. Chang, D. Prezzi, A. Ruini, E. Molinari, M. S. Strano, C. Thomsen, and C. Lienau. In: *Phys. Rev. B* 72 (2005), 241402(R).

[7] F. Wang, G. Dukovic, L. E. Brus, and T. Heinz. In: *Science* 308 (2005), pp. 838–841.

[8] Catalin D Spataru, Sohrab Ismail-Beigi, Lorin X Benedict, and Steven G Louie. In: *Physical Review Letters* 92.7 (2004), p. 077402.

[9] Rodrigo B Capaz, Catalin D Spataru, Sohrab Ismail-Beigi, and Steven G Louie. In: *Physical Review B* 74.12 (2006), p. 121401.

[10] F. Wang, D. J. Cho, B. Kessler, J. Deslippe, P. J. Schuck, S. G. Louie, A. Zettl, T. F. Heinz, and Y. Ron Shen. In: *Phys. Rev. Lett.* 99 (2007), p. 227401.

[11] Jack Deslippe, Catalin D Spataru, David Prendergast, and Steven G Louie. In: *Nano letters* 7.6 (2007), pp. 1626–1630.

[12] T. Giamarchi. Oxford (UK): Clarendon Press, 2004.

[13] L. Balents and M. P. A. Fisher. In: *Phys. Rev. B* 55 (1997), R11973–R11976.

[14] C. L. Kane, L. Balents, and M. Fisher. In: *Phys. Rev. Lett.* 79 (1997), pp. 5086–5089.

[15] R. Egger and A. O. Gogolin. In: *Phys. Rev. Lett.* 79 (1997), pp. 5082–5085.

[16] Y. A. Krotov, D.-H. Lee, and S. G. Louie. In: *Phys. Rev. Lett.* 78 (1997), pp. 4245–4248.

[17] H. Yoshioka and A. A. Odintsov. In: *Phys. Rev. Lett.* 82 (1999), pp. 374–377.

[18] M. Bockrath, D. H. Cobden, J. Lu, A. G. Rinzler, R. E. Smalley, L. Balents, and P. L. McEuen. In: *Nature* 397 (1999), p. 598.

[19] H. W. C. Postma, T. Teepen, Z. Yao, M. Grifoni, and C. Dekker. In: *Science* 293 (2001), pp. 76–79.

[20] V. V. Deshpande, M. Bockrath, L. I. Glazman, and A. Yacoby. In: *Nature* 464 (2010), pp. 209–216.

[21] V. V. Deshpande and M. Bockrath. In: *Nature Phys.* 4 (2008), p. 314.

[22] Andrea Secchi and Massimo Rontani. In: *Phys. Rev. B* 80 (4 July 2009), p. 041404.

[23] S. Pecker, F. Kuemmeth, A. Secchi, M. Rontani, D. C. Ralph, P. L. McEuen, and S. Ilani. In: *Nature Phys.* 9 (2013), pp. 576–581.

[24] I. Shapir, A. Amo, S. Pecker, C. P. Moca, Ö. Legeza, G. Zarand, and S. Ilani. In: *Science* 364 (2019), pp. 870–875.

[25] Neda Lotfizadeh, Daniel R. McCulley, Mitchell J. Senger, Han Fu, Ethan D. Minot, Brian Skinner, and Vikram V. Deshpande. In: *Phys. Rev. Lett.* 123 (19 Nov. 2019), p. 197701.

[26] N. T. Ziani, F. Cavaliere, K. Guerrero Becerra, and M. Sassetti. In: *Crystals* 11 (2021), p. 20.

[27] V. V. Deshpande, B. Chandra, R. Caldwell, D. S. Novikov, J. Hone, and M. Bockrath. In: *Science* 323 (2009), pp. 106–110.

[28] Daniele Varsano, Sandro Sorella, Davide Sangalli, Matteo Barborini, Stefano Corni, Elisa Molinari, and Massimo Rontani. In: *Nature communications* 8.1 (2017), p. 1461.

[29] K.-P. Bohnen, R. Heid, H. J. Liu, and C. T. Chan. In: *Phys. Rev. Lett.* 93 (2004), p. 245501.

[30] D. Connétable, G.-M. Rignanese, J.-C. Charlier, and X. Blase. In: *Phys. Rev. Lett.* 94 (2005), p. 015503.

[31] Guillaume Dumont, Paul Boulanger, Michel Côté, and Matthias Ernzerhof. In: *Physical Review B* 82.3 (2010), p. 035419.

[32] Yonathan Efroni, Shahal Ilani, and Erez Berg. In: *Phys. Rev. Lett.* 119 (14 Oct. 2017), p. 147704.

[33] W. Chen, A. V. Andreev, A. M. Tsvelik, and D. Orgad. In: *Phys. Rev. Lett.* 101 (2008), p. 246802.

[34] Maria Hellgren, Jacopo Baima, and Anissa Acheche. In: *Phys. Rev. B* 98 (20 Nov. 2018), p. 201103.

[35] Junichi Okamoto, Ludwig Mathey, and Wen-Min Huang. In: *Phys. Rev. B* 98 (20 Nov. 2018), p. 205122.

[36] Mitchell J. Senger, Daniel R. McCulley, Neda Lotfizadeh, Vikram V. Deshpande, and Ethan D. Minot. In: *Phys. Rev. B* 97 (3 Jan. 2018), p. 035445.

[37] Joshua O. Island, Marvin Ostermann, Lee Aspitarte, Ethan D. Minot, Daniele Varsano, Elisa Molinari, Massimo Rontani, and Gary A. Steele. In: *Phys. Rev. Lett.* 121 (12 Sept. 2018), p. 127704.

[38] A. A. Nersesyan and A. M. Tsvelik. In: *Phys. Rev. B* 68 (2003), p. 235419.

[39] J. M. Blatt, K. W. Böer, and W. Brandt. In: *Phys. Rev.* 126 (1962), p. 1691.

[40] S. A. Moskalenko. In: *Fiz. Tverd. Tela.* 4 (1962). [Sov. Phys. Solid State **4,** 199 (1962)], p. 276.

[41] R. C. Casella. In: *J. Phys. Chem. Solids* 24 (1963), p. 19.

[42] L. V. Keldysh and Z. N. Kozlov. In: *Zh. Eksp. i Teor. Fiz. Pisma* 5 (1967). [Sov. Phys.–JETP Lett. **5,** 190 (1968)], p. 238.

[43] V. M. Agranovich and B. S. Toshich. In: *Zh. Eksp. i Teor. Fiz.* 53 (1967). [Sov. Phys.–JETP **26,** 104 (1968)], p. 149.

[44] L. V. Keldysh and A. N. Kozlov. In: *Zh. Eksp. i Teor. Fiz.* 54 (1968). [Sov. Phys.–JETP **27,** 521 (1968)], p. 978.

[45] V. A. Gergel', R. F. Kazarinov, and R. A. Suris. In: *Zh. Eksp. i Teor. Fiz.* 54 (1968). [Sov. Phys.–JETP **27,** 159 (1968)], p. 298.

[46] C. Comte and P. Nozières. In: *J. Physique* 43 (1982), p. 1069.

[47] L. V. Keldysh. In: *Bose-Einstein condensation*. Ed. by A. Griffin, D. W. Snoke, and S. Stringari. Cambridge, UK: Cambridge University Press, 1995. Chap. 12, pp. 246–280.

[48] L. Pitaevskii and S. Stringari. Oxford: Oxford University Press, 2003.

[49] E. Hanamura and H. Haug. In: *Phys. Rep.* 33 (1977), p. 209.

[50] A. Mysyrowicz. In: *J. Physique Colloques* 41.C7 (1980), p. 281.

[51] P. B. Littlewood and X. Zhu. In: *Physica Scripta* T68 (1996), p. 56.

[52] S. A. Moskalenko and D. W. Snoke. Cambridge: Cambridge University Press, 2000.

[53] A. V. Larionov and V. B. Timofeev. In: *JETP Lett.* 73 (2001), p. 301.

[54] L. V. Butov. In: *Solid State Commun.* 127 (2003), p. 89.

[55] L. V. Butov. In: *J. Phys.: Condens. Matter* 16 (2004), R1577.

[56] L. V. Butov. In: *J. Phys.: Condens. Matter* 19 (2007), p. 295202.

[57] A. L. Ivanov and S. G. Tikhodeev, eds. Oxford: Oxford University Press, 2008.

[58] D. Snoke. In: *Science* 298 (2002), p. 1368.

[59] T. M. Rice. In: *Solid State Physics* 32 (1977), pp. 1–86.

[60] L. V. Keldysh. In: *Contemp. Phys.* 27 (1986), p. 395.

[61] D. W. Snoke. In: *Advances in Condens. Matter Phys.* 2011 (2011), p. 938609.

[62] S. I. Shevchenko. In: *Fiz. Nizk. Temp.* 2 (1976). [Sov. J. Low Temp. Phys. **2,** 251 (1976)], p. 505.

[63] Yu. E. Lozovik and V. I. Yudson. In: *Zh. Eksp. i Teor. Fiz.* 71 (1976). [Sov. Phys.–JETP **44,** 389-397 (1976)], pp. 738–753.

[64] T. Fukuzawa, S. S. Kano, T. K. Gustafson, and T. Ogawa. In: *Surf. Sci.* 228 (1990), p. 482.

[65] A. Alexandrou, J. A. Kash, E. E. Mendez, M. Zachau, J. M. Hong, T. Fukuzawa, and Y. Hase. In: *Phys. Rev. B* 42 (1990), R9225.

[66] A. Zrenner, P. Leeb, J. Schäfler, G. Böhm, G. Weimann, J. M. Worlock, L. T. Florez, and J. P. Harbison. In: *Surf. Sci.* 263 (1992), p. 496.

[67] L. V. Butov, A. Zrenner, G. Abstreiter, G. Böhm, and G. Weimann. In: *Phys. Rev. Lett.* 73 (1994), p. 304.

[68] A. A. High, A. T. Hammack, L. V. Butov, M. Hanson, and A. C. Gossard. In: *Optics Lett.* 32 (2007), p. 2466.

[69] A. A. High, A. K. Thomas, G. Grosso, M. Remeika, A. T. Hammack, A. D. Meyertholen, M. M. Fogler, L. V. Butov, M. Hanson, and A. C. Gossard. In: *Phys. Rev. Lett.* 103 (2009), p. 087403.

[70] L. V. Butov, C. W. Lai, A. L. Ivanov, A. C. Gossard, and D. S. Chemla. In: *Nature* 417 (2002), p. 47.

[71] A. A. High, J. R. Leonard, A. T. Hammack, M. M. Fogler, L. V. Butov, A. V. Kavokin, K. L. Campman, and A. C. Gossard. In: *Nature* 483 (2012), p. 584.

[72] Romain Anankine, Mussie Beian, Suzanne Dang, Mathieu Alloing, Edmond Cambril, Kamel Merghem, Carmen Gomez Carbonell, Aristide Lemaıtre, and François Dubin. In: *Physical review letters* 118.12 (2017), p. 127402.

[73] Ouri Karni, Elyse Barré, Sze Cheung Lau, Roland Gillen, Eric Yue Ma, Bumho Kim, Kenji Watanabe, Takashi Taniguchi, Janina Maultzsch, Katayun Barmak, et al. In: *Physical review letters* 123.24 (2019), p. 247402.

[74] Zefang Wang, Daniel A Rhodes, Kenji Watanabe, Takashi Taniguchi, James C Hone, Jie Shan, and Kin Fai Mak. In: *Nature* 574.7776 (2019), pp. 76–80.

[75] R. S. Knox. Vol. Supplement 5. Solid State Physics. New York: Academic Press, 1963.

[76] L. V. Keldysh and Yu. V. Kopaev. In: *Fiz. Tverd. Tela.* 6 (1964). [Sov. Phys. Solid State **6,** 2219 (1965)], pp. 2791–2798.

[77] J. des Cloizeaux. In: *J. Phys. Chem. Solids* 26 (1965), pp. 259–266.

[78] D. Jèrome, T. M. Rice, and W. Kohn. In: *Phys. Rev.* 158 (1967), pp. 462–475.

[79] D. Sherrington and W. Kohn. In: *Rev. Mod. Phys.* 40 (1968), pp. 767–769.

[80] John Bardeen, Leon N Cooper, and John Robert Schrieffer. In: *Physical review* 108.5 (1957), p. 1175.

[81] J. Bardeen. In: *Phys. Rev. Lett.* 6 (1961), p. 57.

[82] B. I. Halperin and T. M. Rice. In: *Solid State Phys.* 21 (1968), pp. 115–192.

[83] W. Kohn. In: *Many-body physics*. Ed. by C. de Witt and R. Balian. New York: Gordon and Breach, 1967, pp. 351–411.

[84] P. Nozières and C. Comte. In: *J. Physique* 43 (1982), p. 1083.

[85] B. Bucher, P. Steiner, and P. Wachter. In: *Phys. Rev. Lett.* 67 (1991), pp. 2717–2720.

[86] P. Wachter, A. Jung, and P. Steiner. In: *Phys. Rev. B* 51 (1995), p. 5542.

[87] P. Wachter. In: *J. Alloys and Compounds* 225 (1995), p. 133.

[88] F. J. Di Salvo, D. E. Moncton, and J. V. Waszczak. In: *Phys. Rev. B* 14 (1976), pp. 4321–4328.

[89] J. A. Wilson. In: *Solid State Commun.* 22 (1977), p. 551.

[90] M. M. Traum, G. Margaritondo, N. V. Smith, J. E. Rowe, and F. J. Di Salvo. In: *Phys. Rev. B* 17 (1978), p. 1836.

[91] G. Margaritondo, C. M. Bertoni, J. H. Weaver, F. Lévy, N. G. Stoffel, and A. D. Katnani. In: *Phys. Rev. B* 23 (1981), p. 3765.

[92] N. G. Stoffel, F. Lévy, C. M. Bertoni, and G. Margaritondo. In: *Solid State Commun.* 41 (1982), p. 53.

[93] O. Anderson, R. Manzke, and M. Skibowski. In: *Phys. Rev. Lett.* 55 (1985), p. 2188.

[94] T. Pillo, J. Hayoz, H. Berger, F. Lévy, L. Schlapbach, and P. Aebi. In: *Phys. Rev. B* 61 (2000), p. 16213.

[95] T. E. Kidd, T. Miller, M. Y. Chou, and T.-C. Chiang. In: *Phys. Rev. Lett.* 88 (2002), p. 226402.

[96] H. Cercellier, C. Monney, F. Clerc, C. Battaglia, L. Despont, M. G. Garnier, H. Beck, P. Aebi, L. Patthey, H. Berger, and L. Forró. In: *Phys. Rev. Lett.* 99 (2007), p. 146403.

[97] J. C. E. Rasch, T. Stemmler, B. Müller, L. Dudy, and R. Manzke. In: *Phys. Rev. Lett.* 101 (2008), p. 237602.

[98] C. Monney, E. F. Schwier, M. G. Garnier, N. Mariotti, C. Didiot, H. Beck, P. Aebi, H. Cercellier, J. Marcus, C. Battaglia, H. Berger, and A. N. Titov. In: *Phys. Rev. B* 81 (2010), p. 155104.

[99] M. Cazzaniga, H. Cercellier, M. Holzmann, C. Monney, P. Aebi, G. Onida, and V. Olevano. In: *Phys. Rev. B* 85 (2012), p. 195111.

[100] Y. Wakisaka, T. Sudayama, K. Takubo, T. Mizokawa, M. Arita, H. Namatame, M. Taniguchi, N. Katayama, M. Nohara, and H. Takagi. In: *Phys. Rev. Lett.* 103 (2009), p. 026402.

[101] A. Taraphder, S. Koley, N. S. Vidhyadhiraja, and M. S. Laad. In: *Phys. Rev. Lett.* 106 (2011), p. 236405.

[102] Liliana Hromadova, Roman Martoňák, and Erio Tosatti. In: *Physical Review B* 87.14 (2013), p. 144105.

[103] Anshul Kogar, Melinda S Rak, Sean Vig, Ali A Husain, Felix Flicker, Young Il Joe, Luc Venema, Greg J MacDougall, Tai C Chiang, Eduardo Fradkin, Jasper van Wezel, and Peter Abbamonte. In: *Science* 358.6368 (2017), pp. 1314–1317.

[104] S Samaneh Ataei, Daniele Varsano, Elisa Molinari, and Massimo Rontani. In: *Proceedings of the National Academy of Sciences* 118.13 (2021).

[105] Daniele Varsano, Maurizia Palummo, Elisa Molinari, and Massimo Rontani. In: *Nature nanotechnology* 15.5 (2020), pp. 367–372.

[106] Bosong Sun, Wenjin Zhao, Tauno Palomaki, Zaiyao Fei, Elliott Runburg, Paul Malinowski, Xiong Huang, John Cenker, Yong-Tao Cui, Jiun-Haw Chu, Xiaodong Xu, S. Samaneh Ataei, Daniele Varsano, Maurizia Palummo, Elisa Molinari, and Massimo Rontani. In: *Nature Physics* (2021), pp. 1–6.

[107] D. V. Khveshchenko. In: *Phys. Rev. Lett.* 87 (2001), p. 246802.

[108] Xiaomeng Liu, Kenji Watanabe, Takashi Taniguchi, Bertrand I Halperin, and Philip Kim. In: *Nature Physics* 13.8 (2017), pp. 746–750.

[109] JIA Li, T Taniguchi, K Watanabe, J Hone, and CR Dean. In: *Nature Physics* 13.8 (2017), pp. 751–755.

[110] Hiroshi Yaguchi and John Singleton. In: *Journal of Physics: Condensed Matter* 21.34 (2009), p. 344207.

[111] David LeBoeuf, CW Rischau, Gabriel Seyfarth, R Küchler, Martin Berben, Steffen Wiedmann, Wojciech Tabis, Medhi Frachet, Kamran Behnia, and Benoit Fauqué. In: *Nature communications* 8.1 (2017), pp. 1–6.

[112] Jinhua Wang, Pan Nie, Xiaokang Li, Huakun Zuo, Benoıt Fauqué, Zengwei Zhu, and Kamran Behnia. In: *Proceedings of the National Academy of Sciences* 117.48 (2020), pp. 30215–30219.

[113] François Léonard and J Tersoff. In: *Applied Physics Letters* 81.25 (2002), pp. 4835–4837.

[114] J. Deslippe, M. Dipoppa, D. Prendergast, M. V. O. Moutinho, R. B. Capaz, and S. G. Louie. In: *Nano Lett.* 9 (2009), pp. 1330–1334.

[115] Anmol Thakur, Rashi Sachdeva, and Amit Agarwal. In: *Journal of Physics: Condensed Matter* 29.10 (2017), p. 105701.

[116] T. Ando. In: *Physica B* 201 (1994), p. 349.

[117] Edward A Laird, Ferdinand Kuemmeth, Gary A Steele, Kasper Grove-Rasmussen, Jesper Nygård, Karsten Flensberg, and Leo P Kouwenhoven. In: *Reviews of Modern Physics* 87.3 (2015), p. 703.

[118] Carlo A Rozzi, Daniele Varsano, Andrea Marini, Eberhard KU Gross, and Angel Rubio. In: *Physical Review B* 73.20 (2006), p. 205119.

[119] I Shapir, A Hamo, and S Ilani. In: *unpublished* ().

[120] Kostya S Novoselov, Andre K Geim, Sergei V Morozov, De-eng Jiang, Yanshui Zhang, Sergey V Dubonos, Irina V Grigorieva, and Alexandr A Firsov. In: *science* 306.5696 (2004), pp. 666–669.

[121] A. H. Castro Neto, F. Guinea, N. M. R. Peres, K. S. Novoselov, and A. K. Geim. In: *Rev. Mod. Phys.* 81 (2009), p. 109.

[122] J. C. Slonczewksi and P. R. Weiss. In: *Phys. Rev.* 109 (1958), pp. 272–279.

[123] Annick Loiseau, Pascale Launois, Pierre Petit, Stephan Roche, and Jean-Paul Salvetat. In: *Lect. Notes Phys* 677 (2006), pp. 495–543.

[124] Philip Richard Wallace. In: *Physical review* 71.9 (1947), p. 622.

[125] DP DiVincenzo and EJ Mele. In: *Physical Review B* 29.4 (1984), p. 1685.

[126] J Maultzsch, S Reich, C Thomsen, S Webster, R Czerw, DL Carroll, SMC Vieira, PR Birkett, and Chris A Rego. In: *Applied physics letters* 81.14 (2002), pp. 2647–2649.

[127] Stephanie Reich, Janina Maultzsch, Christian Thomsen, and Pablo Ordejon. In: *Physical Review B* 66.3 (2002), p. 035412.

[128] T. Ando. In: *J. Phys. Soc. Jpn.* 74 (2005), pp. 777–817.

[129] Andrea Secchi and Massimo Rontani. In: *Physical Review B* 82.3 (2010), p. 035417.

[130] JW Mintmire and CT White. In: *Physical Review Letters* 81.12 (1998), p. 2506.

[131] JM Luttinger. In: *Physical Review* 84.4 (1951), p. 814.

[132] H. Ajiki and T. Ando. In: *J. Phys. Soc. Jpn.* 62 (1993), pp. 1255–1266.

[133] MF Lin and Kenneth W-K Shung. In: *Physical Review B* 51.12 (1995), p. 7592.

[134] Jian Ping Lu. In: *Physical review letters* 74.7 (1995), p. 1123.

[135] E. D. Minot, Y. Yaish, V. Sazonova, and P. L. McEuen. In: *Nature* 428 (2004), pp. 536–539.

[136] C. L. Kane and E. J. Mele. In: *Phys. Rev. Lett.* 78 (1997), p. 1932.

[137] W. Izumida, K. Sato, and R Saito. In: *J. Phys. Soc. Jpn.* 78 (2009), p. 074707.

[138] Min Ouyang, Jin-Lin Huang, Chin Li Cheung, and Charles M Lieber. In: *Science* 292.5517 (2001), pp. 702–705.

[139] H. J. Liu and C. T. Chan. In: *Phys. Rev. B* 66 (2002), p. 115416.

[140] M. Machón, S. Reich, C. Thomsen, D. Sánchez-Portal, and P. Ordejón. In: *Phys. Rev. B* 66 (2002), p. 155410.

[141] I. Cabria, J. W. Mintmire, and C. T. White. In: *Phys. Rev. B* 67 (2003), 121406(R).

[142] Hongki Min, JE Hill, Nikolas A Sinitsyn, BR Sahu, Leonard Kleinman, and Allan H MacDonald. In: *Physical Review B* 74.16 (2006), p. 165310.

[143] Yugui Yao, Fei Ye, Xiao-Liang Qi, Shou-Cheng Zhang, and Zhong Fang. In: *Physical Review B* 75.4 (2007), p. 041401.

[144] F. Kuemmeth, S. Ilani, D. C. Ralph, and P. L. McEuen. In: *Nature* 452 (2008), pp. 448–452.

[145] G. A. Steele, F. Pei, E. A. Laird, J. M. Jol, H. B. Meerwaldt, and L. P. Kouwenhoven. In: *Nature Commun.* 4 (2013), p. 1573.

[146] Volodymyr V Maslyuk, Rafael Gutierrez, and Gianaurelio Cuniberti. In: *Physical Chemistry Chemical Physics* 19.13 (2017), pp. 8848–8853.

[147] G. Onida, L. Reining, and A. Rubio. In: *Rev. Mod. Phys.* 74 (2002), pp. 601–659.

[148] Eberhard KU Gross and Reiner M Dreizler. Vol. 337. Springer Science & Business Media, 2013.

[149] Paolo Giannozzi, Stefano Baroni, Nicola Bonini, Matteo Calandra, Roberto Car, Carlo Cavazzoni, Davide Ceresoli, Guido L Chiarotti, Matteo Cococcioni, Ismaila Dabo, Andrea Dal Corso, Stefano de Gironcoli, Stefano Fabris, Guido Fratesi, Ralph Gebauer, Uwe Gerstmann, Christos Gougoussis, Anton Kokalj, Michele Lazzeri, Layla Martin-Samos, Nicola Marzari, Francesco Mauri, Riccardo Mazzarello, Stefano Paolini, Alfredo Pasquarello, Lorenzo Paulatto, Carlo Sbraccia, Sandro Scandolo, Gabriele Sclauzero, Ari P Seitsonen, Alexander Smogunov, Paolo Umari, and Renata M Wentzcovitch. In: *Journal of Physics: Condensed Matter* 21.39 (Sept. 2009), p. 395502.

[150] P Giannozzi, O Andreussi, T Brumme, O Bunau, M Buongiorno Nardelli, M Calandra, R Car, C Cavazzoni, D Ceresoli, M Cococcioni, N Colonna, I Carnimeo, A Dal Corso, S de Gironcoli, P Delugas, R A DiStasio, A Ferretti, A Floris, G Fratesi, G Fugallo, R Gebauer, U Gerstmann, F Giustino, T Gorni, J Jia, M Kawamura, H-Y Ko, A Kokalj, E Küçükbenli, M Lazzeri, M Marsili, N Marzari, F Mauri, N L Nguyen, H-V Nguyen, A Otero-de-la-Roza, L Paulatto, S Poncé, D Rocca, R Sabatini, B Santra, M Schlipf, A P Seitsonen, A Smogunov, I Timrov, T Thonhauser, P Umari, N Vast, X Wu, and S Baroni. In: *Journal of Physics: Condensed Matter* 29.46 (Oct. 2017), p. 465901.

[151] John P Perdew and Alex Zunger. In: *Physical Review B* 23.10 (1981), p. 5048.

[152] Andrea Marini, Conor Hogan, Myrta Grüning, and Daniele Varsano. In: *Computer Physics Communications* 180.8 (2009), pp. 1392–1403.

[153] Davide Sangalli, Andrea Ferretti, Henrique Miranda, Claudio Attaccalite, Ivan Marri, Elena Cannuccia, P Melo, Margherita Marsili, Fulvio Paleari, Antimo Marrazzo, et al. In: *Journal of Physics: Condensed Matter* 31.32 (2019), p. 325902.

[154] Charles L Kane and EJ Mele. In: *Physical Review Letters* 78.10 (1997), p. 1932.

[155] Sohrab Ismail-Beigi. In: *Physical Review B* 73.23 (2006), p. 233103.

[156] Catalin D. Spataru, S. Ismail-Beigi, L. X. Benedict, and S. G. Louie. In: *Appl. Phys. A* 78 (2004), pp. 1129–1136.

[157] Yuh Tomio, Hidekatsu Suzuura, and Tsuneya Ando. In: *Physical review B* 85.8 (2012), p. 085411.

[158] T. Ando. In: *J. Phys. Soc. Jpn.* 75 (2006), p. 024707.

[159] Tsuneya Ando. In: *Journal of the Physical Society of Japan* 66.4 (1997), pp. 1066–1073.

[160] G Strinati, HJ Mattausch, and W Hanke. In: *Physical Review Letters* 45.4 (1980), p. 290.

[161] Richard M Martin, Lucia Reining, and David M Ceperley. Cambridge University Press, 2016.

[162] H. Suzuura and T. Ando. In: *Phys. Rev. Lett.* 89 (2002), p. 266603.

[163] Joshua O Island, Marvin Ostermann, Lee Aspitarte, Ethan D Minot, Daniele Varsano, Elisa Molinari, Massimo Rontani, and Gary A Steele. In: *Physical review letters* 121.12 (2018), p. 127704.

[164] Vikram V Deshpande, Bhupesh Chandra, Robert Caldwell, Dmitry S Novikov, James Hone, and Marc Bockrath. In: *Science* 323.5910 (2009), pp. 106–110.

Appendix A

Appendix

A.1 Overlap integrals within the model of the nanotube as a series of rings

In this Appendix we compute the overlap integrals, ρ_{cv}, between conduction and valence band states, by modelling the carbon nanotube as a series of rings over which the electronic charge is spread homogeneously.

We recall that the orbital wave function of NT states is:

$$\Psi_{\alpha\tau k}(\boldsymbol{r}) = F^{\tau A}_{\alpha k}(\boldsymbol{r})\,\psi_{\tau A}(\boldsymbol{r}) + F^{\tau B}_{\alpha k}(\boldsymbol{r})\,\psi_{\tau B}(\boldsymbol{r}). \tag{A.1}$$

Here the envelope functions, F, take the form (4.7), and the Bloch states, $\psi_{\tau\eta}(\boldsymbol{r})$, are spread homogeneously over rings placed along the y axis:

$$\psi_{\tau A}(\boldsymbol{r}) = \frac{1}{\sqrt{N}}\frac{e^{i\phi_{\tau A}}}{\sqrt{2\pi R}}\sum_{l=1}^{N}\left[e^{i\boldsymbol{K_\tau}\cdot\boldsymbol{R}^A_l}\,g(\boldsymbol{r}-\boldsymbol{R}^A_l)\right], \tag{A.2}$$

$$\psi_{\tau B}(\boldsymbol{r}) = \frac{1}{\sqrt{N}}\frac{e^{i\phi_{\tau B}}}{\sqrt{2\pi R}}\sum_{l=1}^{N}\left[e^{i\boldsymbol{K_\tau}\cdot\boldsymbol{R}^B_l}\,g(\boldsymbol{r}-\boldsymbol{R}^B_l)\right], \tag{A.3}$$

the phases being $\phi_{KA}=0$, $\phi_{K'A}=\theta$, $\phi_{KB}=-\frac{\pi}{3}+\theta$ and $\phi_{KB}=0$. The functions g are localised along the y axis and orthogonal, according to:

$$g^{*}(\boldsymbol{r}-\boldsymbol{R}^{\eta}_{l})\,g(\boldsymbol{r}-\boldsymbol{R}^{\eta'}_{l'}) \;=\; \delta_{\eta,\eta'}\,\delta_{l,l'}\,\delta(\rho-R)\,\delta(y-R^{\eta}_{l}). \tag{A.4}$$

There are N charge rings for given sublattice and the rings within the sublattice are uniformly spaced along the NT axis, at distance $\lambda = a\cos\left(\frac{\pi}{6}-\theta\right)$:

$$\begin{cases} \boldsymbol{R}^A_l = \left(l\lambda + y^A_0\right)\hat{y} \\ \boldsymbol{R}^B_l = \left(l\lambda + y^B_0\right)\hat{y} \end{cases} \quad \text{with} \quad l = 0, ..., N-1, \tag{A.5}$$

with $y_0^A = y_0^B = 0$.

The overlap integrals of interest within each valley τ, ρ_{cv}, are:

$$\rho_{\alpha\alpha'}(k\hat{y}, q\hat{y}, \boldsymbol{G}) = \langle \alpha\tau k | e^{-i(\boldsymbol{G}+\boldsymbol{q})\cdot\boldsymbol{r}} | \alpha'\tau k + q \rangle, \tag{A.6}$$

where the ket $|\alpha\tau k\rangle$ indicates the NT orbital wave function $\Psi_{\alpha\tau k}$. To proceed we make the expression (A.1) explict and insert it into the definition of $\rho_{\alpha\alpha'}$, using cylindrical coordinates as well as the orthogonality of g's :

$$\rho_{\alpha\alpha'} = \langle \alpha\tau k | e^{-i(\boldsymbol{G}+\boldsymbol{q})\cdot\boldsymbol{r}} | \alpha'\tau k + q \rangle = \frac{1}{2\pi RN} \sum_{\eta=A}^{B} (F^{\eta}_{\tau\alpha k})^* F^{\eta}_{\tau\alpha' k+q} \tag{A.7}$$

$$\times \quad \int_0^{\infty} d\rho \int dy \int_0^{2\pi} d\varphi \sum_{l=0}^{N-1} \rho\, \delta(\rho - R)\, \delta(y - l\lambda)\, e^{-i\left(G_{\parallel} y + \rho G_{\perp} \cos\varphi\right)}.$$

The delta function of ρ argument constrains the integration over the nanotube surface:

$$\rho_{\alpha\alpha'} = \frac{1}{2\pi N} \sum_{\eta=A}^{B} (F^{\eta}_{\tau\alpha k})^* F^{\eta}_{\tau\alpha' k+q} \int dy \int_0^{2\pi} d\varphi \sum_{l=0}^{N-1} \delta(y - l\lambda)\, e^{-i\left(G_{\parallel} y + RG_{\perp} \cos\varphi\right)}. \tag{A.8}$$

We then integrate over y and recall the expression (5.2) of $G_{\parallel}$, obtaining:

$$\rho_{\alpha\alpha'} = \frac{1}{2\pi N} \sum_{\eta=A}^{B} (F^{\eta}_{\tau\alpha k})^* F^{\eta}_{\tau\alpha' k+q} \sum_{l=0}^{N-1} e^{-i2\pi n_2 l} \int_0^{2\pi} d\varphi\, e^{-iRG_{\perp}\cos(\varphi)}. \tag{A.9}$$

The indices n_2 and l are both integers, then the exponential is always equal to 1. Furthermore, the integral over φ is equal to $2\pi J_0(RG_{\perp})$. In conclusion, the overlap integral is:

$$\langle \alpha k | e^{-i(\boldsymbol{G}+\boldsymbol{q})\cdot\boldsymbol{r}} | \alpha' k + q \rangle = \left[(F^{A}_{\tau\alpha k})^* F^{A}_{\tau\alpha' k+q} + (F^{B}_{\tau\alpha k})^* F^{B}_{\tau\alpha' k+q} \right] J_0(RG_{\perp}). \tag{A.10}$$

The possible combinations of α and α' are as follows. The intraband overlap integrals have either $\alpha = c$ and $\alpha' = c$ or $\alpha = v$ and $\alpha' = v$:

$$\langle ck | e^{-i(\boldsymbol{G}+\boldsymbol{q})\cdot\boldsymbol{r}} | ck + q \rangle = \langle vk | e^{-i(\boldsymbol{G}+\boldsymbol{q})\cdot\boldsymbol{r}} | vk + q \rangle = \frac{1}{2} \left(\frac{k(k+q) + k_{\tau}^2 - iqk_{\tau}}{\sqrt{k^2 + k_{\tau}^2}\sqrt{(k+q)^2 + k_{\tau}^2}} + 1 \right) J_0(RG_{\perp}). \tag{A.11}$$

The interband overlap integrals, with $\alpha = c$ and $\alpha' = v$ or viceversa, exhibit a negative sign instead:

$$\langle ck|e^{-i(\boldsymbol{G}+\boldsymbol{q})\cdot\boldsymbol{r}}|vk+q\rangle = \frac{1}{2}\left(\frac{k(k+q)+k_\tau^2 - iqk_\tau}{\sqrt{k^2+k_\tau^2}\sqrt{(k+q)^2+k_\tau^2}} - 1\right) J_0(RG_\perp). \tag{A.12}$$

A.2 Overlap integrals of zigzag carbon nanotubes

In this Appendix and in the next one we compute the overlap integrals ρ_{cv} for zigzag and armchair carbon nanotubes, respectively, by accounting for the actual location of atoms on the curved honeycomb lattice. To this aim, we replace the Bloch states (4.18) with orbitals localised along the tube circumference, whose positions depend on the azimuthal angle φ. The derivation of ρ_{cv} proceeds analogously to what done in Appendix A.1 until one performs the integration over φ. AAs n atoms per sublattice are now localised along φ, one has to sum over their positions, the overlap integrals being:

$$\rho_{\alpha\alpha'} = \frac{1}{2n}\sum_{\eta=A}^{B}(F^{\eta}_{\tau\alpha k})^*(F^{\eta}_{\tau\alpha' k+q})\int_0^{2\pi} d\varphi \sum_{j=0}^{n-1}\delta\left(\varphi-\varphi_j^\eta\right)e^{-iRG_\perp\cos(\varphi)}, \tag{A.13}$$

where the φ_j^η are the angular coordinates of the atoms. We specialise to zigzag nanotubes in the following.

Zigzag nanotubes $(n,0)$ may be thought of as built by rolling the graphene sheet along the chiral vector $\boldsymbol{\mathcal{C}} = n\boldsymbol{a}$, which stretches over n units cells of graphene. There are $2n$ atoms per sublattice, whose positions on the tube surface are:

$$\boldsymbol{R}^A_{l,j} = \begin{cases} R\,\frac{2\pi j}{n}\hat{\varphi} + l\lambda\hat{y} + +R\hat{\rho} \\ R\,\frac{\pi(2j+1)}{n}\hat{\varphi} + \left(l\lambda + \frac{\sqrt{3}}{2}a\right)\hat{y} + R\hat{\rho} \end{cases} \quad \text{with} \quad j = 0, n-1. \tag{A.14}$$

$$\boldsymbol{R}^B_{l,j} = \begin{cases} R\,\frac{\pi(2j+1)}{n}\hat{\varphi} + \left(l\lambda + \frac{1}{2\sqrt{3}}a\right)\hat{y} + R\hat{\rho} \\ R\,\frac{2\pi j}{n}\hat{\varphi} + \left(l\lambda + \frac{2}{\sqrt{3}}a\right)\hat{y} + R\hat{\rho} \end{cases} \quad \text{with} \quad j = 0, n-1. \tag{A.15}$$

The distance between two unit cells along the axial direction is $\lambda = \sqrt{3}a$. We

insert coordinates (A.14) into (A.13), obtaining

$$\rho_{\alpha\alpha'} = \frac{1}{2n}\sum_{\eta=A}^{B}(F^{\eta}_{\tau\alpha k})^{*}F^{\eta'}_{\tau\alpha' k+q}\int_0^{2\pi}d\varphi\sum_{j=0}^{n-1}\left[\delta\left(\varphi-\frac{2\pi j}{n}\right)\right. \\ \left. + \quad \delta\left(\varphi-\frac{\pi(2j+1)}{n}\right)\right]e^{-iRG_{\perp}\cos(\varphi)}, \quad \text{(A.16)}$$

$$\rho_{\alpha\alpha'} = \frac{1}{2n}\sum_{\eta=A}^{B}(F^{\eta}_{\tau\alpha k})^{*}F^{\eta'}_{\tau\alpha' k+q}\sum_{j=0}^{n-1}\left[e^{-iRG_{\perp}\cos\left(\frac{2\pi j}{n}\right)}+e^{-iRG_{\perp}\cos\left(\frac{\pi(2j+1)}{n}\right)}\right]. \quad \text{(A.17)}$$

We rewrite the two exponentials as a sum of Bessel functions by using the Jacobi-Anger identity:

$$e^{ixcos(\zeta)} = J_0(x) + 2\sum_{m=1}^{\infty} i^m J_m(x)\cos(m\zeta). \quad \text{(A.18)}$$

Then (A.17) becomes:

$$\rho_{\alpha\alpha'} = \frac{1}{2n}\sum_{\eta=A}^{B}(F^{\eta}_{\tau\alpha k})^{*}F^{\eta'}_{\tau\alpha' k+q}\sum_{j=0}^{n-1}\left[2J_0(x)+2\sum_{m=1}^{\infty}\left(i^m J_m(x)\cos\left(\frac{\pi m j}{n}\right)\right.\right. \\ \left.\left. + \quad i^m J_m(x)\cos\left(\frac{\pi m(2j+1)}{n}\right)\right)\right]. \quad \text{(A.19)}$$

We now sum over j. The first term is obvious. In the second one, we exchange the order of the sums over j and m, and use the identities

$$\sum_{j=0}^{n-1} i^m J_m(x)\cos\left(\frac{\pi m j}{n}\right) = \begin{cases} n\, i^m J_m(x) & \text{if } m \text{ is a multiple of n} \\ 0 & \text{otherwise} \end{cases}, \quad \text{(A.20)}$$

$$\sum_{j=0}^{n-1} i^m J_m(x)\cos\left(\frac{\pi m(2j+1)}{n}\right) = \begin{cases} (-1)^{\frac{m}{n}} n\, i^m J_m(x) & \text{if } m \text{ is a multiple of n} \\ 0 & \text{otherwise} \end{cases}. \quad \text{(A.21)}$$

Putting everything together, the overlap integral becomes:

$$\langle \alpha k | e^{-i(\boldsymbol{G}+\boldsymbol{q})\cdot\boldsymbol{r}} | \alpha' k+q \rangle = \\ \left((F^A_{\tau\alpha k})^* F^A_{\tau\alpha' k+q} + (F^B_{\tau\alpha k})^* F^B_{\tau\alpha' k+q}\right) \left[J_0(RG_\perp) + 2\sum_{m=1}^{\infty} (-1)^m J_{2mn}(RG_\perp) \right]. \tag{A.22}$$

As the Bessel functions of large multiples of n decay very rapidly, we only consider the first term in the sum in m. The exact intraband and interband overlap integrals are:

$$\langle ck | e^{-i(\boldsymbol{G}+\boldsymbol{q})\cdot\boldsymbol{r}} | ck+q \rangle = \\ \frac{1}{2}\left(\frac{k(k+q)+k_\tau^2 - iqk_\tau}{\sqrt{k^2+k_\tau^2}\sqrt{(k+q)^2+k_\tau^2}} + 1 \right) (J_0(RG_\perp) + 2(-1)^n J_{2n}(RG_\perp)), \tag{A.23}$$

$$\langle ck | e^{-i(\boldsymbol{G}+\boldsymbol{q})\cdot\boldsymbol{r}} | vk+q \rangle = \\ \frac{1}{2}\left(\frac{k(k+q)+k_\tau^2 - iqk_\tau}{\sqrt{k^2+k_\tau^2}\sqrt{(k+q)^2+k_\tau^2}} - 1 \right) (J_0(RG_\perp) + 2(-1)^n J_{2n}(RG_\perp)). \tag{A.24}$$

A.3 Overlap integrals of armchair carbon nanotubes

Armchair nanotubes (n, n) may be thought of as built by rolling the graphene sheet along the chiral vector $\boldsymbol{\mathcal{C}} = 2n\boldsymbol{a} + n\boldsymbol{b}$, which covers $2n$ units cell of graphene. There are n atoms per sublattice, with positions:

$$\begin{aligned} \boldsymbol{R}^A_{l,j} &= R\,\frac{\pi j}{n}\hat{\varphi} + \left(l\lambda - (-1)^j \frac{a}{4}\right)\hat{y} + R\hat{\rho} \\ &\qquad\qquad \text{with} \quad j = 0, 2n-1, \\ \boldsymbol{R}^B_{l,j} &= R\,\left(\frac{\pi j}{n}\hat{\varphi} + \frac{\pi}{3n}\right)\hat{\varphi} + \left(l\lambda - (-1)^j \frac{a}{4}\right)\hat{y} + R\hat{\rho} \\ &\qquad\qquad \text{with} \quad j = 0, 2n-1. \end{aligned} \tag{A.25}$$

The distance between two subsequent unit cells along the axial direction is $\lambda = a$. To compute the overlap integrals $\rho_{\alpha\alpha'}$, we follow the same procedure used for zigzag tubes in the previous appendix. After integrating over φ, we obtain:

$$\rho_{\alpha\alpha'} = \frac{1}{2n}\sum_{j=0}^{2n-1} \Big[(F^A_{\tau\alpha k})^* F^A_{\tau\alpha' k+q} e^{-iRG_\perp \cos\left(\frac{\pi j}{n}\right)} + (F^B_{\tau\alpha k})^* F^B_{\tau\alpha' k+q} \\ \times \quad e^{-iRG_\perp \cos\left(\frac{\pi j}{n}+\frac{\pi}{3n}\right)} \Big]. \tag{A.26}$$

Again, using the Jacobi-Anger identity (A.18), we rewrite the exponentials as a sum of Bessel functions of different orders, J_m. We then obtain two sums over indexes j and m, and evaluate the sums over j for given m, according to

$$\sum_{j=0}^{2n-1} i^m J_m(x) \cos\left(\frac{\pi m j}{n}\right) = \begin{cases} 2n\, i^m J_m(x) & \text{if } m \text{ is a multiple of 2n} \\ 0 & \text{otherwise} \end{cases}, \quad \text{(A.27)}$$

$$\sum_{j=0}^{2n-1} i^m J_m(x) \cos\left(\frac{\pi m(3j+1)}{3n}\right) = \begin{cases} 2n \cos\left(\frac{m\pi}{3}\right)\, i^m J_m(x) & \text{if } m \text{ is a multiple of 2n} \\ 0 & \text{otherwise} \end{cases}. \quad \text{(A.28)}$$

The resulting overlap integral is:

$$\langle \alpha k | e^{-i(\boldsymbol{G}+\boldsymbol{q})\cdot\boldsymbol{r}} | \alpha' k+q \rangle = \frac{1}{2}\Bigg[(F^A_{\tau\alpha k})^* F^A_{\tau\alpha' k+q} \left(J_0(RG_\perp) + 2\sum_{m=1}^{\infty} (-1)^m J_{2mn}(RG_\perp) \right)$$
$$+ (F^B_{\tau\alpha k})^* F^B_{\tau\alpha' k+q} \left(J_0(RG_\perp) + 2\sum_{m=1}^{\infty} \cos\left(\frac{2m\pi}{3}\right) (-1)^m J_{2mn}(RG_\perp) \right) \Bigg]. \quad \text{(A.29)}$$

As before, it is sufficient to retain the first addendum of the sum over m. The intraband and interband overlap integrals of armchair nanotubes are

$$\langle ck | e^{-i(\boldsymbol{G}+\boldsymbol{q})\cdot\boldsymbol{r}} | ck+q \rangle = \frac{1}{2}\left(\frac{k(k+q)+k_\tau^2 - iqk_\tau}{\sqrt{k_\tau^2+k^2}\sqrt{k_\tau^2+(k+q)^2}} + 1 \right) J_0(RG_\perp)$$
$$+ \quad \frac{(-1)^n}{2}\left(2\frac{k(k+q)+k_\tau^2 - iqk_\tau}{\sqrt{k_\tau^2+k^2}\sqrt{k_\tau^2+(k+q)^2}} - 1 \right) J_{2n}(RG_\perp), \quad \text{(A.30)}$$

$$\langle ck | e^{-i(\boldsymbol{G}+\boldsymbol{q})\cdot\boldsymbol{r}} | vk+q \rangle = \frac{1}{2}\left(\frac{k(k+q)+k_\tau^2 - iqk_\tau}{\sqrt{k_\tau^2+k^2}\sqrt{k_\tau^2+(k+q)^2}} - 1 \right) J_0(RG_\perp)$$
$$+ \quad \frac{(-1)^n}{2}\left(2\frac{k(k+q)+k_\tau^2 - iqk_\tau}{\sqrt{k_\tau^2+k^2}\sqrt{k_\tau^2+(k+q)^2}} + 1 \right) J_{2n}(RG_\perp). \quad \text{(A.31)}$$

A.4 Analysis of the long-range limit of the Coulomb potential

In the main text, we have expanded the Coulomb potential through two different Fourier decompositions. The first one is the Fourier transform (4.10) of the

Coulomb potential on a uniform cylindrical surface, $V_{\rm cyl}(m,q)$. The second one is the three-dimensional Fourier transform (5.3) of the truncated Coulomb potential, $v(\mathbf{q}+\mathbf{G})$. Independently from the Fourier decomposition of choice, the long-range, macroscopic behaviour of $v(\mathbf{q}+\mathbf{G})$ and $V_{\rm cyl}(m,q)$ in the limit $q\to 0$ must be the same, as both forms derive from the same real-space potential, e^2/r (r is the radial distance in spherical coordinates). To show this, we constrain the Fourier transformation to a finite nanotube length, A (we use the symbols $\tilde{v}$ and $\tilde{V}_{\rm cyl}$ to identify the quantities obtained in this way). For $\tilde{v}$ one has:

$$\tilde{v}(q,\mathbf{G}_\perp)=\frac{e^2}{A\pi\mathfrak{R}^2}\int_{-A/2}^{A/2}dy\int_0^{2\pi}d\theta\int_0^{\mathfrak{R}}dr\frac{r}{\sqrt{r^2+y^2}}e^{iqy}e^{irG_\perp\cos(\theta)}. \tag{A.32}$$

We now take the limit $q\to 0$:

$$\tilde{v}(0,\mathbf{G}_\perp)=\frac{e^2}{A\pi\mathfrak{R}^2}\int_{-A/2}^{A/2}dy\int_0^{2\pi}d\theta\int_0^{\mathfrak{R}}dr\frac{r}{\sqrt{r^2+y^2}}e^{irG_\perp\cos(\theta)}, \tag{A.33}$$

which gives

$$\tilde{v}(0,\mathbf{G}_\perp)=\frac{4e^2}{A(G_\perp\mathfrak{R})^2}\Big[1-J_0(G_\perp\mathfrak{R})+G_\perp\mathfrak{R}J_1(G_\perp\mathfrak{R})\log\left(\frac{A}{\mathfrak{R}}\right)\Big]. \tag{A.34}$$

The long-wavelength, macroscopic limit is:

$$\tilde{v}(0,0)=\frac{e^2}{A}\left[1+2\log\left(\frac{A}{\mathfrak{R}}\right)\right]. \tag{A.35}$$

For $\tilde{V}_{\rm cyl}$ one has:

$$\tilde{V}_{cyl}(m,q)=\frac{e^2}{2A\pi R}\int_{-A/2}^{A/2}dy\int_0^{2\pi}d\varphi\frac{e^{im\varphi}\,e^{iqy}}{\sqrt{4R^2\sin^2\left(\frac{\varphi}{2}\right)+y^2}}, \tag{A.36}$$

and in the limit $q\to 0$:

$$\tilde{V}_{cyl}(m,0)=\frac{e^2}{2A\pi R}\int_{-A/2}^{A/2}dy\int_0^{2\pi}d\varphi\frac{e^{im(\varphi)}}{\sqrt{4R^2\sin^2\left(\frac{\varphi}{2}\right)+y^2}}, \tag{A.37}$$

that is

$$\tilde{V}_{cyl}(m,0)=\begin{cases}\frac{e^2}{Am} & \text{if}\quad m\neq 0\\ \frac{2e^2}{A}\log\left(\frac{A}{R}\right) & \text{if}\quad m=0\end{cases}. \tag{A.38}$$

The macroscopic term amounts to:

$$\tilde{V}_{cyl}(0,0) = \frac{2e^2}{A} \log\left(\frac{A}{R}\right). \tag{A.39}$$

We recall that the nanotube length A is linked to the sampling of the Brillouin zone, $A = 2\pi/\mathrm{d}q$. As a consequence both macroscopic potentials (A.35) and (A.39) exhibit an analogous logarithmic divergence of the kind $\sim -\log(R\,\mathrm{d}q)$, leading to the same long-range behaviour.